Strongly Correlated Micro/Nano-Domains of Functional Lipids for Geometrical Control of Dynamic Cell Adhesion

Dissertation zur Erlangung des Doktorgrades
der mathematisch-naturwissenschaftlichen Fakultät
der Universität Augsburg, vorgelegt von

Jochen Oelke

Institut für Physik
der Universität Augsburg
Lehrstuhl für Experimentalphysik I

Erster Gutachter: Univ.-Prof. Dr. Achim Wixforth
Zweiter Gutachter: Univ.-Prof. Dr. Motomu Tanaka

Tag der Einreichung: 10.10.2008
Tag der mündlichen Prüfung: 21.11.2008

Meiner Familie

Table of Contents

List of Figures

„Was wir wissen, ist ein Tropfen;
was wir nicht wissen, ein Ozean“
Isaac Newton

Summary

The primary goal of this thesis was to design well-defined cell membrane models that locally display micro/nano-domains of bio-functional sugars, which mimic lipid rafts in biological cells. The uniqueness of this work exists in the use of fluorinated (and thus non-biological) lipid anchors with an aid of organic chemistry.

In Chapter 2, the domains formed by a lipid with the largest degree of fluorination (FL17) were fully characterized. Owing to both hydrophobic and oleophobic nature of fluorinated lipids, they are separated from the matrix phospholipids membranes and create solid domains within a wide range of mixing ratio (up to 33 mol%). The size of sub-micrometer clusters, which is close to the resolution limit of the optical microscopy, was determined using grazing-incidence X-ray diffraction (GIXD) technique with an aid of analyzer crystal optics of a high spatial resolution. It has been demonstrated that each domain consists of single crystallite of fluorinated lipids, whose diameter (~ 350 nm) is almost constant between 5 and 33 mol%. The highly mono-dispersive size distribution of the domains enables to treat them as two-dimensional colloidal particles. The radial distribution functions of the self-assembled lipid clusters can be obtained using a self-developed image analysis routine, yielding the potential of mean force. The positions of potential minima correspond to the correlation distance between domains, while spring constants of the potentials reflect how sharply the inter-domain correlations are confined.

In Chapter 3, the influence of the molecular chemistry on the domain size has been examined by the systematic variation of the length and number of fluorinated chains. First, it was found that the domain size is not influenced by the number of fluorocarbon chains. More remarkably, the length of fluorocarbon chains significantly influenced the domain size: the change in the number of fluorocarbons from 10 to 17 results in the modulation of the domain size by more than an order of magnitude. Interestingly, however, the increase in the domain size was observed with the decrease in the chain length. This can successfully be explained by a so-called “equivalent dipole model”, which takes into account the height mismatch between the fluorinated lipids and the surrounding matrix. As a preliminary attempt to add bio-functionality, a mannose monosaccharide was coupled to the head group. It has been confirmed that the fluorinated lipids do not loose the capability to form highly uniform domains in the presence of the mannose function.

In Chapter 4, the surface of a flat-μ-fluidics chip was functionalized with the lipid monolayers that locally display the fluorinated lipid domains. The pre-structuring of chip surfaces with photolithography allows for the fabrication of a free standing, half-cylindrical water channel with the liquid volume of about 7 μl. As the first attempt, bacteria have mannose binding proteins were in contact with the mannose domains then subjected to various shear fields, which can be regulated up to 1000 s^{-1}.

The results obtained here demonstrated that synthetic lipids with non-biological fluorocarbon anchors can offer unique advantages over commonly used raft models composed of complex lipid mixtures to form highly uniform domains, whose size and distribution can be fine-tuned by molecular chemistry and mixing ratio, respectively.

Introduction

Lipid membranes are a major constituent of biological membranes, acting as the boundary between interior and exterior of cells and organelles. Owing to their amphiphilic nature, lipid molecules assemble into a bilayer in water in order to minimize the contact of hydrophobic chains to the surrounding water (called hydrophobic effect [Tanford, 1980]). This unique property fascinated physicists to describe lipid membranes within the framework of liquid-crystal theory [Sackmann & Lipowsky, 1995]. Since lipid molecules and membrane proteins do not possess short-range order, they can freely diffuse within the membrane plane. These features enable membranes to act as important filter materials: Organelles serve as micro-containers to confine biochemical processes inside, and plasma membranes reject the insertion of toxic substances. Special nutrients, wastes, and metabolites can selectively pass through the membranes and go to the external environment. Furthermore, many important biochemical processes occur at membrane surfaces via interactions between various membrane proteins.

In 1972, Singer & Nicholson introduced the fluid mosaic model [Singer & Nicholson, 1972], where a fluid lipid membrane act as a quasi-two-dimensional matrix for randomly distributed proteins "mosaic" (see Fig. 1, for a sketch of a cell plasma membrane).

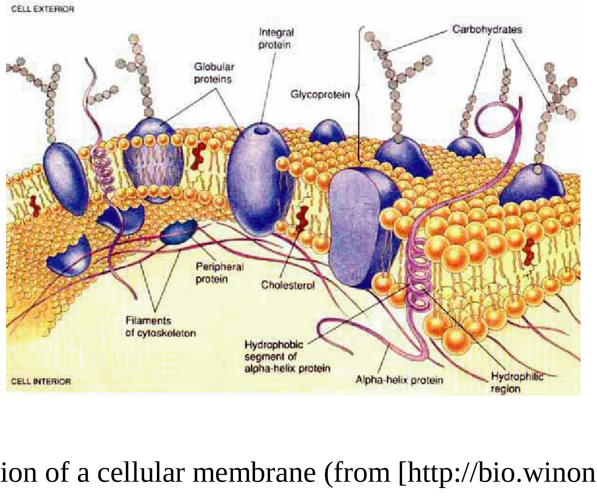

Fig. 1 Schematic illustration of a cellular membrane (from [http://bio.winona.edu/berg])

On the other hand, self-assembled mixtures of matrix lipids and membrane proteins need not always mix uniformly, but can form regional differences in composition and therefore change the physical properties of the plasma membrane locally [Jain & White, 1977; Simons & Vaz, 2004]. In recent years, an increasing number of studies have evidenced that such micro-domains are responsible for various biologically important processes, such as signal transduction and membrane trafficking [Edidin, 2003; Maxfield, 2002; Simons & Toomre, 2000]. Functional micro-domains are categorized into three major classes; (i) coated pits, (ii) caveolae, and (iii) lipid rafts [Thompson & Tillack, 1985].

Coated pits are important during the receptor mediated uptake of substances like iron (Fe^{3+}) into cells, as reported by Sackman and Lipowsky [Sackmann & Lipowsky, 1995]. Usually plasma membranes are impermeable for such substances, but by the formation of coated pits, in combination with the recycling of membrane receptors the allow for receptor mediated uptake. Caveolae are up to now the best-characterized type of micro-domains observed in living cells [Mukerjee & Maxfield, 2004]. Reviews about their composition and function were written by several authors [Anderson, 1998; Anderson & Jacobson, 2002; Parton & Simons, 2007]. Another important class are signalling domains incorporating trans-membrane signalling proteins, for instance IgE-FcεRI [Baird et al., 1999], mediating for example the permittivity of cell membranes. In 1997, Simons and Ikonen postulated the “raft model“ [Simons & Ikonen, 1997], which assumes that sphingolipids, phospholipids and cholesterol form locally ordered lipid clusters, floating as a “raft” in the “see” of matrix lipids (Fig 2.(b)).

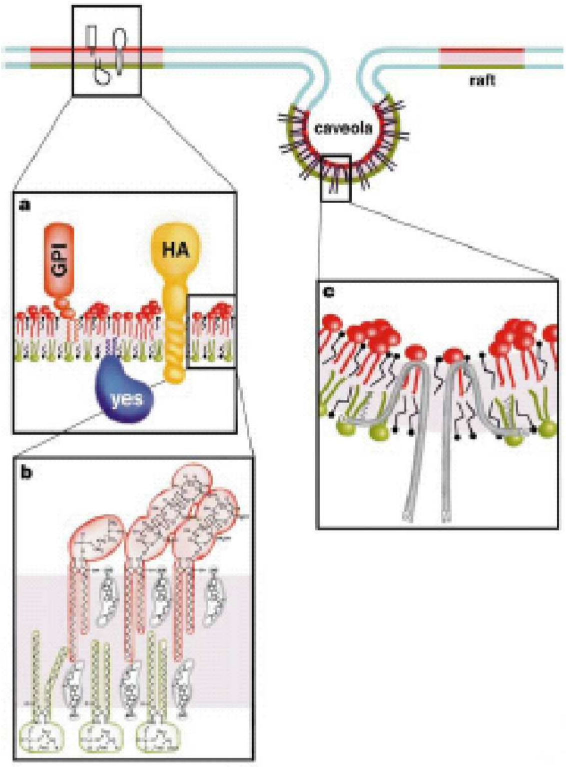

Fig. 2 Schematic illustration of (a) signaling domains, (c) caveolas and the (b) lipid-rafts (from [Simons & Ikonen, 1997])

However, although some studies seem to support the hypothesis, even the size of rafts is still the matter of debate [Jacobson & Dietrich, 1999].
So for instance, the extraction of lipid rafts with non-polar detergents [London & Brown, 2000] would strongly interfere with lipid membranes [Heerklotz, 2002]. On the other hand, an indirect technique like fluorescence resonance energy transfer (FRET) would not be sensitive to the length scale of above 5 nm [Jacobson & Dietrich, 1999; Anderson & Jacobson, 2002].

One of the main obstacles to understand the physical mechanism of micro-domain formations exists in the complex phase diagram of biological membranes that contain different molecular components, which include various phase coexisting regions. To date, most of the attempts to reconstitute lipid rafts in artificial membranes have used a cocktail of lipids that mimic the composition of lipid rafts, such as the molar ratio of 2:1:1 for [phospholipid]:[cholesterol]:[glycosphingolipid] mixtures. Huang and Feigenson proposed a so-called *“umbrella”* effect [Huang & Feigenson, 1999], which assumes small head groups of sterols shielded against the polar water by umbrellas of large phosphate head groups. McConnell and coworkers proposed another approach for the fluid-fluid immiscibility based on the formation of oligomeric complexes composed of cholesterol and phospholipids [McConnell & Radhakrishnan, 2003; McConnell & Vrljic, 2003]. However, almost all domains formed in complex lipid mixtures are found to be either highly polydispersive, or coalesce into large domains, whose diameters is often over several μm.

The main goal of this work is the design of a new class of micro-domains based on synthetic (thus not biological) molecular building blocks. In order to achieve a simple and tuneable phase diagram, the system is designed composed of binary mixtures of synthetic building blocks, which undergo perfect phase separation. Since this is practically impossible by mixing lipids with different lengths of hydrocarbon chains, perfluorinated carbon chains were introduced. This concept has been inspired by the unique feature of fluorocarbon chains: they are not only hydrophobic but also oleophobic. A typical example would be the perfect de-mixing of poly-ethylene and poly-tetrafluoroethylene (Teflon). Actually, surfactants with partially or fully fluoroalkylated hydrophobic tails (F-alkyl chains) have been drawing increasing attentions in recent years for various medical applications such as drug delivery [Kraft & Riess, 1998; Riess & Kraft, 1998; Riess & Greiner, 2000; Riess, 2002].

As preliminary molecular building blocks, several lipids with different fluorocarbon chains and head group functionalities have been custom-designed and synthesized by Dr. Andreea Pasc in our group (now at Univ. Nancy). Fluorocarbon chains take highly ordered, helical conformation within wide temperature ranges, and the fluorinated lipids were doped in the matrix phospholipids, 1,2-dioleoylphosphatidylcholine (DOPC), which is in a fluid phase under all experimental conditions (Fig. 3). The micro-domains were initially formed at the air/water interface under thermodynamic equilibrium, and were transferred onto planar solid supports, called as supported membranes [Brian & McConnell, 1984; Sackmann, 1996; Tanaka & Sackmann, 2005]. The well defined molecular chemistry of fluorinated lipids allowed for quantitative determination of the domain size using a self-developed image analysis routine and grazing-incidence X-ray diffraction technique. Furthermore, owing to the highly mono-dispersive size distribution of the domain size, the lateral correlation between the domains can be described within the framework of colloidal crystallization. The impact of the molecular chemistry (number and length of fluorocarbon chains, head groups) on the domain size has systematically been studied, which enabled to identify the key parameters that determine the domain size. Finally, the surface of custom-designed flat-μ-fluidics chips has been functionalized with the supported membranes that locally display functional saccharides, which can be subjected to study dynamic adhesion of carcinoma cells and bacteria with and without shear fields. The details of the results will be presented in the following chapters.

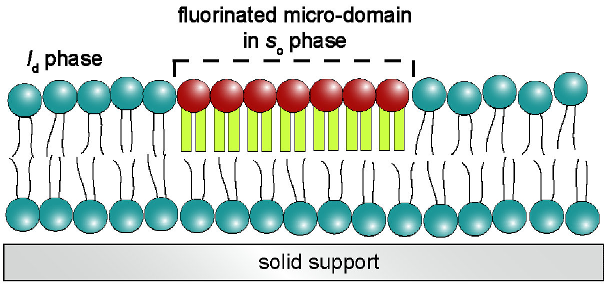

Fig. 3 Schematic illustration of the supported membrane that locally displays fluorinated lipids.

1 Materials and Methods

In this work, self-assemblies of synthesized fluorinated molecules were utilized to structure phospholipid monolayers and to establish bio-functionalized membrane models in μ-fluidic channels. To investigate the formation of such nano-/micro-domains and their strongly correlated arrangements the following preparation methods and characterization techniques were used.

1.1 Materials

1.1.1 Fluorinated Amphiphilic Molecules

The lipid monolayers and bilayer membranes investigated in this work incorporated custom-designed and synthesized fluorinated amphiphilic molecules. The synthesis was performed by Dr. Andreea Pasc (now at University Nancy, France). Details can be found in further publications, currently in preparation [Oelke et al, 2009].

Fluorocarbon chains are characterized by their exceptional chemical and biological inertness, extreme hydrophobicity and oleophobicity, low surface tension, high density, absence of protons and magnetic susceptibility.

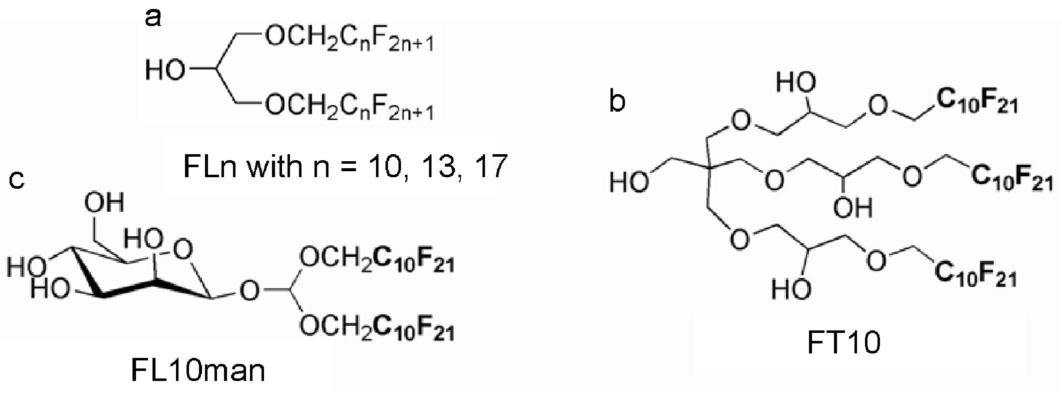

Fig. 1.1 (a) Chemical structure of the fluorinated amphiphilic molecules FLn, with an OH head-group, glycerol backbone and two symmetric fluorocarbon chains, where n = 10, 13 and 17 is the number of fluorocarbon units. (b) Chemical structure of FT10, a three chain molecule and (c) FL10man, a molecule modified with a sugar head-group.

To investigate the influence of the molecular chemistry on the formation of self-assemblies and their correlation within a phospholipid matrix, three classes of fluorinated amphiphilic molecules were synthesized. The different molecules consist of at least two symmetric perfluorocarbon chains connected by a glycerol backbone to a hydrophilic head-group.

(I) With FL10, FL13 and FL17 a set of fluorinated molecules with a varying number of fluorocarbon units (9, 12 and 16 CF_2 units plus one CF_3 chain terminus) was designed to investigate an influence of the chain length (see Fig. 1.1(a)).

(II) The effect of a variation in the number of chains was investigated with the molecule FT10 (see Fig. 1.1(b)). Here, an additional perfluorinated chain was attached to the molecule in contrast to FL10.

(III) FL10man was designed to investigate the influence of a functionalized head-group on the formation of micro-domains and their arrangement. Based on the molecule FL10, the OH head group was here replaced by a more polar α-D-mannose sugar moiety (see Fig. 1.1(c)) to make the molecule bio-functional.

1.1.2 Mannose Binding Cells and Bacteria

E.coli HB101 (pPKl4)

Preliminary adhesion experiments in functionalized μ-fluidic channels were performed with the mannose binding bacteria strain, Escherichia Coli (E.Coli) HB101 (pPKl4), expressing a high amount of FimH binding proteins at their surface. The strain was generously provided by Prof. J. Hacker (Institut für Molekulare Infektionsbiologie, IMIB, Universität Würzburg).

J774 Macrophage

For cell experiments in fluid cells a mannose binding cell line of mouse macrophages *J774* was used, purchased at the "*Deutsche Sammlung von Mikroorganismen und Zellkulturen*"(DSMZ) (Braunschweig, Germany)

1.1.3 Substrates

Glass substrates for lipid monolayer support:

As solid supports for monolayer experiments glass cover slides (dimensions 24 x 24 mm, thickness 0.17 mm) from Marienfeld (Lauda-Königshofen, Germany) were used.

For further experiments the glass slides were cleaned following the procedure reported by Purrucker [Purrucker, 2004].
In short:

- Ultrasonication (3min) and subsequent rinsing with acetone and methanol
- Ultrasonication in a solution of 1:1:5 (v/v) H_2O_2 (30%) : NH_4OH (30%) : water for 5 min , and
- soaking in the same solution for another 30 min at 60°C [Kern & Puotinen, 1970].
- Finally, they were rinsed intensively with water, dried at 70°C, and stored in sealed glass boxes.

$LiNbO_3$ substrates for μ-fluidic channel preparation

The piezoelectric substrate for the preparation of the μ-fluidic setup was a 128° Y-cut, X-propagation $LiNbO_3$ single crystal purchased from Advalytix AG (Munich, Germany). After an gold layout was applied as electric circuit to the surface the crystal was subsequently coated with a thin layer of SiO_2 to passivate the material. Further details of the final μ-fluidic channel preparation can be found in Chapter 4.

1.1.4 Chemicals and Buffers

If not stated otherwise, all chemicals were purchased from Sigma-Aldrich (Munich, Germany) and used without further purification.

Phospholipids:

In this study the following commercial lipids were used without further purification

- 1,2-dioleo-*sn*-glycero-3-phosphocholine (DOPC) purchased from Avanti Polar Lipids Inc. (Alabaster, AL)
- 1,2-dihexadecanoyl-sn-glycero-3-phosphoethanolamine triethylammonium salt (Texas Red-PE) from Molecular Probes (Leiden, Netherlands). This fluorescence probe is excited at 582 nm and emits at 601 nm.

The chemical structures for both commercial lipids can be found in Appendix A1.

Lipid monolayer support:

Glass substrates were functionalized with the commercially available silane octyltrimethoxysilane (ODTMS), purchased from ABCR (Karlsruhe, Germany), following the procedure published by Mooney et al. [Mooney et al., 1996] and Hillebrandt & Tanaka [Hillebrandt & Tanaka, 2001] to serve as solid support for a lipid monolayer.

Photolithography:

For fabrication of flat-μ-fluidic channels the following chemicals were used:

- The positive photoresist S1813 from Shipley purchased at Resist Technology GmbH (Berlin, Germany) was used to prepare the channel layout on the SiO_2 passivated $LiNbO_3$ chip.
- The negative photoresist SU-8/100 from MicroChem (Newton, Massachusetts, USA) purchased at Micro Resist Technology GmbH (Berlin, Germany) was used to form casting moulds.

Protective Sheets:

As protective sheet during the lipid monolayer deposition the organic polymer polydimethylsiloxan (PDMS) Sylgard 184 purchased at SASCO Holz GmbH (Putzbrunn, Germany) was used.

Buffers:

For all aqueous solutions, water from a Millipore purification systems (R > 18 MΩcm, Millipore, Molsheim, France) was used.
The buffer used in preliminary bacterial adhesion experiment was *PBS*, at 150 mM NaCl (pH 8.0).

Cell Medium:

The medium used for cell culture and μ-fluidic experiments was RPMI 1640 from PAA purchased at Biochrom (Berlin, Germany).

Solvents:

For stock solution of lipids and for the artificial fluorinated molecules trichlormethane (Chloroform) was used, together with 1,1,2-trichlortrifluoroethane bought from Riedel De Haen in a mixing ratio of 1:1.

1.2 Film Balance

For the preparation of lipid monolayers several Langmuir trough film balances were used all equipped with Wilhelmy plate surface tension sensors [Gaines, 1966]. Short descriptions of the used film balances can be found in the following, listed by their application.

Langmuir-Schaeffer monolayer deposition could be performed with all in following mentioned film balances. In contrast Langmuir-Blodgett depositions were only feasible with two film balances equipped with a dipping well.

First a self-built film balance using one barrier was used with a subphase area of 1008 cm^2. The pressure sensor was a filter paper platelet as Wilhelmy plate with a resolution of approximately $\Delta\Pi = \pm 0.01$ mN/m.

Additionally a standard film balance with one barrier *601A*, bought from Nima Technology Ltd. (Coventry, England) was used again with a filter paper platelet as Wilhelmy plate sensor. The subphase area of the 601A was 900 cm^2 and the resolution of the sensor was $\Delta\Pi = \pm 0.01$ mN/m [Nima homepage, 2008].

The imaging of free floating monolayers at the air/water interface was done with a film balance equipped with an additional window at the trough bottom. This two barrier *Minitrough* film balance was bought from KSV Instruments Ltd. (Helsinki, Finland) and had a subphase area of 274 cm^2. It utilized a Pt-platelet as Wilhelmy plate sensor with a resolution of $\Delta\Pi = \pm 0.004$ mN/m [KSV Homepage, 2008].

For surface potential measurements a film balance *MicroTroughX* bought from KIBRON (Espoo, Finland) was used, additionally equipped with a surface potential sensor. This film balance has a subphase area of 462 cm^2, a surface pressure resolution of $\Delta\Pi = \pm 0.01$ mN/m and a surface potential resolution of $\Delta V = \pm 1$ mV [KIBRON homepage, 2008]

If necessary in the following the film balances are named with their manufacturer names *KSV*, *self-built*, *Nima* and *KIBRON*.

1.2.1 Film Balance Technique

A monolayer of amphiphilic molecules is spread on an aqueous subphase in a Langmuir trough. The area of the spread monolayer can be controlled by either one or more barriers. An exemplary two barrier Langmuir film balance with surface pressure and surface potential sensor is depicted in Fig. 1.2.1.

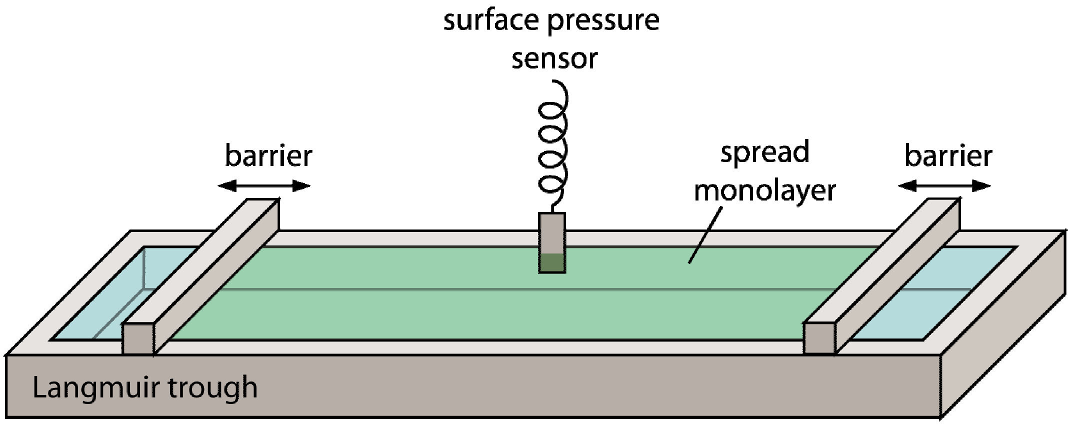

Fig. 1.2.1 Sketch of a two barrier Langmuir film balance with Wilhelmy plate surface pressure sensor. The sensor is placed in the middle the trough to measure a monolayer of amphiphilic molecules spread and compressed at the air/water interface between the barriers.

The presence of an amphiphilic molecule at the air/water interface alters the surface tension γ of the system with respect to the tension of pure water γ_{water}. The surface pressure Π is defined as,

$$\Pi = \gamma_{water} - \gamma, \tag{1.1}$$

and can be measured by the technique of the Wilhelmy plate. Therefore a thin hydrophilic platelet, either a simple filter paper or a Pt-platelet, with known geometry, is attached to a sensitive spring, with known spring constant [Gaines, 1966].

1.2.2 Pressure-Area Isotherms

The Π-A-isotherm is a simple way to determine properties of amphiphilic molecule monolayers, like molecular area A_{mol}, monolayer phase and phase transition pressures and molecular compressibilities [Dynarowicz-Latka et al., 2001]. The surface pressure Π is measured at constant temperature T as a function of the area A, which can be controlled by the position of the barrier.

To form pure monolayers of fluorinated molecules or mixed monolayers of fluorinated molecule/phospholipid at the air/water interface a sufficient amount of mixture of lipid mixture solved in chloroform and trichlortrifluoroethan was used. The solvents were mixed in a ratio of 1:1. During the monolayer experiments the temperature was kept constant at T = 20°C by an external temperature control unit. After a sufficient time for solvent evaporation $t > 45$ min the monolayer was compressed by closing the barriers while the surface pressure and barrier position was recorded.

1.2.3 Surface Potential *V* of Langmuir Monolayers - *ΔV*-Area Isotherms

A film balance equipped with an additional surface potential sensor was used to record *ΔV*-A-isotherms in parallel to *Π*-A-isotherms. The used sensor was based on the so-called vibrating capacitor technique, a modification of the Kelvin probe principle [Dynarowicz-Latka et al., 2001].

A capacitor electrode plate is placed in a short distance (~2 mm) above the air/water interface, while a counter electrode plate is placed onto the bottom of the Langmuir trough (Fig. 1.2.2).

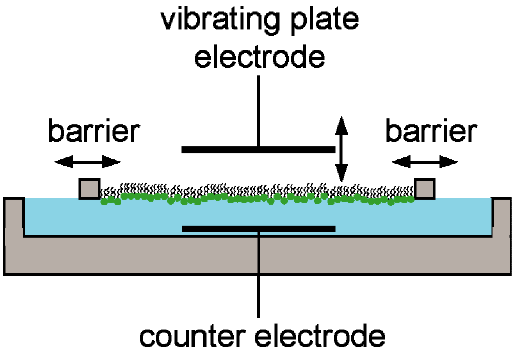

Fig. 1.2.2 Sketch of a surface potential setup, using a vibrating plate capacitor.

The vibrating plate electrode oscillating at fixed frequency causes an effective output voltage that is characteristic for various dielectric layers water, molecule and air in between the two capacitor plates. After a calibration measurement of a clean air-water surface, the application of an additional lipid monolayer alters the effective surface potential and the difference between the potentials *ΔV* of the spread monolayer at the air/water interface V_{layer} and the clean surface V_{water} is given as,

$$\Delta V = V_{layer} - V_{water}\ . \tag{1.2}$$

Comparable to the behavior of thin films on metal plates, amphiphilic molecules can possess a dipole moment μ and therefore change the surface potential of the clean water surface V_{water}. The change in surface potential *ΔV* for a monolayer of uncharged molecules is, according to Gaines [Gaines, 1966], given by

$$\Delta V = \frac{m_\perp}{\varepsilon} = \frac{\mu_\perp}{\varepsilon A_{mol}}\ . \tag{1.3}$$

Here, $m_\perp$ is the dipole density normal to the air/water interface and ε is the relative dielectric constant of the monolayer. The molecular dipole moment $\mu_\perp$ perpendicular to the surface is then given by $\mu_\perp = m_\perp \cdot A_{mol}$.

1.2.4 Langmuir-Blodgett Deposition (LB)

As preparation method of monolayers for lower leaflets of asymmetric membranes the Langmuir-Blodgett technique was used [Blodgett, 1934; Blodgett, 1935; Blodgett & Langmuir, 1937].

The trough of a one barrier film balance is therefore equipped with a dipping well, placed at the opposing site of the barrier, as shown in Fig. 1.2.3(a).

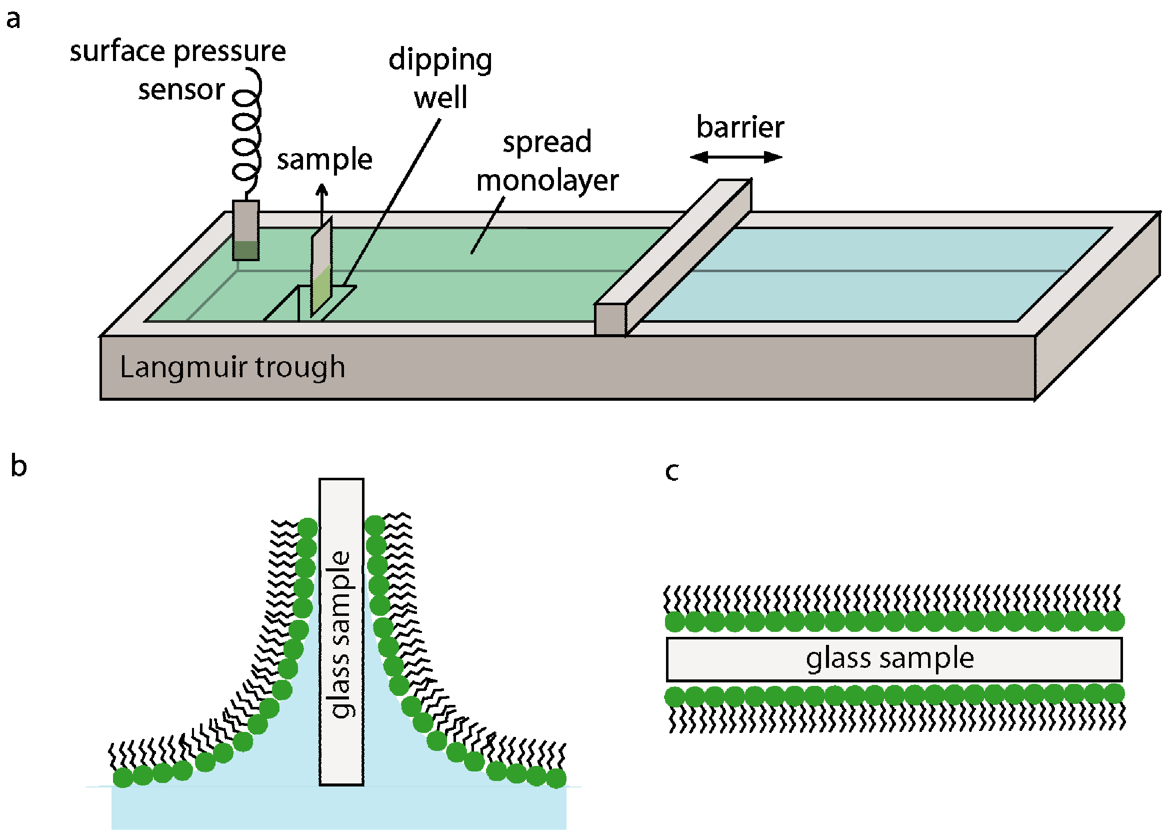

Fig. 1.2.3 (a) Sketch of a film balance setup with dipping well and sample lift. (b) The beforehand immersed hydrophilic sample is lifted at a target pressure Π_T. (c) A schematic drawing of a LB transferred monolayer on a hydrophilic glass sample.

A sample lift is installed directly above the dipping well in order to fix a hydrophilic glass sample immersed into the subphase during the solved molecule mixture was spread to the air/water interface (see Fig 1.2.3(b)). After solvent evaporation and film compression to a lateral target pressure Π_T the substrate is pulled out at a constant transfer velocity of $v_T = 2\ \mathrm{mms}^{-1}$ and the film was deposited while the lateral pressure was kept constant by a control unit. Fig. 1.2.3(c) shows the monolayer coated glass sample, where the lipid monolayer is transferred on both sides with the head groups oriented to the glass surface.

1.2.5 Langmuir-Schaeffer Deposition (LS)

The transfer of a monolayer of amphiphilic molecules from the air/water interface to a glass surface with the hydrophobic chains pointing to the solid support can be done by the Langmuir-Schaeffer technique. This transfer technique was used to build up the upper leaflet of a lipid bilayer, as reported by Tamm & McConnell [Tamm & McConnell, 1985] and Charitat et al. [Charitat et al., 1999].

A monolayer of amphiphilic molecules is spread to the air/water interface of a Langmuir trough. After solvent evaporation and compression to a target pressure π_T, a hydrophobic glass sample is dipped onto the lipid monolayer (see Fig. 1.2.4(a)).

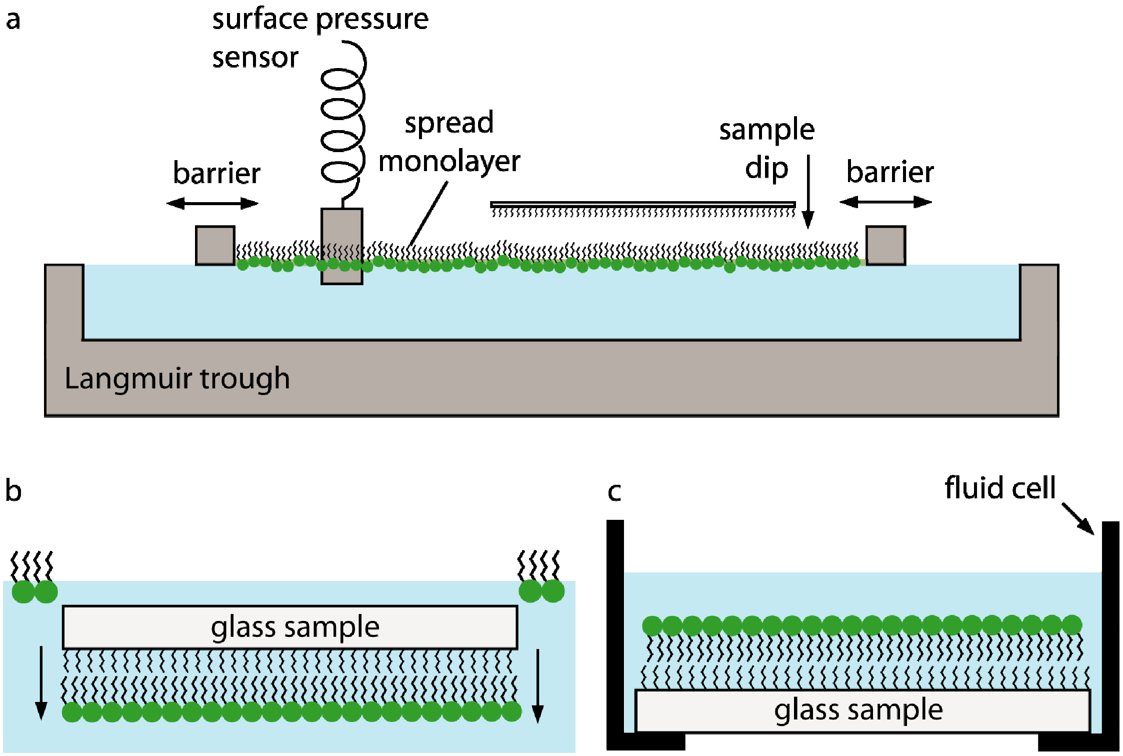

Fig. 1.2.4 (a) Sketch of a film balance setup for the procedure of a Langmuir-Schaeffer deposition. The monolayer is compressed up to a target pressure Π_T. (b) After equilibration a hydrophobic sample is dipped onto the monolayer. (c) A schematic drawing of LS transferred monolayer onto a hydrophobic glass sample mounted in a fluid cell.

Since the LS transferred lipid monolayer is unstable in air, the floating glass sample is pushed through the air/water interface horizontally as depicted in Fig. 1.2.4(b) and mounted in a half open fluid cell (see Fig. 1.2.4(c)). In the resulting surface supported monolayer, the hydrophobic anchor chains are pointed towards the hydrophobic substrate, while the hydrophilic head groups are accessible from the bulk.

1.3 Fluorescence Microscopy

For the visualization of fluorescence images, the following objectives were used in an inverted fluorescence microscope (Axiovert 200, Carl Zeiss, Göttigen, Germany)

- 20x long distance (LD) objective (Achroplan, N.A. 0.40),
- 63x long distance (LD) objective (Achroplan, N.A. 0.75) and
- 100x oil immersion,

purchased from Carl Zeiss.

As filter set for the used fluorescence probe Texas Red a combination of exciter (560/40 nm), dichroic mirror (585 nm) and emitter (630/75 nm) was used. Optional to the commonly used X-Y-sample stage, (see Fig. 1.3(a)), a Langmuir trough equipped with a window, was mounted on top of the microscope, replacing said sample stage, as depicted in Fig. 1.3(b). This setup allows for taking images of the fluorescence labeled monolayer through a glass window during and after the compression.

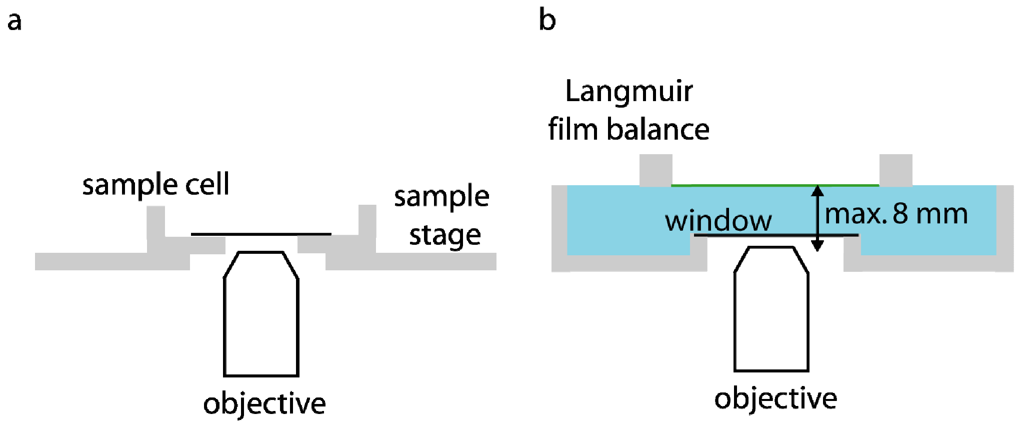

Fig. 1.3 Sketch of the inverted microscope setup with (a) sample cell and (b) Langmuir trough equipped with a observation window.

For μ-fluidic experiments (see Chapter 4) the 20x LD objective was used in a standard upright microscope (Helmut Hund, Wetzlar, Germany).

1.4 Effective Micro-Domain Potential - Potential of Mean Force –*ßw*(*r*)

In natural membranes, functional lipid micro-domains are postulated to play a key role in complex cellular functions [Simons & Ikonen, 1997]. Their formation and distribution in natural systems has been studied before [Gege et al., 2004].

The lateral distribution of fluorinated micro-domains, as depicted in Fig. 1.4.1 was studied by image processing. The calculated radial distribution function $g(r)$ and the potential of mean force $-ßw(r)$, the effective inter-particle potential of micro-domains, give a measure of the structure in the arrangement of detected micro-domains within the lipid bilayer membrane.

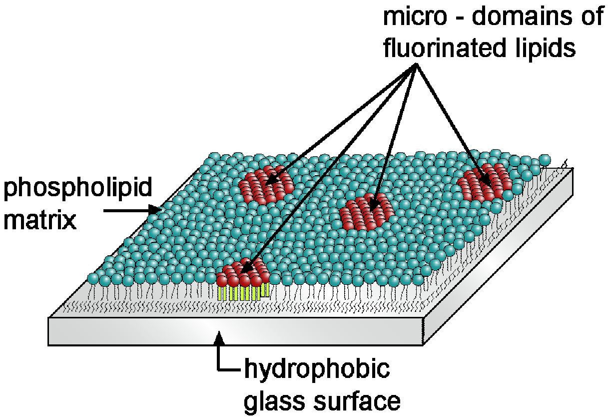

Fig. 1.4.1 Sketch of a supported monolayer on a hydrophobic glass surface structured with micro-domains of the fluorinated molecules.

Samples for image processing were Langmuir-Schaeffer transferred mixed lipid monolayers at various molar fractions χ of fluorinated molecules, incorporated in a phospholipid matrix of 1,2-dioleo-*sn*-glycero-3-phosphocholine (DOPC). To visualize the micro-domains the fluorescence tracer 1,2-dihexadecanoyl-sn-glycero-3-phosphoethanolamine triethylammonium salt (Texas Red-PE), was added in a molar fraction of 0.1 to 0.2 mol% into the stock solutions. Texas Red-PE preferentially locates in the more disordered “liquid expanded” phase of DOPC and is expelled from the highly ordered phase of the fluorinated molecules. Therefore the micro-domains appear as black spots. At least 50 images for each transferred monolayer were taken, stored in a stack and processed afterwards.

1.4.1 Image Processing

The images were processed with the image analysis software “Cellenger Developer Studios” (Definiens AG, Munich, Germany) to define single micro-domains of fluorinated molecules in the transferred monolayer according the following steps:

- Select pixels below a distinct brightness threshold and define them as segment of a micro-domain
- Select pixels below a distinct next pixel contrast threshold and define them as segment of a micro-domain
- Merge the previously selected, neighboring pixels to form a single compact domain (red)
- Discard all domains below an area of 4 pixels
- Define all not selected pixels as background (blue)

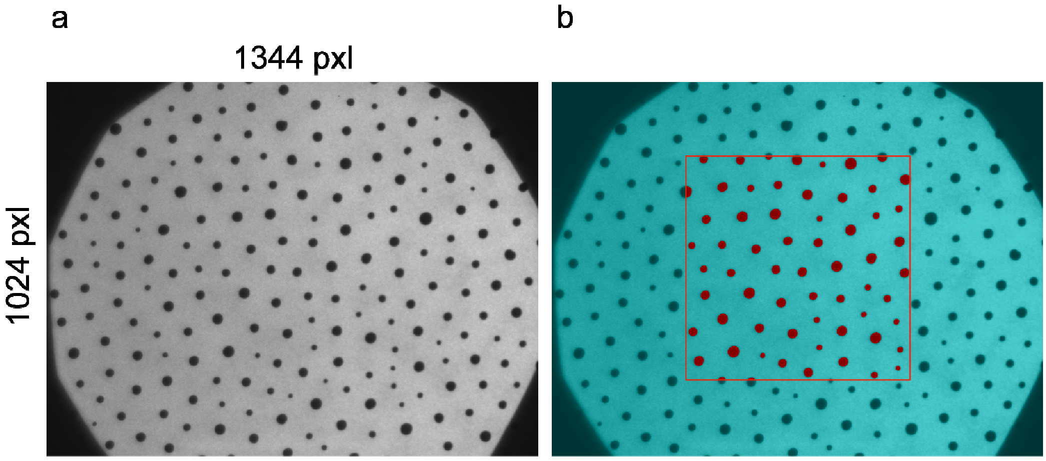

Fig. 1.4.2 (a) Fluorescence image of a transferred monolayer (b) after image analysis a red bordered region of interest was analyzed. Red spots are detected micro-domains, while the blue area is the surrounding matrix.

A fluorescence image of a monolayer incorporating fluorinated domains is shown in Fig. 1.4.2(a). The correspondent processed image is shown in Fig. 1.4.2(b).
In the region boarded with a red frame, the red highlighted particles represent detected micro-domains, while the surrounding matrix of phospholipids is homogeneously colored in blue.

After processing a stack of images, the information about the absolute positions in each picture and the area of micro-domains was stored and used afterwards to determine a radial distribution.

1.4.2 Radial Distribution Function *g*(*r*)

The calculation of a radial distribution function *g*(*r*) is a convenient and common method to obtain structural information of colloidal suspensions [Hansen, 2007; Israelachvili, 1991; Belloni, 2000; Quesada-Pérez et al., 2002]. Beside this it was already used to characterize two-dimensional colloidal systems shown by Brunner et al. and Quesada et al. [Quesada-Pérez et al., 2001; Brunner, 2003].
Since fluorinated molecules form micro-domains comparable to colloidal crystals (see Chapter 2.1) a radial distribution function *g*(*r*) was determined, to derive information about the particle correlations.

Starting from a selected micro-domain (see in Fig 1.4.3(left) colored in black) the number ΔN of micro-domains located in a ring with width Δr were counted.

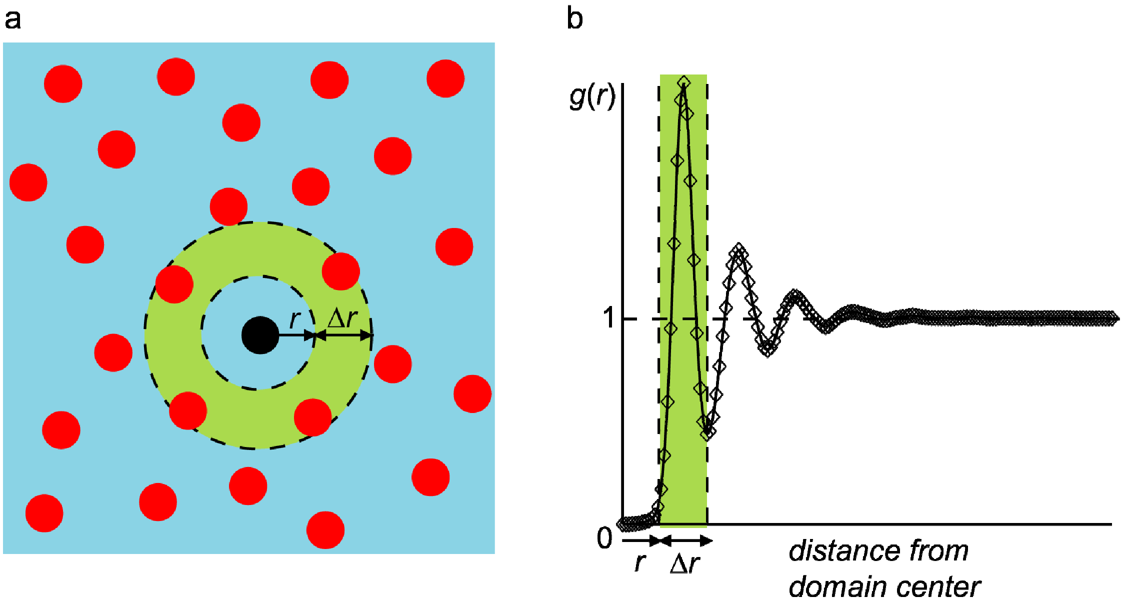

Fig. 1.4.3 (a) Sketch of the micro-domains (red) arranged in the matrix of phospholipids (blue)
(b) the radial distribution function *g*(*r*) vs. the distance from the domain center

The density distribution $\rho_{\mathrm{SD}}(r)$ for a single micro-domain is obtained by dividing ΔN by the area ΔA of the correspondent ring:

$$\rho_{SD}(r) = \frac{\Delta N(r+\Delta r)}{\Delta A(r+\Delta r)}. \tag{1.3}$$

Subsequently $\rho_{\mathrm{SD}}(r)$ is normalized by the total density of the frame ρ_{tot} to obtain the radial distribution function $g_{\mathrm{SD}}(r)$ of a single micro-domain:

$$g_{SD}(r) = \frac{\rho_{SD}(r)}{\rho_{tot}}. \tag{1.4}$$

More than 2000 domains in >50 images were analyzed according to the reported procedure. The total radial distribution function $g(r)$ is obtained as a sum of all $g_{\mathrm{SD}}(r)$, normalized by the total number of analyzed micro-domains N_{tot},

$$g(r) = \frac{\sum g_{SD}(r)}{N_{tot}}. \tag{1.5}$$

Exemplarily the radial distribution function $g(r)$, for a quasi hexagonal arrangement of particles can be seen in Fig. 1.4.3(right). The oscillation of the radial distribution function around $g(r) = 1$ implies the quasi hexagonal structure in the arrangement of particles around the starting particle. The centre of the first second or additional rings with high density of particles around the starting particle can be determined from the maxima position in the radial distribution function.

1.4.3 Potential of Mean Force –*ßw*(*r*)

Usually three different potentials in a system of colloidal particles can be distinguished as the direct pair potential, the solvent-averaged effective pair potential and the mean force potential [Belloni, 2000].

In general a pair interaction between neighboring particles can be separated in two contributions (I) an attractive short range and (II) a repulsive long-range interaction, dependent of the particle nature like shape and charge. These interactions can be modeled by various types of potentials, for instance a hard-sphere, soft-sphere, Lennard-Jones or square-well potential.

Two particles interact via a pair potential $u(r)$ with each other. If mediating and averaging effects of a solvent between the particles have to be taken into account an effective pair interaction $u^{eff}(r)$ may be defined.

In the case of a multi-particle system the interaction between two particles is not only influenced by their own pair interaction, but also by contributions of the neighboring particles. Therefore the potential determined from the radial distribution function is a potential of mean force $w(r)$, representing all existing interactions between the particles in a defined region.

The potential of mean force $w(r)$ is calculated from the radial distribution function $g(r)$ according to the inverse work theorem [Hansen, 2007],

$$-\beta w(r) = \ln[g(r)]. \tag{1.6}$$

where $\beta = 1/k_B T$. The potential for the exemplarily particle distribution (see Fig. 1.4.3(a)) is shown in Fig 1.4.4(a).

1.4.4 Molecular Spring Model

A spring model interconnecting the micro-domains by springs with defined constant *k*, as depicted in Fig. 1.4.4(b) is an appropriated model to describe a colloidal system at given boundary conditions with an interacting potential –*ßw*(*r*) [Nikolaides et al., 2002]. The shape of the determined potential of mean force –*ßw*(*r*) can be estimated around the position of the first minima with a harmonic potential *v*(*r*):

$$v(r) = v(r_1) + \frac{1}{2} k`r , \tag{1.7}$$

where *k*' is the spring constant representing the strength of the interacting potential and $v(r_1)$ is the initial potential at the position of the first order minimum.
The spring constant *k*’ is a measure for the displacement of a single micro-domain around the first minimum r_1 and therefore for the strength of the potential of mean force.

In Fig. 1.4.4(a) the harmonic potential, calculated by Equation (1.7) is illustrated by a red fit.

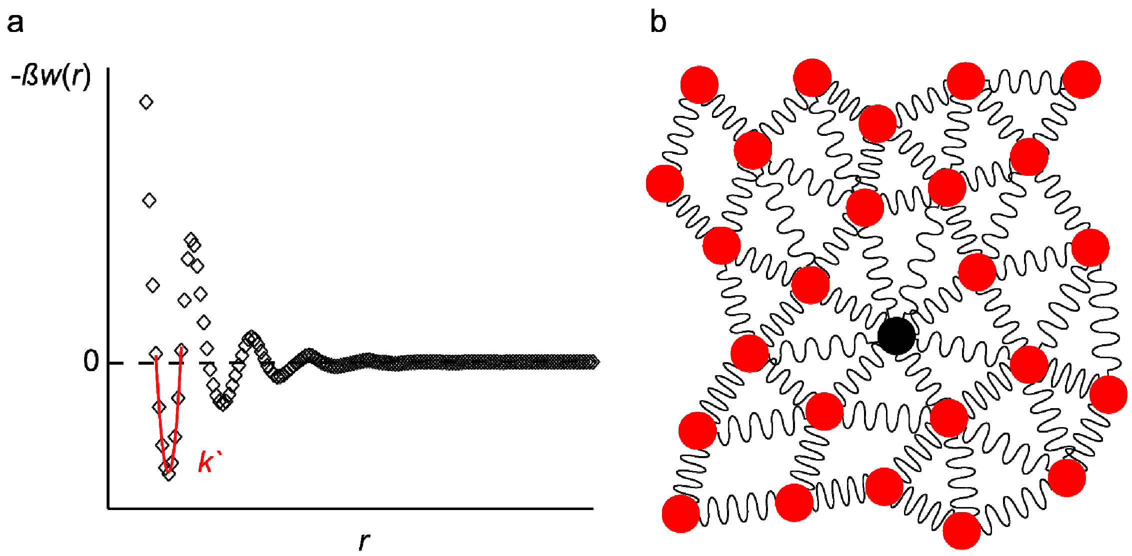

Fig. 1.4.4 (a) Potential of mean force -*ßw*(*r*) calculated from the radial distribution function *g*(*r*) using the inverse work theorem [Hansen, 2007]. (b) A lattice of colloidal molecules connected by imaginary springs.

1.5 Grazing Incidents X-Ray Diffraction (GIXD)

As an applicable technique to investigate the molecular structure of two-dimensional surfaces at the air/water interface grazing-incidence X-ray diffraction (GIXD) was used. Experiments employing this technique have already been performed for instance with two dimensional lattices of quantum dots, with monolayers formed by amphiphilic molecules or in particular with partially fluorinated molecules [Wiegart et al., 2005; Metzger et al., 1999; Barton et al., 1991].

1.5.1 Diffraction Geometry

A sample is placed on the sample stage of the experimental setup. The incoming X-ray beam k_i hits the sample below 80% of the critical angle α_c and is totally reflected. An evanescent wave is exited along the footprint of the incoming k_i beam and diffracts at the lateral two-dimensional lattice of the monolayer.

In Fig. 1.5.1(a) a schematic view from the top of the setup is presented, in (b) the diffraction geometry of the beam is depicted.

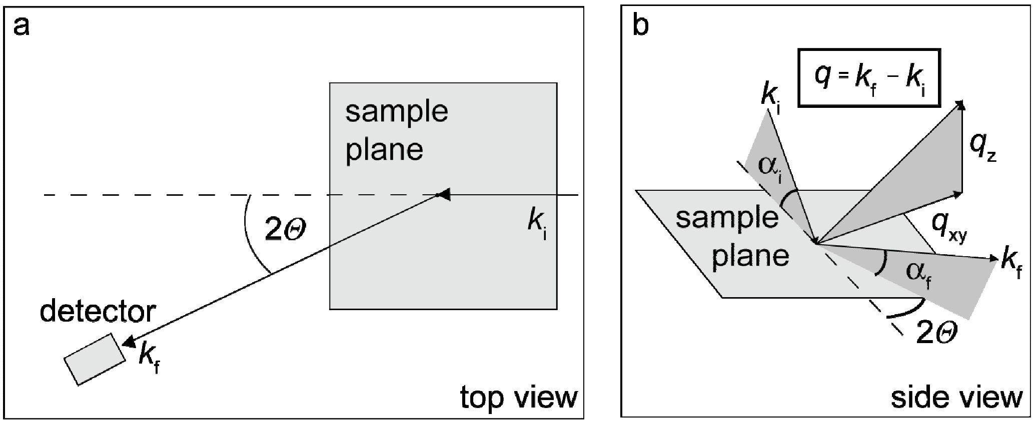

Fig. 1.5.1 Sketch of the ID10B GIXD setup at the ESRF (a) top view, (b) diffraction geometry.

In a two-dimensional lattice of ordered molecules, the above mentioned scattering geometry confines the scattering vector and exhibit Bragg rods (see Fig. 1.5.2) where the Bragg condition

$$\lambda = 2 d_{xy} \sin(\Theta_\mathrm{B}), \tag{1.8}$$

is fulfilled. In Equation (1.8), d_xy is the correlation length, representing the lattice spacing within the sample and Θ_B is the Bragg angle, corresponding to an angle of 2Θ in the GIXD setup, see Fig. 1.5.1(a).

The lateral scattering vector q_{xy}, in reciprocal space can be recalculated from the correlation length d_{xy} by the relation

$$q_{xy} = \frac{2\pi}{d_{xy}}. \tag{1.9}$$

Using Equation (1.9), the Bragg Relation (1.8) can be rewritten as

$$q_{xy} = \frac{4\pi}{\lambda}\sin(2\Theta), \tag{1.10}$$

with respect to the reciprocal lattice vector q_{xy}.

The diffracted beam fraction k_f is finally detected with a position sensitive detector (PSD). Since a line-detector was used as PSD in the experimental setup, a diffraction contribution of k_f in z-direction has also to be considered. For this contribution a vertical scattering vector q_z is given by

$$q_z = \frac{2\pi}{\lambda}\sin(\alpha_f). \tag{1.11}$$

In the two-dimensional lattice of rod-like molecules three possible closest packing structures (shown in Fig. 1.5.2) can be considered as reported by Als-Nielsen et al. [Als-Nielsen et al., 1994].

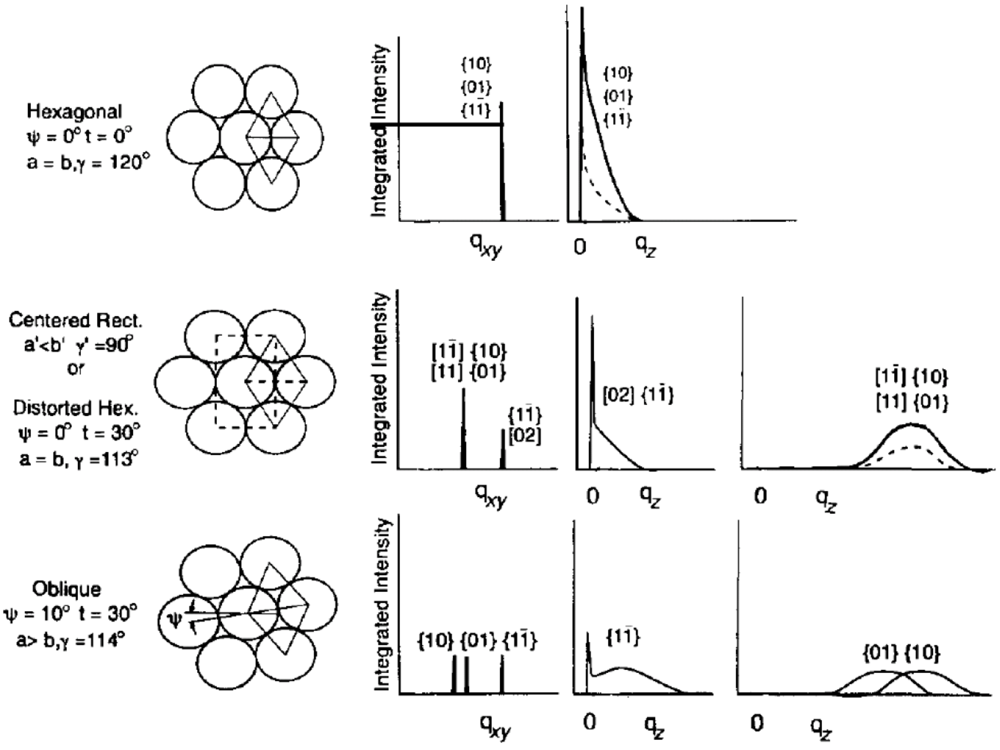

Fig. 1.5.2 Possible structures and diffraction of rod like molecules in a monolayer (from [Als-Nielsen et al., 1994]).

In the special case of a molecule oriented perpendicular to the air/water surface, the intensity along the Bragg rod exhibits a maximum at $q_z = 0$. For molecules tilted with respect to the air/water interface, the intensity maximum in the reciprocal intensity map can shift in q_z and q_{xy}.

1.5.2 Experimental Setup

Grazing-incidence X-ray diffraction experiments were performed at the beam-line ID10B (TROIKA II) of the European Synchrotron Radiation Facility (ESRF) (Grenoble, France). Its high flexibility in performing air/water, air/solid and water/solid experiments has already been reported [Smilgies et al., 2005].

Lipid monolayers were spread on the Langmuir trough mounted in horizontal alignment onto the sample stage of the beam-line. A monochromatic incident beam ($\lambda = 1.54$ Å) was extracted from the synchrotron beam using a diamond [111] double crystal, impinging on the sample at an incident angle of $\alpha_i = 0.18°$, which is approximately 80% of the angle of total reflection for water at this wavelength. The Langmuir trough was sealed for the measurements by a plastic hard-cover with Kapton foil windows and purged with humidified He_2 to avoid further scattering in air and to minimize radiation damage by oxygen radicals. The enclosed oxygen concentration was therefore reduced below a level of 0.1 %.

Between Langmuir trough and line detector an evacuated Soller collimator was placed to suppress further scattering in air and to increase the signal at the PSD. The collimator collected the diffracted beam under an angle of 0.08° which corresponds to a maximum angular resolution of $\Delta q_{xy} = 6 \cdot 10^{-3}$ Å^{-1} for the Soller setup.

2 Two-Dimensional Colloidal Crystals of Self Assembled Fluorinated Lipid Domains

2.1 Introduction

In this chapter, the properties of synthetic fluorinated molecules to de-mix and self-assemble into micro-domains in presence of a phospholipid matrix, will be representatively demonstrated for the fluorinated compound FL17 dispersed in a matrix of DOPC.

As introduced in Chapter 1.1.1 the molecule FL17 is composed of two chains with 16 CF_2 subunits and one CF_3 terminal unit. In Fig. 2.1 the space filling model of FL17 is presented.

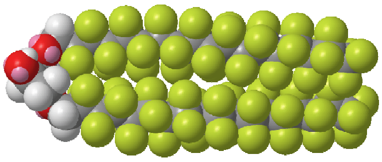

Fig. 2.1 A so-called space filling model of the fluorinated compound FL17 [created in ChemDraw by Dr. Andreea Pasc]. Fluor atoms are indicated as green spheres, while oxygen is colored in red, hydrogen in white and carbon in grey.

Here, the two fully fluorinated chains are indicated by green spheres representing flour and grey spheres representing carbon atoms. The molecular backbone connecting the fluorinated chains with an OH head-group is small compared to the chains and has therefore no influence on the unique de-mixing properties of the molecule. Within this backbone red colored spheres represent oxygen and white spheres hydrogen.

Mixed FL17/DOPC monolayers at various molar fractions χ_{FL17} of FL17 were transferred onto hydrophobic glass surfaces at a defined transfer pressure Π_T. Fluorescence images of the transferred monolayer were made and by image processing FL17 micro-domains could be detected and highlighted.

From this specific parameters of the investigated system, such as the domain area the center-to-center distances were obtained wherefrom the mean micro-domain diameter $<d_{\mathrm{FLl7}}>$, the mean distance between domain centers $<r_{\mathrm{FLl7}}>$, the radial distribution function $g_{FL17}(r)$ and the mean force potential –ß$w_{\mathrm{FL17}}(r)$ could be extracted. Spring constants k' could be derived from the first minimum of the potential of mean force assuming a harmonic potential. These spring constants provide a quantitative measure for the potential strength.

To determine the chain-chain correlation within the micro-domains in mixed monolayers, grazing incidents X-ray diffraction (GIXD) measurements were performed. A scattering length (which corresponds to the distance between scattering layers, formed by the ordered arrangement of the fluorinated molecules) was calculated from the Full Width at Half Maximum (FWHM) of the measured peaks.

2.2 Monolayer Transfer and Image Processing

Mixed phospholipids monolayers incorporating FL17 at molar fractions χ_{FL17} = 5, 10, 20 and 33 mol% were spread from stock solutions and compressed to a transfer surface pressure of Π_T = 25 mNm^{-1}. After compression and subsequently equilibration the monolayers were transferred by LS-transfer technique from the air-water interface onto a previously cleaned, hydrophobized glass surface.

The stability of micro-domains and their arrangement was proved by the comparison of fluorescence images of the monolayers taken both at the air-water interface and after transfer onto the solid substrate. Since the two kinds of images were found to be identical (see Chapter 3.2), the transferred monolayers were used for further image processing. More than 50 images of a single transferred monolayer were taken at various locations of the monolayer to reduce the impact of either locally confined substructures or damaging effects of the transfer in the arrangement of the micro-domains. For each molar fraction a stack of images was acquired.

Fig. 2.2.1(a) presents a transferred fluorescence image of the monolayer with χ_{FL17} = 33 mol%, in which FL17 micro-domains can be identified as dark spots.

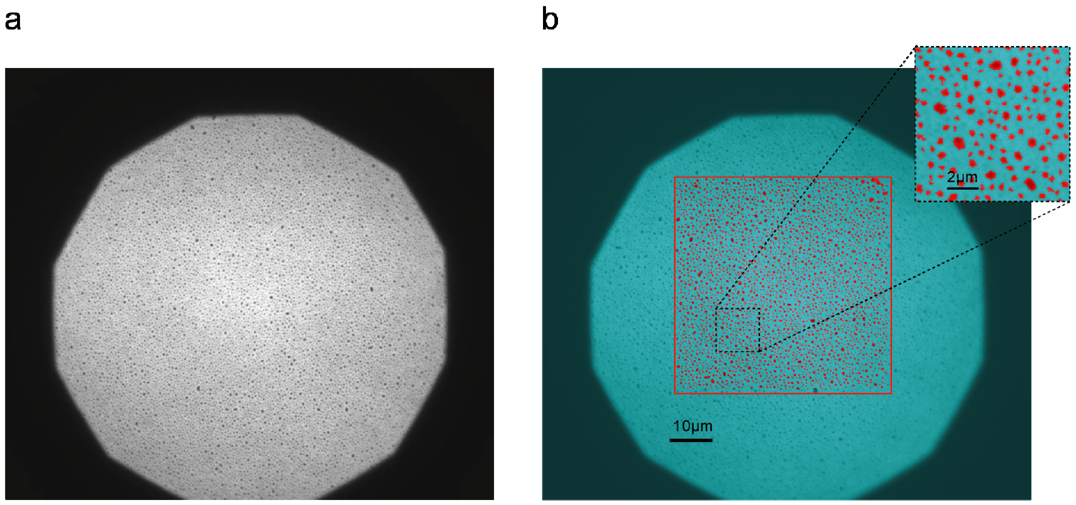

Fig. 2.2.1 (a) Fluorescence image of a transferred monolayer at a molar fraction of χ_{FL17} = 33 mol%. (b) The identical image after processing, whereby the red frame represents a region of interest with a size of 50x50 μm. Red spots represent detected micro-domains, while the blue area corresponds to the surrounding matrix. As an inset a more detailed zoom-in is shown to visualize the micro-domain/matrix detection.

Owing to the fact that fluorocarbon chains of fluorinated molecules take a solid, helical conformation even at low surface pressure (this was verified by wide angle X-ray scattering (WAXS) measurements, see Appendix A.3 for more details), so that the used fluorescent lipid tracer Texas Red-PE is excluded from the fluorinated micro-domains into the fluid lipid phospholipids matrix.

The image processing was done by a self-developed routine as reported in Chapter 1.4.1and results in a 50x50 μm region of interest where detected micro-domains were highlighted in red, while the phospholipid matrix was colored in blue as shown in Fig. 2.2.1(b). To better visualize the detected micro-domains a zoom-in is shown in Fig. 2.2.1(b) as an inset.

2.2.1 Fast Fourier Transform (FFT) of Mixed Monolayer Images

A two-dimensional Fourier transform of the stack of images was performed to obtain the characteristic length scales of the ordered domains.

For the processed image stack of the transferred monolayer with a molar fraction χ_{FL17} = 33 mol% (shown in Fig. 2.2.1(a)), the Fourier transform is presented in Fig. 2.2.2(a).

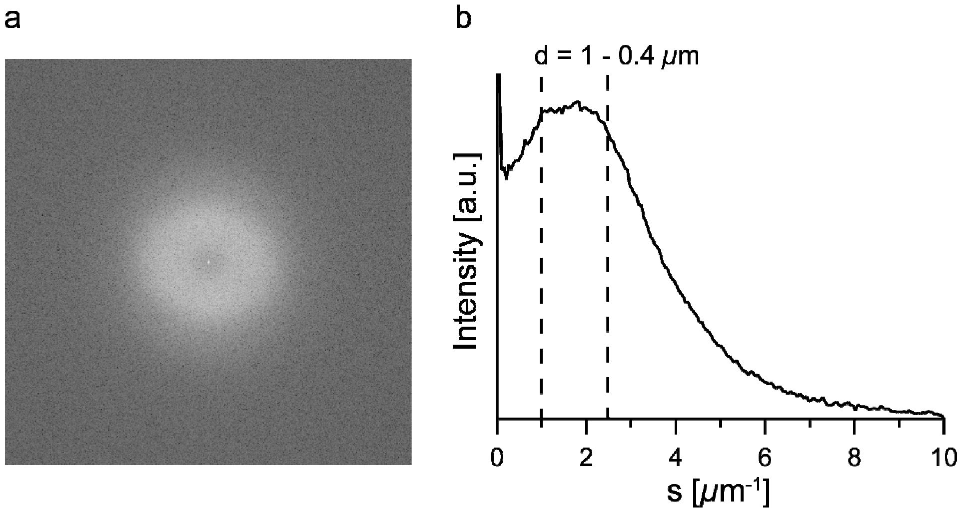

Fig. 2.2.2 (a) A two dimensional Fast Fourier Transformation (FFT) of the stack of images (b) the radial integration of the FFT around the center shows a plateau representing the characteristic lengths for the micro-domains of 0.4 to 1 µm.

A circular halo is observed close to the center of the reciprocal image. The radial integration of the circular halo, presented vs. the reciprocal length *s* in Fig. 2.2.2(b) exhibits a plateau, reflecting the characteristic lengths scales of the sample structure of about 0.4 to 1 μm. This coincides with the lateral dimensions of micro-domains and their mean distance respectively.

2.2.2 Size Distribution and Mean Diameter $<d_{\mathrm{FL17}}>$

In addition to the Fourier transform, a detailed analysis of the micro-domains was performed according to the procedure reported in Chapter 1.4.

The size distributions obtained for FL17 micro-domains in DOPC monolayers at molar fractions $\chi_{\mathrm{FL17}} = 5$, 10, 20 and 33 mol% are presented in Fig. 2.2.3(a). The histogram for each composition was obtained by averaging over a stack of fluorescence images. From the correspondent size distribution the mean diameter $<d_{\mathrm{FL17}}>_\chi$ for the micro-domains at a defined molar fraction was determined, presented in Fig. 2.2.3(b) as a function of χ_{FL17}.

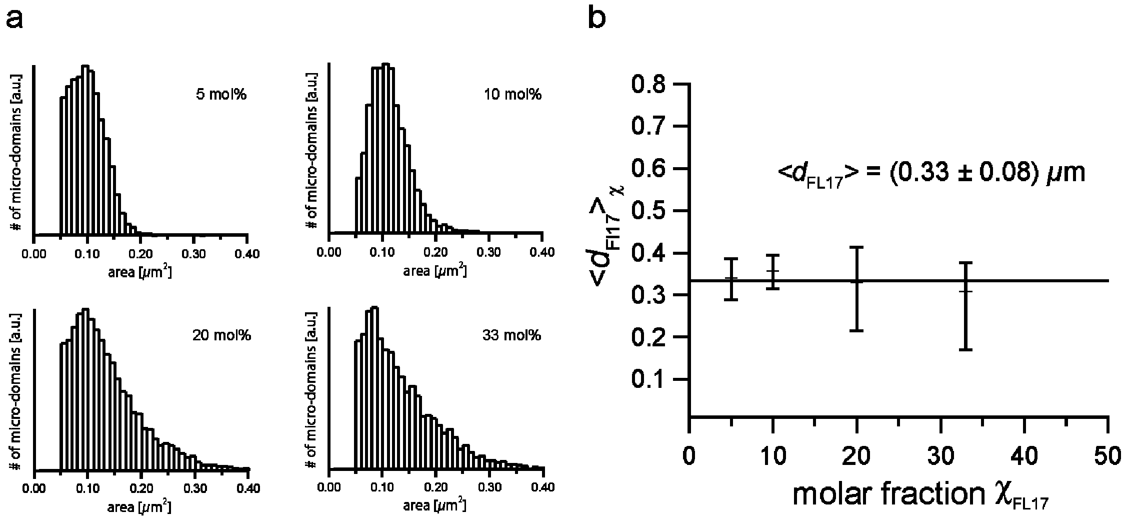

Fig. 2.2.3 (a) Size distribution of the micro-domains at the different molar fractions χ_{FL17}. (b) Mean domain diameter $<d_{\mathrm{FL17}}>_\chi$ as a function of χ_{FL17}. A mean diameter $<d_{\mathrm{FL17}}> = (0.33 \pm 0.08)$ μm could be determined for all monolayers incorporating FL17 micro-domains.

The linear fit in Fig. 2.2.3(b) indicates that FL17 micro-domains have almost constant size for all mixing ratios. Thus, a mean diameter $<d_{\mathrm{FL17}}> = (0.33 \pm 0.08)$ μm for all mixing ratios could be determined as average of all mean diameters $<d_{\mathrm{FL17}}>_\chi$. This value coincides well with the plateau obtained from the FFT (~0.4 μm) performed in Chapter 2.2.1.

2.3 X-Ray Measurements

Since the fluorescence microscopy technique is limited in the resolution of a few 100 nm, grazing-incidence X-ray diffraction (GIXD) measurements were carried out, to study the lateral, sub-micron structure of the monolayers as described in Chapter 1.5.

2.3.1 Analyzer crystal setup

Experiments were carried out at the air/water interface at several different locations of the sample to minimize artifacts from radiation damage or sample inhomogeneity. A molar fraction $\chi_{\mathrm{FL17}} = 50$ mol% was chosen to obtain sufficient diffraction intensities.

For experiments with FL17 molecules, a slightly modified setup including an analyzer crystal optics (depicted in Fig. 2.3.1(a)) was used instead of the more commonly used Soller collimator to resolve lateral structures larger than 0.1 μm. The analyzer crystal optics allowed to gain a higher angular resolution ($\Delta q_{xy} = 10^{-4}$ Å^{-1}) compared to the Soller collimator ($\Delta q_{xy} = 6 \cdot 10^{-3}$ Å^{-1}).

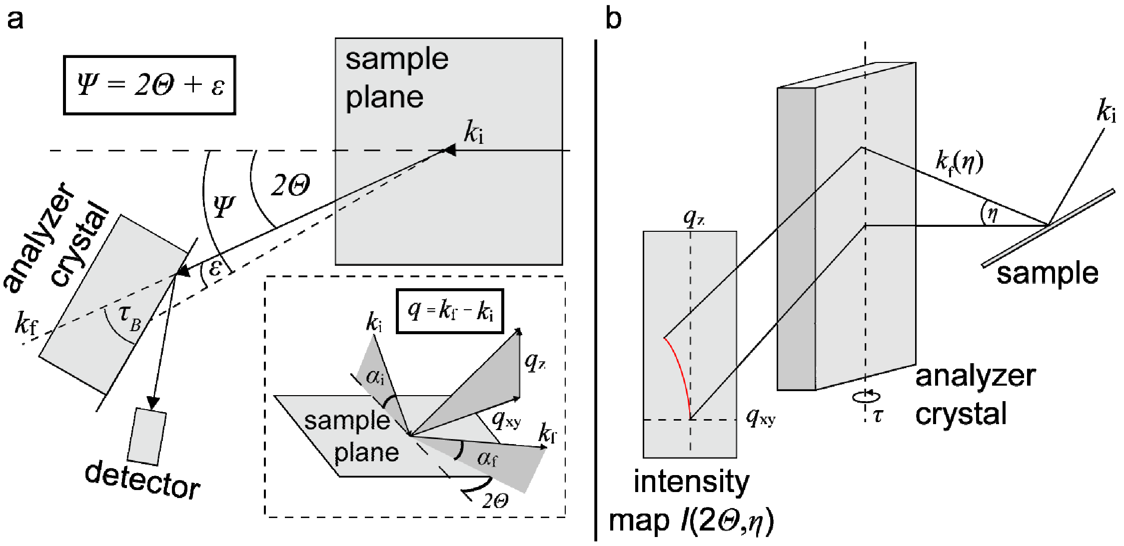

Fig. 2.3.1 (a) Sketch of the grazing-incidence X-ray diffraction (GIXD) setup, modified with an analyzer crystal optics (Si(111)). The scattering geometry is presented as an inset. (b) The impinging beam fulfils the Bragg condition at different at the analyzer crystal and appears therefore bended at the detector. The result is a curved diffraction (red line) at the detector.

As illustrated in Fig. 2.3.1(a) the analyzer crystal is lined up in the out-coming beam k_f, diffracted at the sample plane. The crystal can be rotated by an angle τ_B to set the Bragg condition for the incident beam. Only the fraction of the beam k_f that fulfills the Bragg condition is reflected at the crystal surface and hits the detector as indicated in Fig. 2.3.1(b).

This refines the diffracted beam to a signal with higher angular resolution, but cause also an immensely reduced intensity of the scattering signal, which is a notable disadvantage of this technique. Thus, in particular fluorinated lipids, which exhibit a huge scattering signal, turn out to be very attractive for this technique, since biological samples show basically weak intensities.

Since a linear point sensitive detector (PSD) was used for detection, the vertical component q_z of the scattered beam has to be taken into account. For an offset angle η for k_f the Bragg condition is fulfilled at an slightly detuned angle of the analyzer crystal. The Bragg angle for the used Si(111) analyzer crystal was determined by the preliminary calibration measurements for the X-ray wavelength of $\lambda = 1.54$ Å to be $\tau_B = 14.35°$.

According to Smilgies [Smilgies, 2003], the detuning of the Bragg angle can be approximated by

$$\Delta\tau = -\tan(\tau_B)\cdot\frac{\eta^2}{2}. \qquad (2.1)$$

This equation can be approximated from the exact deviation relation $\sin(\tau(\eta)) = \sin(\tau_B)\cos(\eta)$ by a Taylor expansion of $\sin(\tau)$ at $\tau = \tau_B$ and of $\cos(\eta)$ to second order. From this, one can see that the detuning increases therefore quadratic with the offset angle η.

For the measurement of the diffracted intensities with respect to q_{xy} the linear detector-analyzer crystal setup was moved as a fixed unit, replacing a simple detector. The detuning of the Bragg angle for the vertical component q_z at an offset angle η was therefore not corrected for each q_{xy}. Thus, the collected intensities appear to the detector setup as if the beam would have a small in-plane deviation $\varepsilon(\eta)$, as illustrated in Fig. 2.3.1(a).

The image distortion for small offset angles $\eta < 5°$ is given by the equation

$$\varepsilon(\eta) = -\tan(\tau_B)\cdot\frac{\eta^2}{2}. \qquad (2.2)$$

To obtain the recalculated intensity map the true scattering angle ψ can be determined by the equation

$$\Psi = 2\Theta + \varepsilon(\eta). \tag{2.3}$$

The measured intensity maps $I(2\Theta,\eta)$ has therefore to be corrected according to Equation (2.3).

Fig. 2.3.2(a) shows a measured, detuned reciprocal space map for the fluorinated compound FL17, where the distortion function $\varepsilon\ (\eta)$ is indicated by a red line. The intensity, integrated along q_z is presented in the graph below (see Fig. 2.3.2 (b)) and shows a broad peak with a smeared edge to larger q_{xy}.

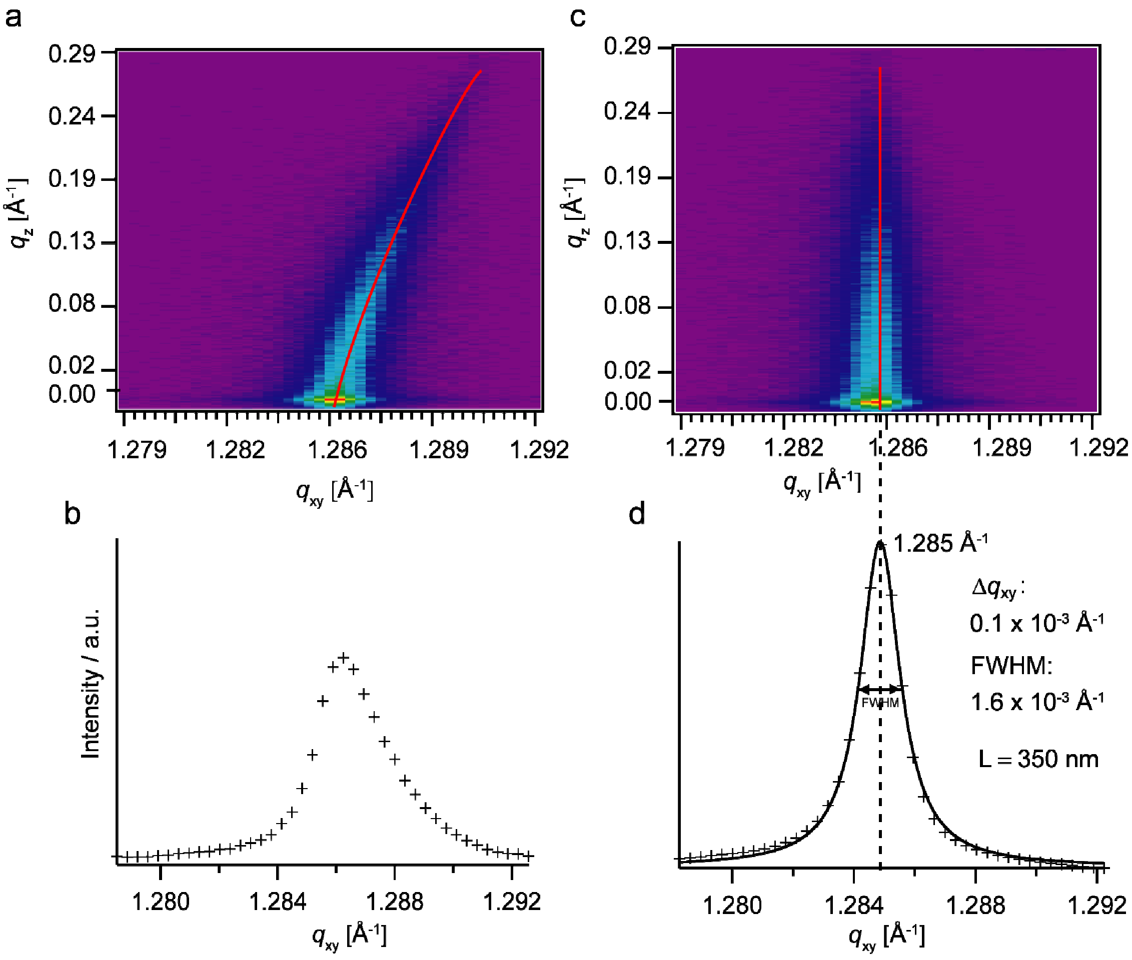

Fig. 2.3.2 (a) The measured reciprocal space map (a) and its reconstructed counterpart (c). The red line represents the bending function $\varepsilon\ (\eta)$ in respect to the deviation in q_z. The intensity integrated along q_z is presented in the lower row for both space maps (b + d). The corrected intensity plot shows a full width at half maximum (FWHM) of 1.6 x 10^{-3} Å^{-1} assigned to scattering length of $L = (0.35 \pm 0.01)\ \mu$m of the scattering signals, as calculated by the Scherrer equation.

The reciprocal space map reconstructed according to Equation (2.3) is presented in Fig. 2.3.2 (c). The intensity map was integrated along q_z, and shows a sharp peak at q_{xy} = 1.285 $Å^{-1}$ see Fig. 2.3.2 (d), denoting that the fluorocarbon chains take an upright orientation in a hexagonal arrangement.

Out of the peak position, a correlation length of 4.89 Å could be calculated by Equation (1.10). With the assumption of a hexagonal lattice the corresponding distance between fluorocarbon chains was calculated be d_{FL17}^{mo} = (5.65 ± 0.01) Å. This value agrees well with the value reported from the crystallography of ordered fluorocarbon chains [Bunn & Howell, 1954].

2.3.2 Crystal Size – The Scherrer Equation

As already mentioned, an advantage of the analyzer crystal optics is the higher angular resolution. This effect is extremely useful for the determination of the lateral dimensions of single diffracting crystals, i.e. here, the diameter of diffracting domains. The diffracted intensity peak width becomes broader, as the crystal size decrease [Guinier, 1963]. Therefore the dimension of a scattering object can be recalculated from this width.

This provides an experimental method to determine the size of submicroscopic crystals for which the mean diameter of a single crystal has to be at least in the order of 0.1μm.

According to Guinier the angular width of the diffracted intensity peak $\Delta(2\theta)$ can be determined for a scattering crystal by the so called Scherrer equation,

$$\Delta(2\Theta) = (0.9\lambda)/(L\cos\Theta_0), \qquad (2.4)$$

where a size $L=Nd$ is defined by the number N of scattering planes in the 2D crystal and their spacing d.

By a transcription from the angular to the width in the reciprocal space via the relation $\Delta(q_{xy}) = (2\pi/\lambda)\cos(\Theta_B)\Delta(2\Theta)$, Equation (2.4) can be written as

$$L = 0.9(2\pi)/\Delta(q_{xy}). \qquad (2.5)$$

The width of the intensity peak $\Delta(q_{xy})$ in reciprocal space can be identified as the Full Width at Half Maximum (FWHM) of the measured integrated intensity as can be seen in Fig. 2.3.2(d). In order to improve the accuracy of the calculated results the peak width has to be corrected by the instrumental resolution Δq_{xy}.

Finally Equation (2.5) can be written as

$$L = 0.9(2\pi)\Big/\sqrt{FWHM^2 - \Delta q_{xy}{}^2}\ . \tag{2.6}$$

For the fluorinated compound FL17 a width of the intensity peak $FWHM = (1.6 \pm 0.1) \times 10^{-3}$ Å^{-1} was determined leading by Equation (2.6) to a scattering length, i.e. the average size of a crystallite, of $L = (0.35 \pm 0.01)$ μm. The obtained value agrees well with the plateau obtained from the FFT (~0.4 μm, see Fig. 2.2.2(b)) and therefore also with the mean diameter calculation ($\langle d_{\mathrm{FL17}} \rangle = (0.33 \pm 0.08)$ μm, see Fig. 2.2.3(b)).

This result is remarkable, since it implies that each FL17 domain consists of only one single crystallite. In fact, this is one of the first demonstrations that utilize the analyzer crystal optics in combination with an in-plane X-ray scattering technique to resolve sub-micrometer organic crystallites in two-dimensions. This achievement was possible, owing to the very high in-plane ordering and high electron density of fluorocarbon chains.

2.4 Nearest Neighbor Distribution Function *p*(*r*)

Since self-assembled FL17 micro-domains have an identical, well defined size at various molar fractions (χ_{FL17} = 5 – 33 mol%), it is straightforward to describe them as two-dimensional colloidal particles. To quantify their lateral correlation within the mixed monolayers, the distance distribution for the nearest neighbors (distance between the centres of mass defined by image processing) *r* was extracted for more than 2000 domains in monolayers at various molar fractions χ_{FL17}.

The distance distribution function *p*(*r*) plotted versus *r/L* is presented in Fig. 2.4.1, where *r* is normalized with the domain size *L* = (0.35 ± 0.01) μm, obtained from the GIXD measurements.

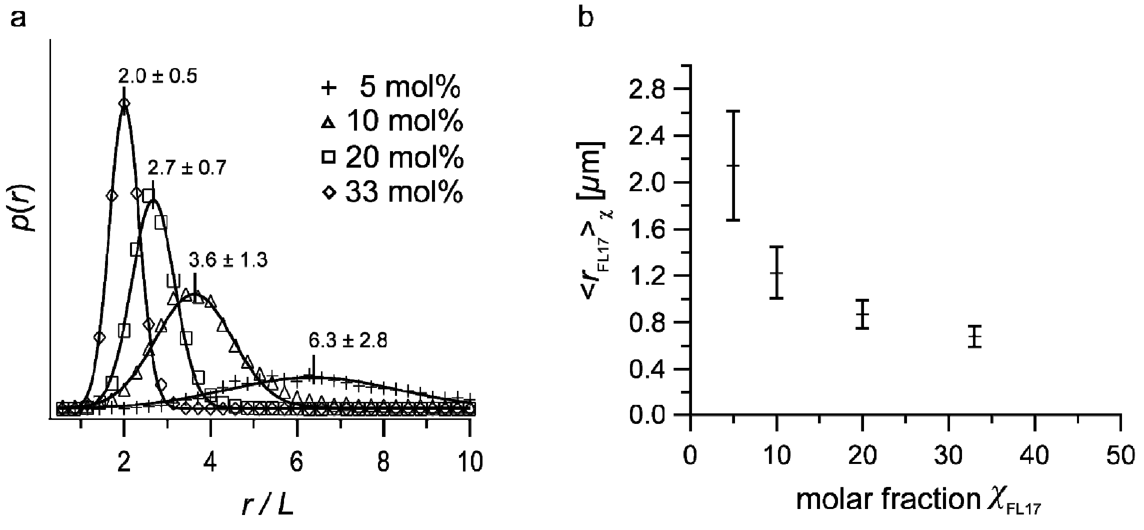

Fig. 2.4.1 (a) The nearest neighbor distribution function *p*(*r*) extracted from the center-to-center distance of the nearest neighbor micro-domains vs. the normalized distance, where *L* is the crystal diameter obtained by GIXD measurements. (b) The mean micro-domain distance $<r_{\mathrm{FL17}}>_\chi$ vs. the molar fraction χ_{FL17}.

In this plot, the peak position of a Gaussian fit (black line) corresponds to the mean inter-domain distance $<r_{\mathrm{FL17}}>_\chi$ at each molar fraction. As can be seen for the monolayer with a molar fraction of 33 mol%, *p*(*r*) has a very sharp peak at $<r_{\mathrm{FL17}}>_{33\ \mathrm{mol\%}}/L$ = (2.0 ± 0.5). This finding suggests that each domain is confined at a finite distance from the neighbors but does not merge with others to minimize the boundary length to the hydrocarbon surrounding, in contrast to other commonly used domain forming systems, like lipid/cholesterol mixtures [Mukerjee & Maxfield, 2004].

Results for mixed monolayer with smaller molar fraction for FL17 show a systematic shift in the peak position to larger mean nearest neighbor distances from $<r_{\mathrm{FL17}}>_{20\ \mathrm{mol\%}}/L = (2.7 \pm 0.7)$ to $<r_{\mathrm{FL17}}>_{10\ \mathrm{mol\%}}/L = (3.6 \pm 1.3)$, and $<r_{\mathrm{FL17}}>_{5\ \mathrm{mol\%}}/L = (6.3 \pm 2.8)$, accompanied by an increase in peak width. Nevertheless it is notable that a distinct peak can be found even for the monolayer with $\chi_{\mathrm{FL17}} = 5$ mol% of FL17, where micro-domains are still correlated even if the center-to-center distance is 6 times larger than the domain size. This suggests the presence of an effective repulsive interaction between the fluorinated micro-domains.

2.5 Radial Distribution Function *g*(*r*)

As the consequence of the presence of a repulsive interaction potential among the domains, resolved from Chapter 2.4, the long-range correlations between micro-domains of self-assembled fluorinated molecules can be treated as an analogue of two-dimensional colloidal crystallization of like-charged colloidal particles [Quesada-Pérez et al., 2002]. In a system of charged particles, an additional contribution to the pair interaction between the neighboring particles has to be taken into account beyond a critical particle density ρ_c, which is dependent from particle charge and matrix screening.

In order to quantitatively evaluate the multiple micro-domain correlations, the radial distribution function *g*(*r*) of >2000 domains was determined according to the procedure presented in Chapter 1.4.2. In Fig. 2.5.1 *g*(*r*) is presented versus the normalized distance *r/L* for varying molar fractions.

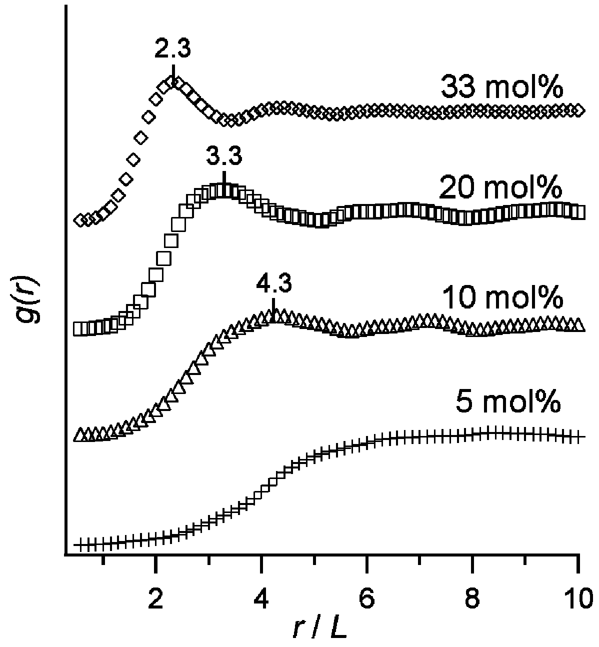

Fig. 2.5.1 The radial distribution function *g*(r) calculated from the absolute center distances between each micro-domain in the corresponding frame.

The first maximum in the radial distribution function represents the mean distance to the next neighbors of a particle. For *g*(*r*) all existing pair correlations in the region of interest are taken into account, which is in contrast to *p*(*r*), that merely considers correlations between the nearest neighbors.

Mean next neighbor distances for various molar fraction were determined to $<r>_{33\ \mathrm{mol\%}}/L = (2.3 \pm 0.2)$, $<r>_{20\ \mathrm{mol\%}}/L = (3.3 \pm 0.5)$, and $<r>_{10\ \mathrm{mol\%}}/L = (4.3 \pm 0.8)$. Note that the broad peak at $\chi_{\mathrm{FL17}} = 5$ mol% seen in Fig. 2.4.1(left) cannot be identified any longer in this plot, although the first order peaks of the other compositions in Fig. 2.5.1 agree well to the peak positions of their correspondent $p(r)$. This and a slight shift to greater values for all compositions in contrast to the mean nearest neighbor distances was observed, owing to the contribution of all micro-domain distances to the determination of the mean next neighbor distance.

Furthermore the radial distribution function points, on one hand, the existence of correlations that reach much further than the nearest neighbor distances described by $p(r)$. On the other hand the presence of second and third order maxima at high molar fractions implies a quasi hexagonal ordering for the micro-domains in the phospholipids matrix. With decreasing molar fraction the ordering is progressively lost.

2.6 Micro-Domain Interaction Potential –*ßw*(*r*)

Using the inverse work theorem [Hansen, 2007], $g(r)$ was related to the so-called potential of mean force $-\beta w(r)$, where $\beta = 1/k_BT$. As one can see from Equation 1.6, this potential is of free energy nature and includes multi particle interactions. In fact $w(r)$ is equal to the direct pair potentials between two particles only for infinitely diluted system [Belloni, 2000].

As shown in Fig. 2.6.1, the position and width of the first order minimum increases with the decrease in the molar fraction χ_{FL17}, while both, first and second order potential minima can be identified at $\chi_{FL17} \geq 10$ mol%.

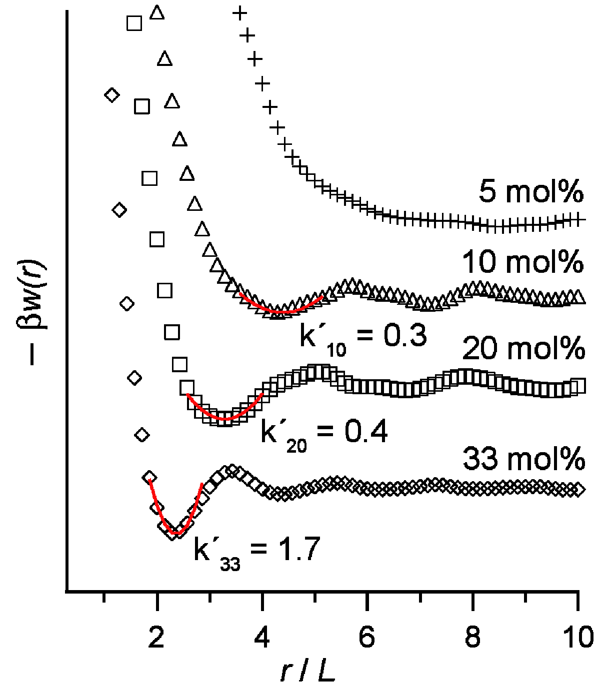

Fig. 2.6.1 The potential of mean force –*ßw*(r) vs. the normalized distance r/L calculated from the radial distribution function *g*(r) by the inverse work theorem. From a harmonic fit (red fit) of the first potential minimum, spring constants *k*' could be derived.

Spring constants *k*' could be calculated by assuming a harmonic potential at the first minimum of $-\beta w(r)$ to $k'_{33mol\%} = 1.7$, $k'_{20mol\%} = 0.4$ and $k'_{10mol\%} = 0.3$. The decrease in *k*' represents the weaker interaction potential at lower molar fractions.

The mixed monolayer at $\chi_{FL17} = 5$ mol% shows only negligible long range interactions, since no fit could be performed. For this mixing ratio the potential can be seen as representative for an effective pair-correlation potential $u^{eff}(r)$ of fluorinated micro-domains and screening matrix.

According to the Derjaguin-Landau-Verwey-Overbeek (DLVO) theory for colloids in charge stabilized suspensions the effective interaction is given by a Yukawa potential $-ßw_{\mathrm{Yuk}}(r)$ [Verwey & Overbeck, 1948; Evans & Wennerström, 1994] in terms of

$$-ßw(x)_{yuk} = A * \exp(-\kappa * x)/x, \tag{2.1}$$

where x is the normalized distance r/L, A is an initial potential and κ the characteristic screening length in the system. Here, the stabilization is mainly modulated by the surrounding lipid matrix.

For visualization purposes the potentials were multiplied by the normalized radius r/L. In the case of the Yukawa potential this results in a linear graph. In Fig. 2.6.2 the potentials extracted from Fig. 2.6.1 are shown together with a fitted Yukawa potential (solid line).

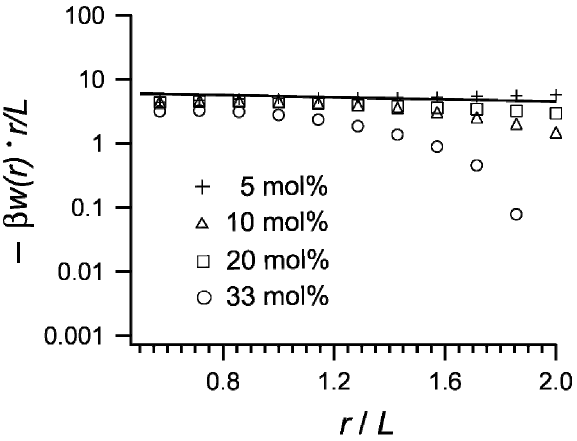

Fig. 2.6.2 $-ßw(r)(r/L)$ vs. the normalized radius for the potentials of FL17 micro-domains at various molar fractions. The solid line represents a fitted Yukawa potential, forming a straight line. Only micro-domains at a molar fraction of 5 mol% fulfill this condition.

Only in the case of micro-domains in mixed monolayers at a molar fraction of 5 mol% the arrangement fulfills the conditions of a Yukawa potential, representing the case of statistical arrangement mainly independent from multi particle interactions.

3 Influence of Molecular Structure on the Micro-/Nano-Domains of Fluorinated Lipids: Fine-tuning of Domain Size and Distribution

3.1 Introduction

This chapter describes the fine-tuning of domain size and distribution by distinct changes in molecular chemistry. Here, the influence of chain length, numbers of chains and head group functions were systematically investigated at different molar fractions following the methods described in Chapter2.

Different fluorinated molecules with different chain lengths (FL10, FL13 and FL17), numbers of chains (FL10 and FT10) and head group (FL10 and FL10man) were incorporated in a phospholipid matrix (DOPC) at various molar fractions χ and spread to the air/water interface of a Langmuir film-balance for further analysis.

Image processing of Langmuir-Schaeffer (LS) transferred monolayers was performed to determine the mean micro-domain diameter $<d>_\chi$, nearest neighbor distance $<r>_\chi$, radial distribution function $g(r)$ and potential of mean force $–ßw(r)$.

The modeling of the molecular pair interactions following the theory of the “equivalent dipole model” by McConnell allows the theoretical prediction of micro-domain size with assumptions on a molecular level. The experimental results of the X-ray analysis serve as background for the domain-size calculations while the image processing results verify the predicted domain-size.

3.2 Theory of Lipid Domain Formation

For a lipid monolayer consisting of two phases (i.e. "solid" domains in "liquid" matrix) at the air/water interface the final state of a single domain can be defined by the free-energy function *F*, according to the "equivalent dipole model" proposed by McConnell [McConnell, 1991],

$$F = F_{\lambda} + F_{el}, \tag{3.1}$$

where F_{el} represents the electrostatic energy and F_{λ} is the line tension energy.

The electrostatic energy of a domain can be written as a function of the domain radius *R* and the molecular dipole density difference between lipid domain and surrounding matrix Δm:

$$F_{el} = 2\pi R(\Delta m)^2 \ln\left(\frac{e^2\delta}{4R}\right), \tag{3.2}$$

where *e* is the Eulerian number and δ the nearest-neighbor intermolecular dipole-dipole distance. The free energy from line tension λ is given by

$$F_{\lambda} = 2\pi R\lambda . \tag{3.3}$$

The minimum free energy *F* of a single domain and the corresponding equilibrium radius $R = R_{eq}^{0}$ can therefore be given by,

$$R_{eq}^{0} = \left(\frac{e^3\delta}{4}\right)\cdot \exp\left(\frac{\lambda}{(\Delta m)^2}\right). \tag{3.4}$$

The first term in Equation (3.4) can be assumed as a constant at a given surface pressure Π_{c}, owing to the fact that the mean molecular area at a certain molecular fraction χ is almost constant and independent from the chain length. Thus a change in the equilibrium domain radius can only be influenced by the term $\lambda/(\Delta m)^2$, often called as a "material parameter"

Measurements of Molecular Dipole Moment Difference Δm

The effective molecular dipole moment μ of a lipid can be calculated considering three contributing factors [Brockman, 1994]: (a) The contribution from the polar head-group, (b) an influence of oriented water molecules adjacent to the dipolar head group and (c) the contribution from asymmetric chain termini. Previous accounts reported that the effective molecular dipole moment of fluorinated lipids is dominated by the CF_3 chain terminus [Vogel & Möbius, 1988; Schneider et al, 2005].

To determine the molecular dipole moment density *m*, surface potentials of pure monolayers at the air/water interface were measured as a function of molecular area A_{mo} with the KIBRON film-balance equipped with a Kelvin probe (see Chapter 1.2.3). The measured surface potential *V* can be given as a function of the dipole density *m* and thus of the molecular dipole moment μ following the Helmholtz equation (1.5).

Domain Line Tension λ

The line tension in a two-component mixture of dimyristoyl-phosphatidyl-choline (DMPC) and dihydrochloesterolchol (Dchol) was calculated in a recent account by Hu et al [Hu et al., 2006], taking the height mismatch Δl between fluid and solid phases into account,

$$\lambda = \gamma \Delta l \, , \tag{3.5}$$

where γ is the surface free energy of the hydrocarbon-air interface.

This theory of lipid domain formation was adapted to the here presented fluorcarbon-hydrocarbon mixtures. So that from the height mismatch between the surrounding phospholipid DOPC and the fluorinated molecule the line tension can be written as

$$\lambda = \Delta\gamma \times l_{FL} + \gamma \times \Delta l \tag{3.6}$$

where $\Delta\gamma$ is the difference in the surface free energy between hydrocarbon chains and fluorocarbon chains, and γ the surface free energy at the chain-air interface.

The formation of fluorinated micro-domains is therefore considered to be mainly influenced by the interaction between the fluorocarbon and hydrocarbon chains and an additional contribution generated by a height mismatch between the boundary phospholipid and the fluorinated molecule.

3.3 Fluorinated Molecule/DOPC Monolayer at the Air/Water Interface

To demonstrate that a LS-transfer process of a mixed monolayer from the air/water interface to a hydrophobic glass surface does not seriously influence the shape and arrangement of micro-domains in the monolayer, fluorescence images of mixed monolayers at the air/water interface for FL10 micro-domains were made using the KSV Langmuir trough equipped with a glass window. This setup, presented in Fig. 1.3(b) allow for the use on an inverted fluorescence microscope.

Fig. 3.3.1(left) shows an image of a mixed monolayer with a molar fraction of 33 mol% FL10, floating on the subphase.

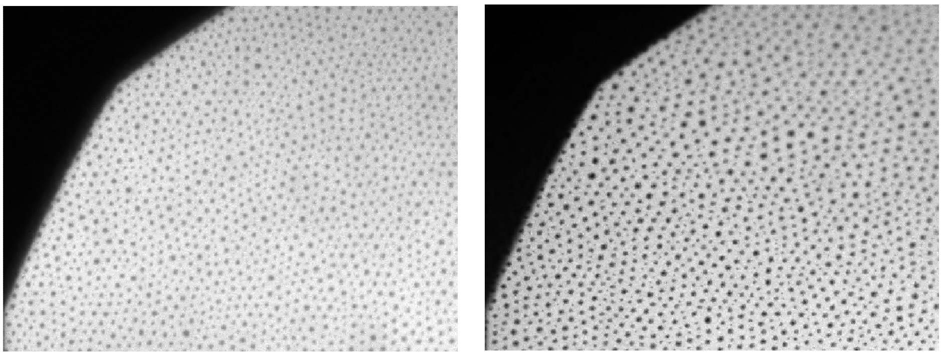

Fig. 3.3.1 Fluorescence image of a mixed monolayer incorporating FL10 micro-domains (left) spread onto the subphase and compressed to $\Pi = 15\ \mathrm{mNm^{-1}}$ and (right) LS transferred to a glass substrate. The formed self-assemblies were detectable in both monolayers, but LS-transferred monolayers exhibit an improved contrast.

In this image FL10 micro-domains were identifiable but weak in contrast, owing to their strong diffusion within the monolayer during the observation. After the transfer of the monolayer by the LS-technique at a defined transfer pressure Π_T, the surface supported monolayer, depicted in Fig. 3.3.1 (right) was in a comparable shape, but exhibited an improved contrast.

At the same time this verified that the de-mixing process was not induced nor influenced by the transfer. To obtain a better accessibility and improved contrast the following optical investigations were done on transferred monolayers mounted in a fluid cell, as described in Chapter 1.2.4. In the following the surface pressure mentioned corresponds to the transfer pressure Π_T at the moment of the LS deposition.

3.4 Influence of Chain Length

To prove that the line tension λ is the dominating contribution in the determination of the micro-domain equilibrium diameter, as discussed theoretically in Chapter 3.2 fluorinated molecules FLn with a variation in the molecular height h_{mo} have been synthesized. The molecules consist all of two fluorinated chains with 9, 12 or 16 CF_2 chain units plus one CF_3 terminus per chain for the molecules FL10, FL13 and FL17 respectively.

Mixed monolayers incorporating the synthesized fluorinated molecules with different chain lengths at the molar fractions χ_{FLn} = 33, 20, 10 and 5 mol% were transferred onto hydrophobic glass samples and subsequently image processing was performed, as described in Chapter 1.4.1.

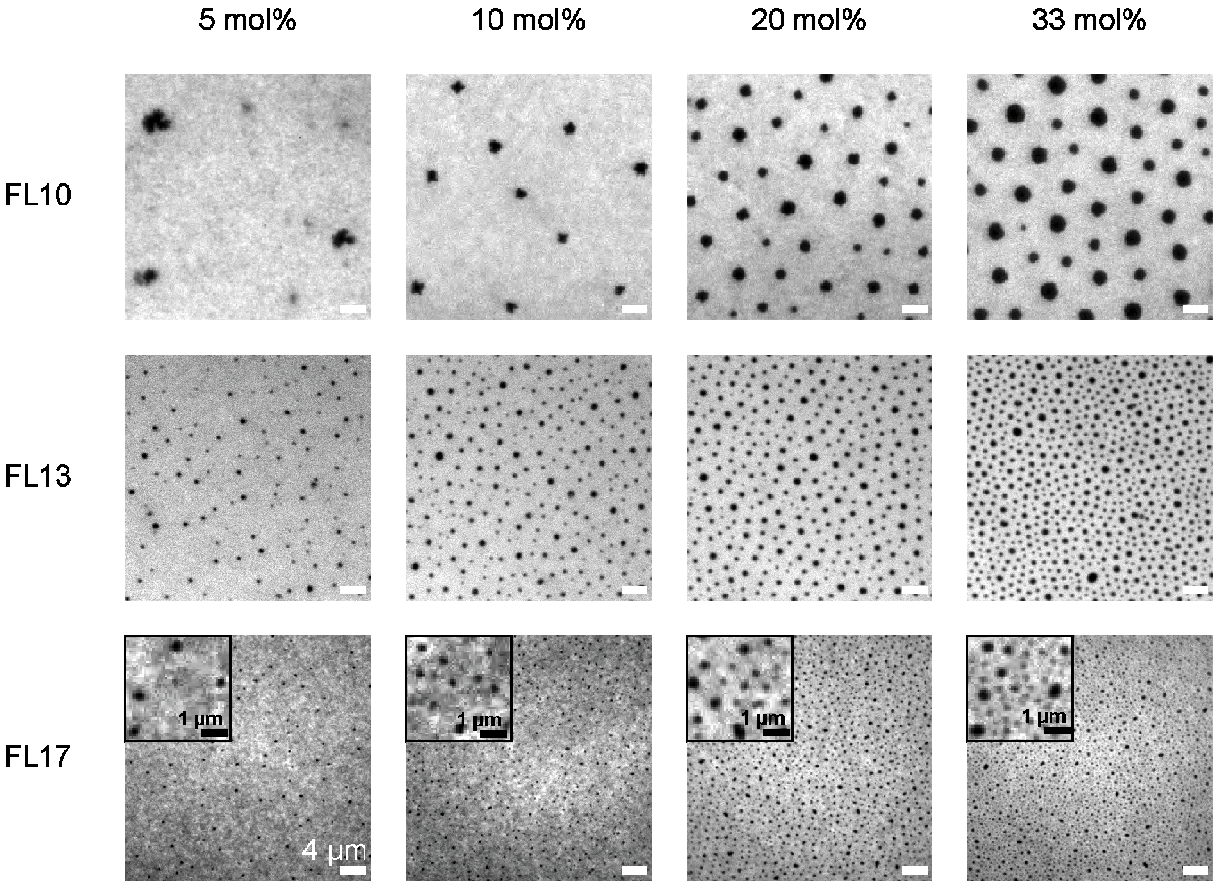

Fig. 3.4.1 Fluorescence images of FL10 (upper row), FL13 (middle row) and FL17 (lower row) demonstrate the de-mixing and self assembling of fluorinated molecules into circular micro-domains at various molar fractions χ_{FLn}. With an ascending amount of micro-domains, their arrangement gets more structured, due to a short range repulsive momentum.

The upper row in Fig. 3.4.1 presents LS transferred monolayers of FL10 in DOPC transferred at Π = 15 mNm^{-1} , while in the middle and last row monolayers of FL13, and respectively FL17 are illustrated transferred at Π = 25 mNm^{-1}. The molar fraction χ_{FLn} of fluorinated molecules is ascending from left to right. All compounds, except of FL10 below χ_{FL10} = 10 mol%, show a de-mixing and self-assemble into micro-domains with circular shape for highest as well as for lowest doping ratios of fluorinated molecules.

3.4.1 Instabilities of FL10 Micro-Domains

Instability in molar fraction

FL10 molecules self-assemble into micro-domains with circular shape at high molar fractions, but form different equilibrium shape, if a critical threshold value for the molar fractions <10 mol% is under-run.

For monolayers with χ_{FL10} = 10 mol% the micro-domains begin to take a star-like shape (Fig. 3.4.2(left) while for monolayers <10 mol% further so-called harmonic shapes could be observed (Fig. 3.4.2(right)).

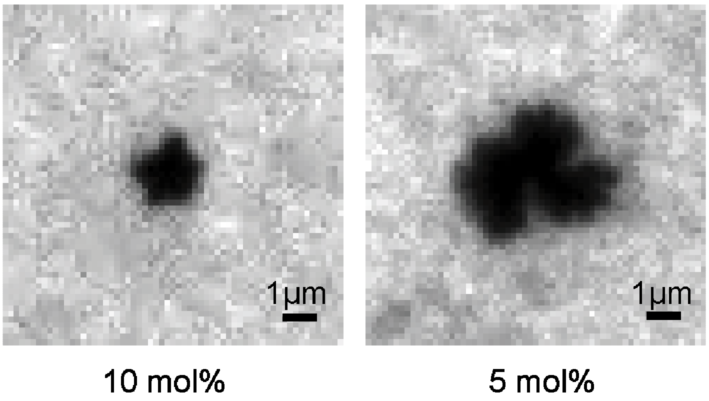

Fig. 3.4.2 The harmonic shapes of a FL10 micro-domain in a transferred monolayer at a molar fraction of χ_{FL10} = 10 mol% (left) and χ_{FL10} = 5 mol% (right)

More details can be found in Appendix A.5.1.

Compression Instability

Another regime of instability in domain shape for FL10 micro-domains was observed by the compression of mixed monolayers with high domain density ($\chi_{\mathrm{FL10}} > 10$ mol%) to surface pressures $\Pi > 17$ mNm^{-1}.

A LS-transferred mixed monolayer of FL10 with a molar fraction of $\chi_{\mathrm{FL10}} = 33$ mol% is presented in Fig. 3.4.3 at different surface pressures.

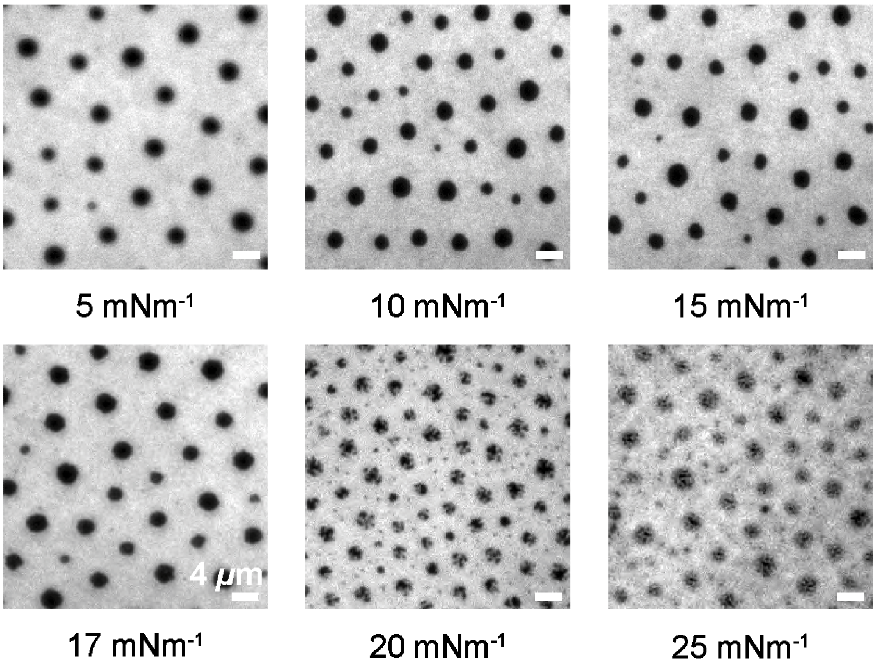

Fig. 3.4.3 Monolayers of FL10 in DOPC at a molar fraction of $\chi_{FL10} = 33$ mol% transferred at different surface pressures.

At surface pressures of $\Pi < 17$ mNm^{-1} FL10 micro-domains exhibit a circular shape, but with further compression of the monolayer the micro-domains undergo a transition, first into a jagged shape and finally begin to break down, owing to the stronger sensitivity of FL10 for fluctuations in the molecular dipole moment (see Appendix A.5 for more details).

3.4.2 Mean Micro-Domain Diameter $<d_{\mathrm{FLn}}>$ and Nearest Neighbor Distance $<r_{\mathrm{FLn}}>$

As shown already in Fig. 3.4.1, FL10, FL13 and FL17 micro-domains exhibit in most cases a circular shape wherefore a mean diameter $<d_{\mathrm{FLn}}>_{\chi}$, at a distinct molar fraction

χ_{FLn} can be estimated by a circular fit. A domain center could also be defined, wherefrom the mean next neighbor distance $<r_{\mathrm{FLn}}>_\chi$ was calculated.

The peak position of Gaussian fits of size- and distance-distributions determines $<d_{\mathrm{FLn}}>_\chi$, shown in Fig. 3.4.4(left) and $<r_{\mathrm{FLn}}>_\chi$, shown in Fig. 3.4.4(right) for the molar fractions χ_{FLn} = 33, 20 and 10 mol% for FL10, FL13 and FL17 and additional χ_{FLn} = 5 mol% for FL13 and FL17 (see Appendix A.4 for the size histogram and next neighbor histogram of the monolayers at corresponding molar fraction).

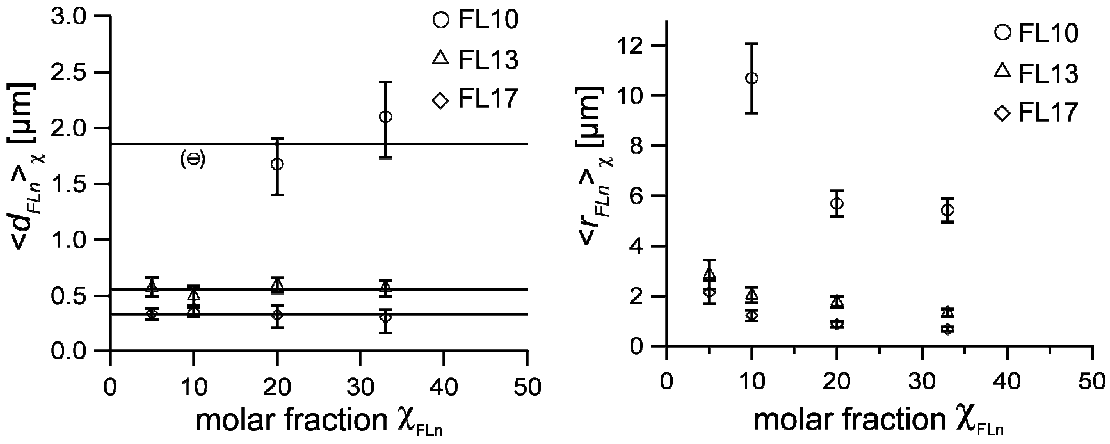

Fig. 3.4.4 (left) The mean diameter of micro-domains $<d_{\mathrm{FLn}}>_\chi$ vs. the molar fraction χ_{FLn} of fluorinated molecules in a DOPC matrix. For FL17 and FL13 the mean diameter of micro-domains remains constant, even for low molar fractions. Micro-domains of FL10 change their shape below 10 mol% (see Fig. 3.4.2), thus no mean diameter could be calculated. (right) The mean nearest neighbor distance $<r_{\mathrm{FLn}}>_\chi$ vs. χ_{FLn} for FL10, FL13 and FL17, even at high molar fractions. Note that a minimum distance between domains remains constant.

As FL10 micro-domains take no round shape for a molar fraction <10 mol%, no qualitatively sufficient circular fit could be performed. The presented diameter for $<d_{\mathrm{FL10}}>_{10\mathrm{mol\%}}$ is only a rough estimation and therefore not taken into account for the calculation of a mean diameter.

However the remaining calculated mean diameters $<d_{\mathrm{FLn}}>_\chi$, for a molecule at varying molar fractions remain constant as indicated by the linear fits for all molecules. Thus a mean diameter $<d_{\mathrm{FLn}}>$ for the fluorinated compounds could be determined as the mean value to $<d_{\mathrm{FL10}}>$ = (1.88 ± 0.29) μm and $<d_{\mathrm{FL13}}>$ = (0.56 ± 0.07) μm and $<d_{\mathrm{FL17}}>$ = (0.33 ± 0.08) μm respectively.

The mean micro-domain diameters $<d_{\mathrm{FLn}}>$ for FL10, FL13 and FL17 exhibit a clear dependency on the chain length of fluorinated molecules: With increasing chain length the mean micro-domain diameters $<d_{\mathrm{FLn}}>$ become smaller. Since the line tension λ_{FLn} is the dominating parameter in tuning the mean micro-domain diameter (see Chapter 3.2), the elongation of chain length leads to a decrease in λ_{FLn} and therefore to smaller domains.

The mean center to center distances $<r_{\mathrm{FLn}}>_{\chi}$, for neighboring micro-domains exhibit a clear repulsive interaction between the micro-domains. An increase in the distance for a decreasing molar fraction and therefore a reduced number of micro-domains could be observed.

3.4.3 Radial Distribution Function $g_{\mathrm{FLn}}(r)$ and Potential of Mean Force $-ßw_{\mathrm{FLn}}(r)$

To obtain information about the micro-domain correlations in the presence of a phospholipids environment the radial distribution function $g_{\mathrm{FLn}}(r)$ was determined according to the procedure presented in Chapter 1.4.2.

For the fluorinated compounds FL10, FL13 and FL17, $g_{\mathrm{FLn}}(r)$ is presented in Fig. 3.4.5(left) for mixed monolayers with a molar fraction of $\chi_{\mathrm{FLn}} = 33$ mol%.

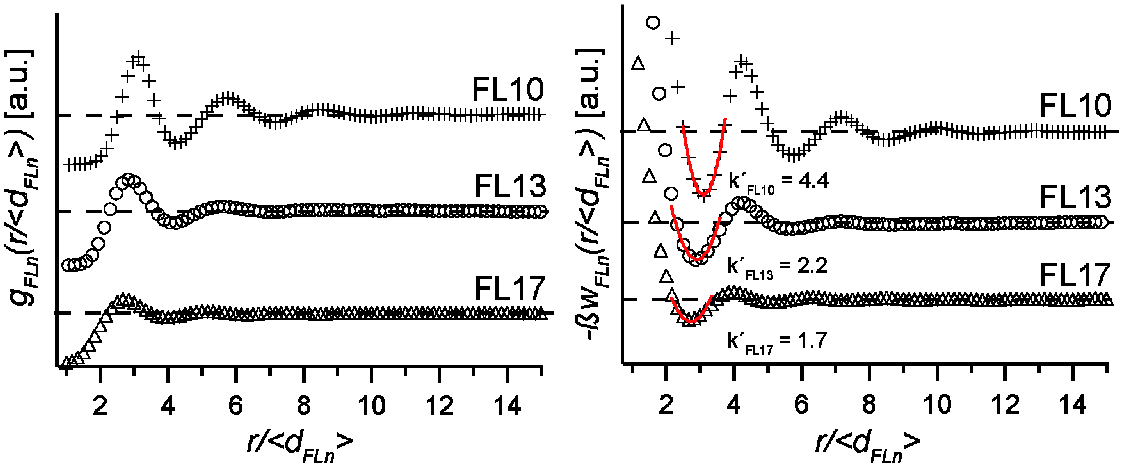

Fig. 3.4.5 The radial distribution function g(r) (left) and potential of mean force $-ßw(r)$ (right) vs. the normalized distance r/d for micro-domains of fluorinated molecules FL10, FL13 and FL17 at the molar fraction of $\chi_{FLn} = 33$ mol%

The radial distribution function is normalized with the distance r/d where d is the corresponding micro-domain mean diameter $<d_{\mathrm{FLn}}>$ calculated in the foregoing Chapter 3.4.2.

An oscillating structure in $g_{\mathrm{FLn}}(r)$, implying a "quasi hexagonal" arrangement of micro-domains within the phospholipids matrix could be observed for all molecules. FL10 micro-domains show the strongest oscillation up to the third order while for FL13 and FL17 only the first order peak is outstanding. This suggests the presence of the strongest repulsive interaction for the micro-domains formed by FL10. The interaction between micro-domains becomes weaker with a decrease in the micro-domain size. For smaller domains the diffusion within the mixed monolayer becomes stronger.

The potential, forming this "quasi hexagonal" structure can be visualized by the potential of mean force (PMF) $-ßw_{\mathrm{FLn}}(r)$ the effective interaction potential between the micro-domains. The potential of mean force was calculated using the inverse work theorem, as presented in Chapter 1.4.3 and is shown for the fluorinated compounds FL10, FL13 and FL17 at a molar fraction of 33 mol% in Fig 3.4.5(right), versus the normalized distance r/d.

Like the radial distribution function the potential of mean force exhibits an oscillating structure, while the first minimum $<r_{\mathrm{FL10}}>_{\mathrm{PMF}}$ corresponds the mean distance of the nearest neighbor distribution $<r_{\mathrm{FLn}}>$ in Chapter 3.4.2, except for a small shift to bigger distances. Note that this shift is owing to the contribution of all neighboring micro-domains, in contrast to only the nearest neighbor. The first minima position for FL10 micro-domains is $<r_{\mathrm{FL10}}>_{\mathrm{PMF}} = (6.9 \pm 0.9)\ \mu\mathrm{m}$ in contrast to the nearest-neighbor distance $<r_{\mathrm{FL10}}> = (5.4 \pm 0.9)\ \mu\mathrm{m}$, obtained in Chapter 3.4.2. For FL13 and FL17 the values $<r_{\mathrm{FL13}}>_{\mathrm{PMF}} = (1.7 \pm 0.5)\ \mu\mathrm{m}$, $<r_{\mathrm{FL13}}> = (1.3 \pm 0.3)\ \mu\mathrm{m}$ and $<r_{\mathrm{FL17}}>_{\mathrm{PMF}} = (0.8 \pm 0.1)\ \mu\mathrm{m}$, $<r_{\mathrm{FL17}}> = (0.7 \pm 0.2)\ \mu\mathrm{m}$ respectively were obtained.

The approximation of the first potential minimum by a harmonic potential $v(r/<d_{\mathrm{FLn}}>)$ returns a spring constant k', representing the strength of an interaction between micro-domains. For FL10 the structure in the arrangement between the micro-domains is with a spring constant of $k'_{\mathrm{FL10}} = (4.4 \pm 0.1)$ the strongest, while for the smaller domains of FL13 and finally FL17 the spring constant decreases to $k'_{\mathrm{FL13}} = (2.2 \pm 0.1)$ and $k'_{\mathrm{FL17}} = (1.7 \pm 0.1)$.

3.4.4 GIXD Measurements

To resolve an influence of the varying chain length to the substructure of fluorinated micro-domains, grazing-incidence X-ray diffraction measurements (GIXD) at the air/water interface have been performed. A Soller collimator setup was used for these experiments to yield sufficient diffraction intensities to resolve chain-chain correlations of the fluorinated molecules within the micro-domains.

Mixed monolayers incorporating FL10, FL13 and FL17 with a molar fraction of 50 mol% were spread at the air water interface of a Langmuir film balance, as described in chapter 1.5.1. The resulting intensity maps for the single monolayers at various surface pressures Π were integrated along q_z and plotted over q_{xy}. Integrated intensities for all measured surface pressures can be found in Appendix A.2.

Fig 3.4.6 shows the integrated diffraction intensity for each molecule in mixed monolayers at a surface pressure of $\Pi = 10$ mNm^{-1}.

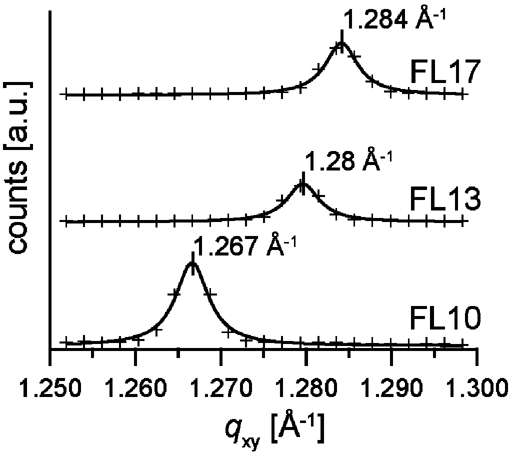

Fig. 3.4.6 GIXD measurements of mixed monolayers at a surface pressure of $\Pi = 10$mNm^{-1} with a molar fraction of $\chi_{FLn} = 50$ mol%. The fluorinated compounds take a upright orientation in a hexagonal packing, verified by a single symmetric peak in q_{xy}.

Since the measured intensities in respect to q_{xy} exhibit a single, symmetric peak for all fluorinated molecules, a hexagonal packing of upright oriented molecules with corresponding molecular distances of $d^{mo}_{FL10} = (5.73 \pm 0.01)$ Å, $d^{mo}_{FL13} = (5.67 \pm 0.01)$ Å and $d^{mo}_{FL17} = (5.65 \pm 0.01)$ Å can by assumed.

A slight decrease in the mean distance for longer fluorinated compounds can be observed, owing to the stronger chain-chain interaction of the longer chains for FL17 compared to FL10. A further compression of mixed monolayers incorporating FL10 micro-domains show a shift of the intermolecular chain-chain distance to smaller distances until the chain-chain correlation disappears at higher pressures (see Appendix A.2).

3.4.5 Surface Potential Measurements

The molecular dipole moment density *m* for pure monolayers of fluorinated molecules, and DOPC was determined from surface potential measurements as described in Chapter 1.2.3.

In Fig. 3.4.7(left) the Π-Area as well as the ΔV-area measurements are presented for FL10 and for the matrix DOPC in Fig. 3.4.7(right). Within this figures outstanding points are labeled corresponding to the transfer pressures Π_T = 15 mNm^{-1} for FL10 micro-domains and Π_T = 25 mNm^{-1} for the other monolayers.

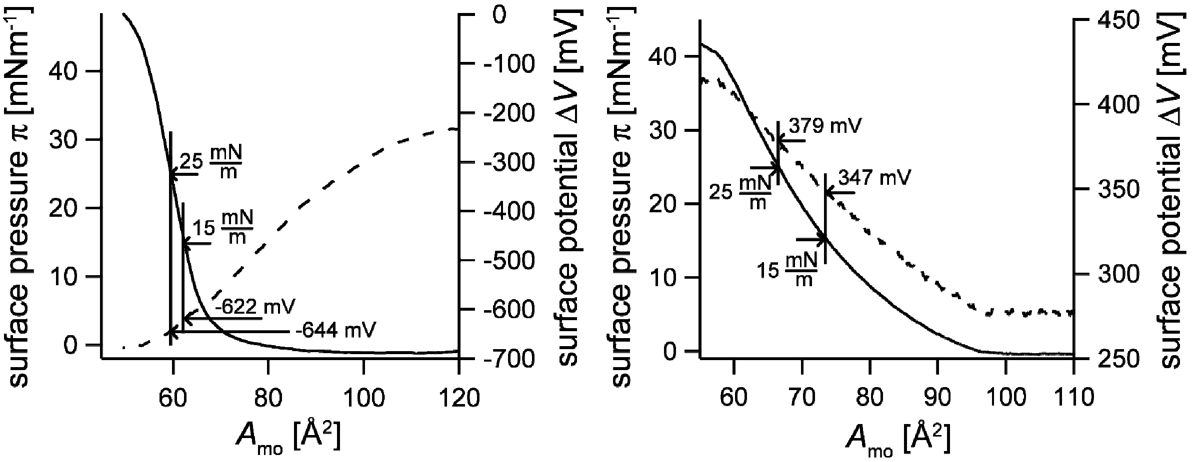

Fig. 3.4.7 Surface potential measurements of pure (left) FL10 and (right) DOPC monolayers. At the transfer pressures of π_T = 15 mNm^{-1} and π_T = 25 mNm^{-1} the surface potential is labeled. The corresponding dipole density is then calculated by the Helmholtz equation (Eq. 1.3).

For the surface potential ΔV the molecular dipole density *m* was calculated by the Helmholtz Equation (Equation (1.3)).

3.4.6 Comparison to *“Equivalent Dipole Model”*

Theoretical calculations for the micro-domain equilibrium diameter $<d>_{th}$ with respect to the chain length of the fluorinated molecules were done according to the "equivalent dipole model", discussed in Chapter 3.2. The required parameters in Equation (3.4) were determined, as described in the following:

Molecular dipole distance δ

A molecular chain-chain distance for DOPC $<r_{\mathrm{DOPC}}>_{\pi = 15\ \mathrm{mNm}^{-1}} = (6.51 \pm 0.01)$ Å and $<r_{\mathrm{DOPC}}>_{\pi = 25\ \mathrm{mNm}^{-1}} = (6.18 \pm 0.01)$ Å at the distinct transfer pressures was obtained from the Π-Area isotherm of the pure monolayer (see Fig. 3.4.7). The correspondent values for the fluorinated molecules were obtained from X-ray diffraction results, presented in Chapter 3.4.5.

From these a value for the molecular dipole distance $\delta = (<r_{\mathrm{DOPC}}>_{\pi} + <r_{\mathrm{FLn}}>_{\pi})\ /2 = (6.09 \pm 0.03)$ Å at the domain boundary could be calculated at a transfer pressure.

Molecular dipole density difference Δm

The molecular dipole density difference $\Delta m \varepsilon^{-1} = (275 \pm 2)$ mV at a transfer pressure of $15\mathrm{mNm}^{-1}$ and $\Delta m \varepsilon^{-1} = (265 \pm 2)$ mV at $\pi = 25\ \mathrm{mNm}^{-1}$ was determined from the corresponding surface potential measurements of pure monolayers, see Chapter 3.4.5.

Molecular height h^{mo}

To calculate the interaction length between the chains and the height mismatch, molecular length of the boundary molecules had to be determined. The height of the DOPC molecule in a fluid phase could be determined by X-ray scattering of lipid bilayers stacks to $h_{\mathrm{DOPC}} \approx (18.5 \pm 0.5)$ Å [Tristram-Nagle et al., 1998]. The heights of the fluorinated molecules were also determined by small angle x-ray scattering (SAXS) measurement to $h^{mo}_{FL10} = (12.8 \pm 0.5)$ Å, $h^{mo}_{FL13} = (16.8 \pm 0.5)$ Å and $h^{mo}_{FL17} = (21.9 \pm 0.5)$ Å (see data in the Appendix A.3).

Surface free energy γ

The surface free energies for a hydrocarbon-air and for a fluorocarbon-air interface have been reported to be $\gamma_{\mathrm{HC\text{-}air}} = 19.3\ \mathrm{mNm}^{-1}$ and $\gamma_{\mathrm{FC\text{-}air}} = 9.5\ \mathrm{mNm}^{-1}$ respectively [Chaudhury & Owen, 1993]. The surface free energy difference between the molecules was therefore calculated to $\Delta\gamma = 9.8\ \mathrm{mNm}^{-1}$.

The predicted micro-domain diameters $<d_{\mathrm{FLn}}>_{th}$ according to Equation (3.4) are presented in Fig. 3.4.8 and show a good agreement with the obtained values of the image processing.

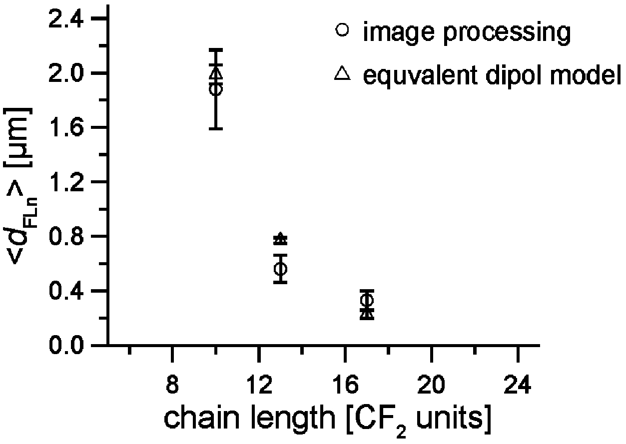

Fig. 3.4.8 The mean diameter $<d_{\mathrm{FLn}}>$ vs. the chain length of the fluorinated molecules in the unit of CF_2 segments. Theoretical determined values correspond well with the image processing results.

Equilibrium micro-domain diameters have been calculated to $<d_{\mathrm{FL10}}>_{th} = (1.99 \pm 0.4)$ μm, $<d_{\mathrm{FL13}}>_{th} = (0.77 \pm 0.14)$ μm and $<d_{\mathrm{FL17}}>_{th} = (0.23 \pm 0.03)$ μm, showing the tendency of a reduction of the micro-domain diameter for an increase in the chain length.

In contrast to these findings, Lipowsky and Dimova estimated in a more generally approach the line tension of a domain boundary in a two component system (A and B) from the energy difference ΔU between the domain lipids and the surrounding matrix lipids [Lipowsky & Dimova, 2003] to

$$\lambda \approx \frac{\Delta U}{l_{mo}}, \tag{3.7}$$

where l_{mo} is the lateral size of lipid molecules and ΔU is defined by

$$\Delta U \equiv \left[\tfrac{1}{2}\left(U_{A-A} + U_{B-B}\right) - U_{A-B}\right]. \tag{3.8}$$

$U_{\mathrm{A-A}}$ and $U_{\mathrm{B-B}}$ represent pair interactions between lipids of the same kind, $U_{\mathrm{A-B}}$ defines the pair interaction between the lipids at the domain boundary. Adapting this approach to the here present system the pair interaction within the alkyl matrix $U_{\mathrm{CH-CH}}$ can be assumed as constant over all experiments, since always DOPC was used as matrix phospholipid. In contrast to this the variation in the chain length of the fluorinated molecules leads to a change in the interaction between the fluorinated molecules $U_{\text{CF-CF}}$ and in the interaction between the lipids along the domain boundary $U_{\text{CF-CH}}$.

It is well known from measurements of hydrocarbon-fluorocarbon mixtures in liquid mixtures as well as in gaseous phase that the pair interaction between these two molecules $U_{\text{CF-CH}}$ is extremely weak and can therefore be neglected [Rowlinson, 1969; Dantzler-Siebert & Knobler, 1971]. Therefore, to quantify the line tension for different fluorinated molecules it can be assumed that a change in the chain length has only influence in the chain-chain interaction $U_{\text{CF-CF}}$. According to this, an elongation of fluorinated chains would increase $U_{\text{CF-CF}}$ and thus ΔU, respectively λ. But this effect should lead to bigger micro-domains for longer chains so that this assumption is contradictory to the observed behavior.

It suggests again that a not negligible additional contribution for a height mismatch $U_{\text{chain-air}}$ has to be taken into account for the interaction between fluorocarbon and hydrocarbon lipids along the domain boundary $U_{\text{A-B}}$. Even with an increasing pair interaction between fluorocarbon chains $U_{\text{CF-CF}}$ this effect is over-compensated by the vanishing of the contribution $U_{\text{chain-air}}$ for an elongation of the fluorinated molecules. This leads to a reduction in line tension and can therefore explain the observed behavior.

3.5 Influence of Number of Chains

As a modification in the degree of fluorination without elongation of the fluorinated molecule an amphiphil with a third fluorinated chain FT10 was synthesized. With this molecule it should be proved that the formation of micro-domains and their lateral dimensions is not influenced by the fluorination per molecule, but does only depend on the length of the contact area between lipids at the domain boundary.

Fluorescence images of mixed monolayers incorporating micro-domains at a molar fraction of χ_{Fn10} = 33 mol% for FT10 (Fig. 3.5.1(a)) and FL10 (Fig. 3.5.1(b)) are presented. From these no significant change in the appearance and distribution could be observed.

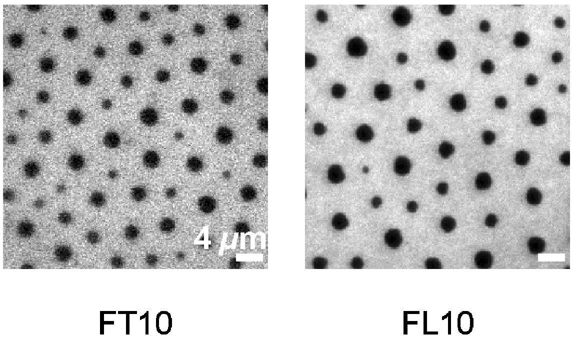

Fig. 3.5.1 Fluorescence images of mixed monolayers showing micro-domains of fluorinated molecule FT10 (left) and FL10 (right) at a molar fraction of χ_{Fn10} = 33 mol%. In both monolayers domains with equally size and distance distribution can be observed.

Fluorescence images of mixed lipid monolayers were analyzed to determine FT10 micro-domain mean diameter $\langle d_{\mathrm{FT10}} \rangle$, mean nearest neighbor distance $\langle r_{\mathrm{FT10}} \rangle$, radial distribution function $g_{\mathrm{FT10}}(r)$ and the potential of mean force $-ßw_{\mathrm{FT10}}(r)$. Spring constants could be obtained from the fit of the first minimum in the PMF and verified an identical displacement even in the presence of a third fluorinated chain with CF_3 terminus.

Additional grazing-incidents x-ray experiments were performed on free floating monolayers to prove the preserved upright orientation and hexagonal packing of the FT10 molecules within the micro-domains.

3.5.1 Mean Micro-Domain Diameter $<d_{Fn10}>$ and Nearest Neighbor Distance $<r_{Fn10}>$

Compared with previously obtained values for the mean diameter and mean nearest neighbor distance for FL10 micro-domains (see Chapter 3.4.2) no significant change could be determined for the fluorinated molecules with three fluorinated chains FT10.

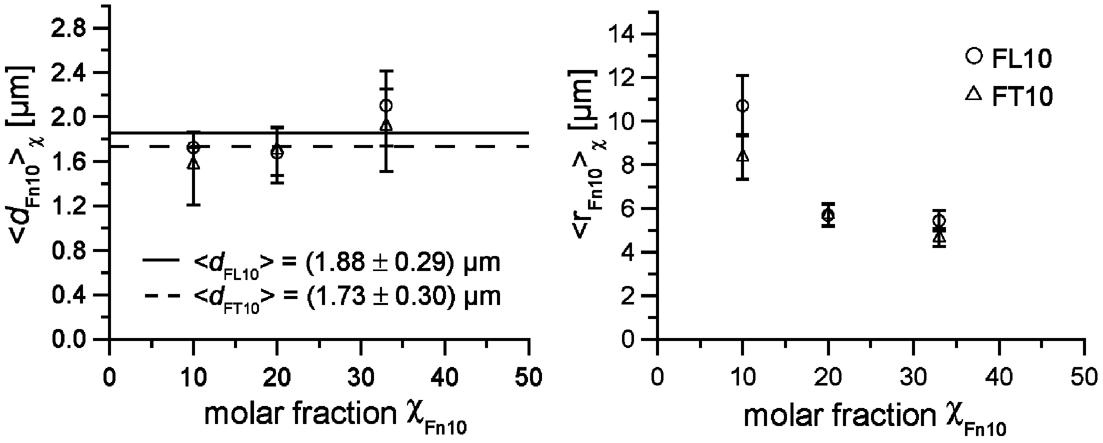

Fig. 3.5.2 (left) The mean diameter of micro-domains $<d_{Fn10}>_\chi$ vs. the molar fraction χ_{Fn10} for FT10 (n = T) and FL10 (n = L) and (right) the corresponding mean distance $<r_{Fn10}>_\chi$ vs. the molar fraction χ_{Fn10}.

The mean diameter for FT10 micro-domains ($<d_{FT10}>$ = (1.73 ± 0.3) μm, dashed line) is in a comparable range as the mean diameter of FL10 micro-domains ($<d_{FL10}>$ = (1.88 ± 0.29) μm, solid line) (see Fig. 3.5.2(left)). This emphasizes the approach in Chapter 3.2, that a height mismatch between the phospholipid matrix and the fluorinated molecule at the domain boundary is the dominating contribution in tuning the domain size. The introduction of a third fully fluorinated chain had obviously no influence on both the line tension and the dipole density of a micro-domain.

The observed repulsive potential found for the fluorinated molecules with varying chain length is preserved as well for FT10 compared to FL10. Therefore an increase in the micro-domain distance can be observed for a decreased density of FT10 micro-domains in a monolayer, owing to a lower molar fraction χ_{FT10} (see Fig. 3.5.2(right)).

3.5.2 Radial Distribution Function $g_{Fn10}(r)$ and Potential of Mean Force $-ßw_{Fn10}(r)$

For FT10 micro-domains the radial distribution function $g_{FT10}(r)$ is determined for various molar fractions χ_{FT10} = 10, 20, 33 mol% in the same way as for the fluorinated molecules FL10, FL13 and FL17 (details can be found in Appendix A.4).

In Fig. 3.5.3 $g_{Fn10}(r)$ for FT10 and FL10 at a molar fraction of χ_{Fn10} = 33 mol% is presented versus the normalized distance $r/<d_{Fn10}>$ where $<d_{Fn10}>$ is the corresponding mean micro-domain diameter. The domain correlation in the arrangement of FT10 and FL10 micro-domains is almost identical.

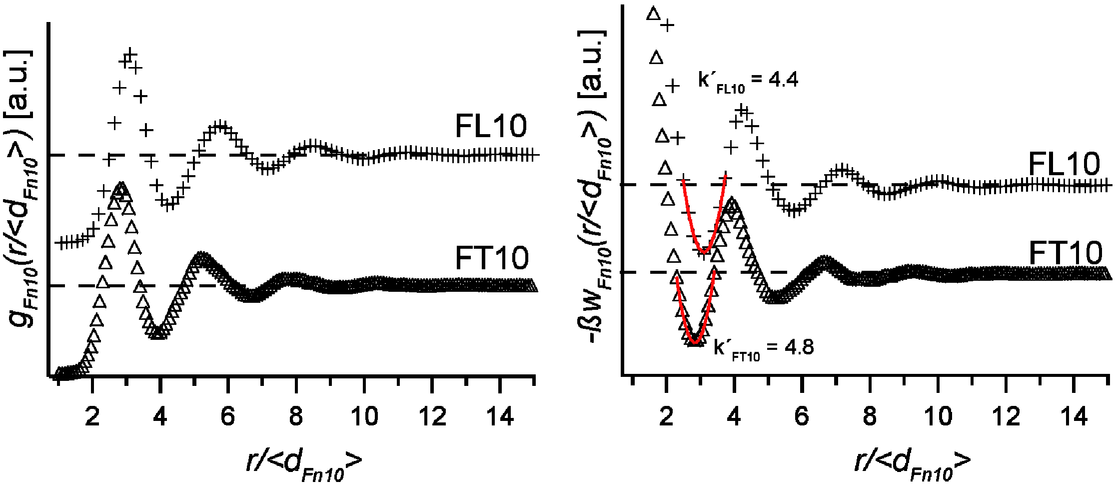

Fig. 3.5.3 (left) The radial distribution function $g_{Fn10}(r)$ and (right) potential of mean force $-ßw_{Fn10}(r)$ vs. the normalized distance $r/<d_{Fn10}>$ for monolayers incorporating FT10 and FL10 at χ_{Fn10} = 33 mol%.

As for FL10 micro-domains, also here a periodical oscillation up to the third order can be identified.

The potential $-ßw_{FT10}(r)$ calculated for $g_{FT10}(r)$ exhibits the same depth and width for FT10 as for FL10 domains. This implies that the dipole moment of a micro-domain remains constant although the molecular dipole moment m increases an additional chain terminus CF_3. On the other hand the number of molecules in a micro-domain formed of FT10 should be less in the same ratio, owing to the increased space requirement of the FT10 molecule.

The position of the first order minimum in $-ßw_{FT10}(r)$ for FT10 $<r_{FT10}>_{PMF}$ = (5.5 ± 0.8) μm also exhibits a slight shift to bigger distances, as for the mean nearest neighbor distance $<r_{\mathrm{FT10}}>$ = (4.5 ± 0.4) μm, observed already for the compounds with varying chain length. Also the calculated spring constant k'_{FT10} = (4.8 ± 0.1) is comparable to the one of FL10 k'_{FL10} = (4.4 ± 0.1).

3.5.3 GIXD Measurements

For the molecule FL10 the micro-domain substructure was determined by grazing-incidence X-ray diffraction measurements for FT10 on mixed monolayers at the air/water interface, to verify that the third chain has also no significant influence on the chain-chain correlations within a FT10 micro-domain.

A molecular distance d^{mo}_{FT10} = (5.72 ± 0.01) Å for FT10 was obtained, which is again comparable to the measured values for FL10.

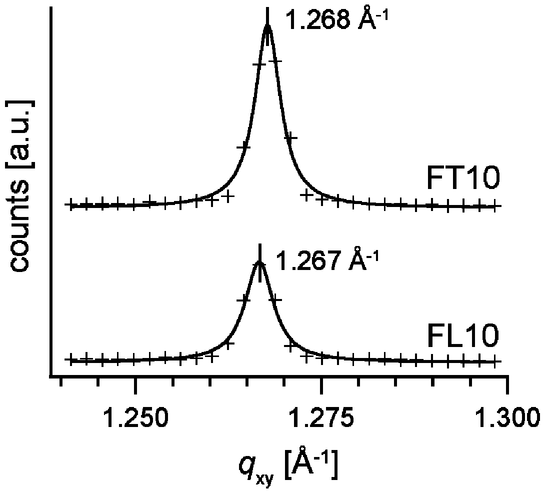

Fig. 3.5.4 Integrated GIXD diffraction intensities of mixed monolayers incorporating FT10 and FL10 vs. q_{xy} at a surface pressure of 10mNm^{-1}

The third chain has therefore no influence on the upright orientation and the hexagonal packing of the fluorinated chains in the FT10 micro-domains.

3.6 Influence of Polar Head Groups

For further μ-fluidic applications presented in Chapter 4, a bio-functional fluorinated molecule FL10man was synthesized based on the fluorinated anchor molecule FL10. As presented in Chapter 1.1.1 the molecule posses an α-D-mannose sugar moiety as head group to make the fluorinated molecules attractive for mannose binding cells and bacteria.

In Fig. 3.6.1 mixed monolayers with FL10man (left) and FL10 (right) micro-domains at a molar fraction of χ_{FL10n} = 33mol% are presented. Obviously FL10man micro-domains become stable at smaller diameters.

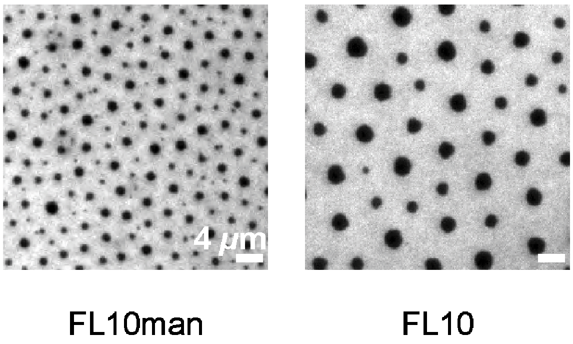

Fig. 3.6.1 Fluorescence images of mixed monolayers of FL10man (left) and FL10 (right) at χ_{FL10n} = 33mol% show a change in both size and distance distribution.

The modified head group of FL10man is more polar than a simple OH group and causes therefore additional attractive head group-head group (head-head) interactions that have no significant influence on the de-mixing and self-assembling properties of the FL10man molecule but on the micro-domain size and therefore on the distance distribution. This could be verified by the use of image processing in the same way as shown for FT10 and FL13 and FL17 respectively. By grazing incidence X-ray diffraction measurements the upright orientation and the preservation of the hexagonal packing within the FL10man micro-domains was verified mandatory for the free accessibility of the mannose functionalization, tested in a first cells experiment.

3.6.1 Mean Micro-Domain Diameter $<d_{\mathrm{FL10n}}>$ and Nearest Neighbor Distance $<r_{\mathrm{FL10n}}>$

Mixed monolayers with a molar fraction χ_{FL10man} = 5, 10 and 33 mol% of FL10man are spread at the air/water interface of a Langmuir trough and compressed to a transfer pressure of Π = 25 mNm^{-1}. Since both, fluorescence images taken as in Chapter 3.2 (data is not shown in this work), and GIXD measurements on mixed monolayers (data can be found in App. 2) verified the stability of micro-domains this target pressure, which is closer to the internal pressure of natural lipid bilayer membranes was chosen.

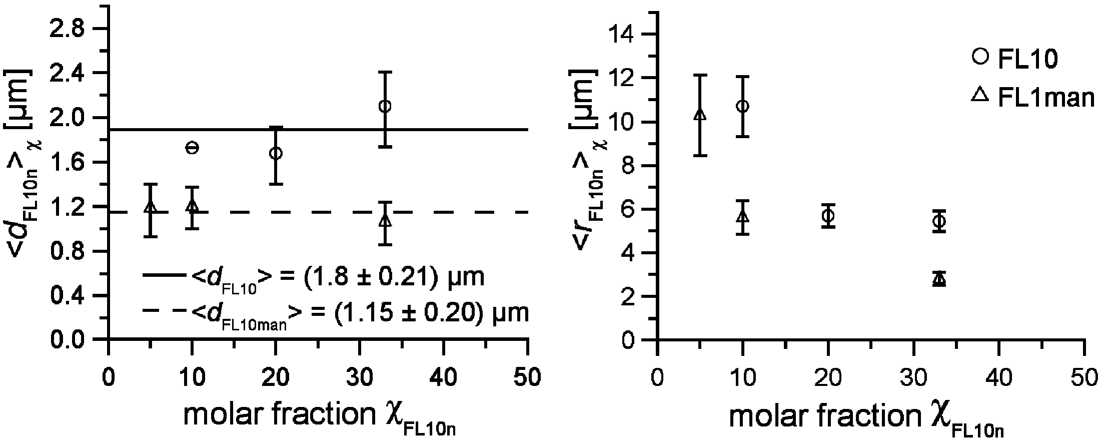

Fig. 3.6.2 (left) Mean diameter of micro-domains $<d_{\mathrm{FL10n}}>$ vs. the molar fraction χ_{FL10n} of FL10man and FL10. In contrast to FL10 the micro-domain diameter remains constant even for $\chi_{FL10man}$=5 mol%. (right) The mean nearest neighbor distance vs. χ_{FL10n}.

A mean micro-domain diameter for FL10man $<d_{\mathrm{FL10man}}>$ = (1.16 ± 0.20) μm was obtained from image processing, presented in Fig. 3.6.2 (left). Thus verifies that the equilibriums radius of the FL10man micro-domains is smaller than for FL10 domains ($<d_{\mathrm{FL10}}>$ = (1.88 ± 0.29) μm), due to smaller line tension $\lambda_{\mathrm{FL10man}} < \lambda_{\mathrm{FL10}}$, caused by the additional head-head interactions.

Even at a low molar fraction (5 mol%) the smaller FL10man domains take a circular shape, owing to a modified line tension term F_λ in the free energy in Equation (3.4). The contribution of the sugar head-group to the molecular dipole moment μ is negligible. A decrease in the molar fraction of FL10man and therefore in the density of micro-domains leads to an increase in the micro-domain distance, shown in Fig. 3.6.2 (right).

Thus the additional head-head interaction does not interfere with the self-assembling properties of the fluorinated chains, but increase the stability of fluorinated micro-domains at higher surface pressures and smaller micro-domain diameters.

3.6.2 Radial Distribution Function $g_{\mathrm{FL10n}}(r)$ and Potential of Mean Force $-ßw_{\mathrm{FL10n}}(r)$

For biological applications a correlated arrangement of micro-domains is desired, to form adhesion spots for biological adhesion experiments. These spots shall be accessible in a distance, adjustable by the molar fraction of fluorinated compound mixed in the phospholipid matrix. To prove that the shown interaction was preserved even for the substitution of the head-group, analog to the influence of chain length and chain number the radial distribution function $g_{\mathrm{FL10man}}(r)$ was determined and thus the interacting potential $-ßw_{\mathrm{FL10man}}(r)$

The structured arrangement of FL10man micro-domains in the monolayer is shown in the comparison to FL10 presented in Fig. 3.6.3(left) normalized by the corresponding micro-domain diameter $<d_{\mathrm{FL10n}}>$.

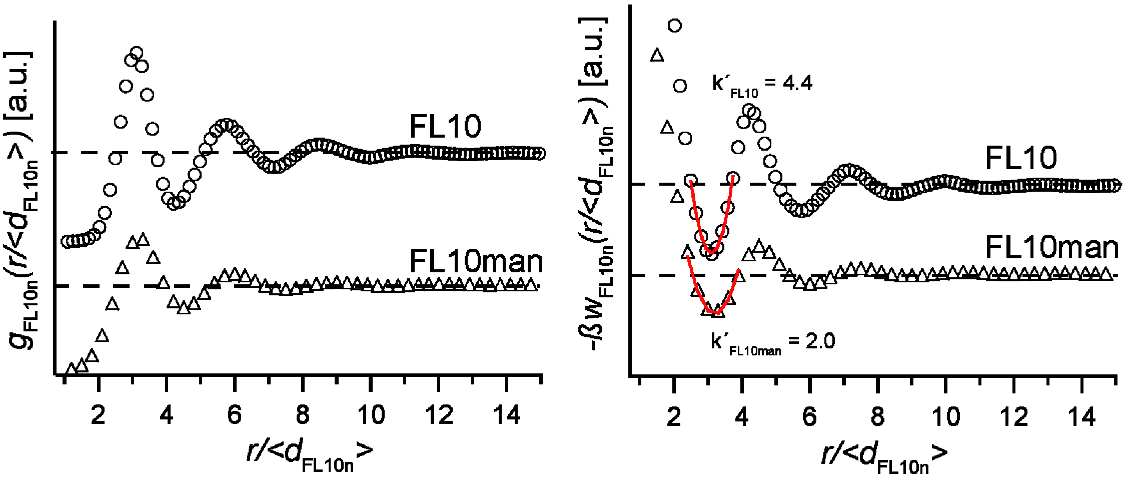

Fig. 3.6.3 (left) Radial distribution function $g_{FL10n}(r)$ vs. normalized distance r/d of FL10man compared to FL10 and (right) the potential of mean force $-ßw_{FL10n}(r)$ vs. normalized distance r/d.

While a periodicity in the arrangement of FL10 micro-domains can be observed up to the third order, the correlation in the arranged FL10man micro-domains is less strong.

This weaker interaction between the FL10man micro-domains is reflected as well in the strength of the potential of mean force $-ßw_{\mathrm{FL10n}}(r)$ vs. r/d presented in Fig.

3.6.3(right). The spring constant for FL10man $k'_{\mathrm{FL10man}} = (2.0 \pm 0.1)$ is less than for the pure anchor molecule FL10, $k'_{\mathrm{FL10}} = (4.4 \pm 0.1)$.

3.6.3 GIXD Measurements

To verify that the hexagonal packing is only determined by the pure fluorinated anchor molecules and not influenced by the additional influence of a sugar head-group, GIXD measurements were performed on mixed monolayers of DOPC with FL10man at a molar fraction of $\chi_{\mathrm{FL10man}} = 50$ mol%.

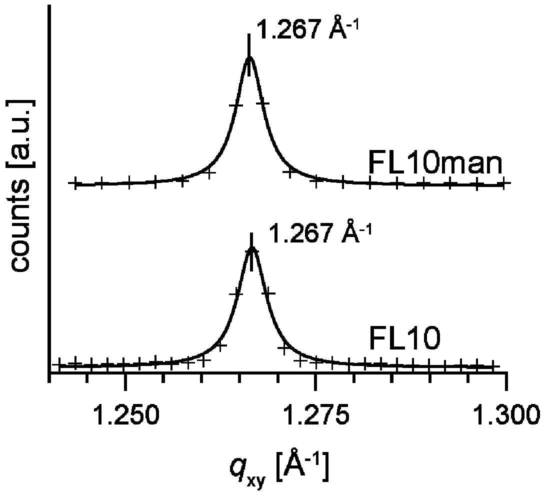

Fig. 3.6.4 GIXD Integrated GIXD diffraction intensities of mixed monolayers incorporating FL10man and FL10 vs. q_{xy} at a surface pressure of $10\mathrm{mNm}^{-1}$

Both fluorinated molecules exhibit a molecular distance of $d^{mo}_{FL10n} = (5.73 \pm 0.01)$ Å indicating no serious influence of the head-group in the chain-chain ordering. The upright orientation is preserved as well to guarantee a sufficient access to the sugar head-group by a mannose binding cell or bacteria.

3.6.4 Cell Incubation Experiment

In a first experiment to verify the bio-functionality of mixed monolayers incorporating FL10man, mannose binding cells (mouse macrophages J774) were incubated in a fluid cell for 20 h. In Fig. 3.6.5 bright field microscopy images are presented to show the clear evidence of the mannose recognition by the macrophages.

Cells were incubated in a fluid cell on (a) a pure DOPC monolayer and (b) a mixed monolayer incorporating a molar fraction of 33 mol% FL10man. After 20h incubation at 37° in a cell incubation chamber the cells incubated on the bio-functionalized surface the cells show spindle-like structures, indicating an activity, owing to the recognition of the mannose head-group in the mixed monolayer, while cells incubated on the DOPC surface show no change in shape.

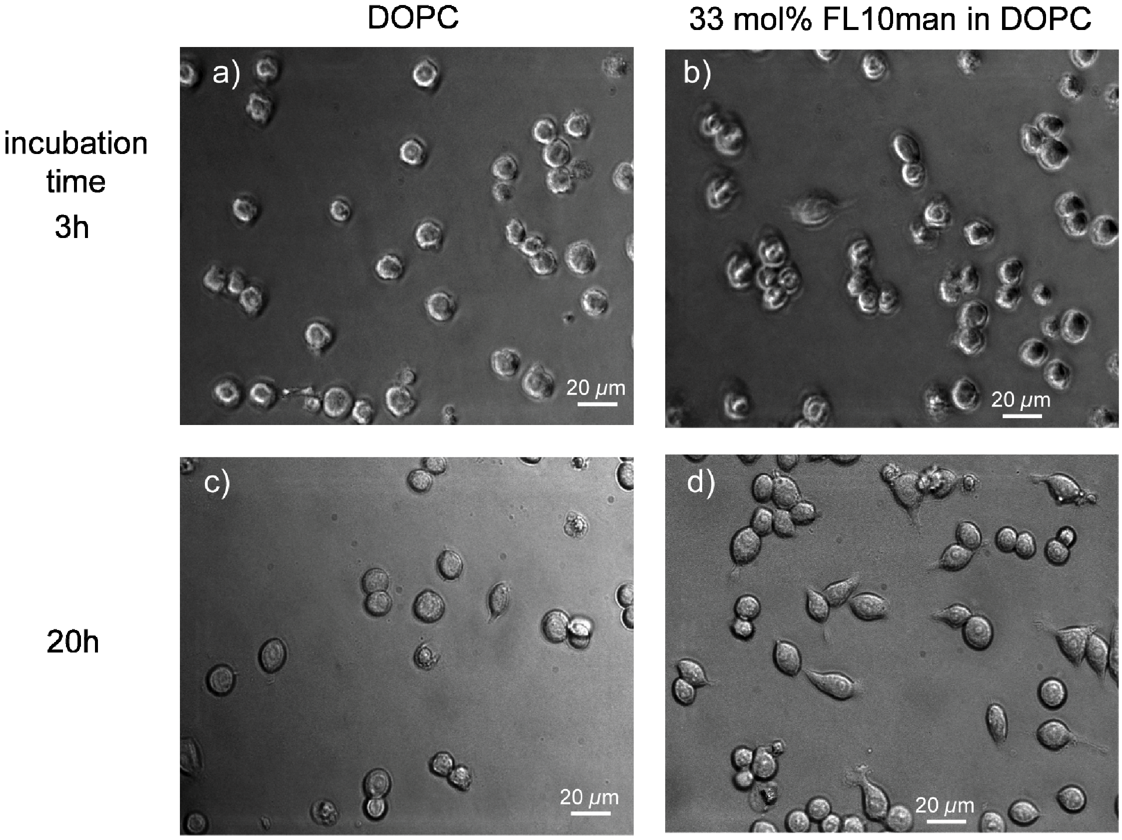

Fig. 3.6.5 Combined phase contrast and fluorescence images of mannose binding mouse macrophages (J774). Images were taken after 3h incubated in a fluid cell on (a) pure phospholipid monolayer and (b) on a mixed monolayer incorporating 33 mol% FL10man. Next images were taken after an incubation time of 20h the macrophages show a clear evidence for the recognition of mannose by forming spindle-like structures (d) in contrast to cells incubated on pure DOPC (c).

4 Applications of Fine-Tunable Artificial Lipid Domains in Cell Biophysics: Combination with Flat-μ-Fluidics Technology

4.1 Introduction

In this chapter first μ-fluidic experiments employing a so-called “flat-μ-fluidic” setup are reported. It is demonstrated that half cylindrical water channels on a solid support can be successfully functionalized with lipid bilayer membranes. These bilayers were structured and laterally patterned, as described in Chapter 3. The principle of acoustic streaming was used as a fine-tunable μ-pumping technique for flat-μ-fluidic channels.

Photolithography was used for photochemical surface structuring to form μ-fluidic channels in a circular layout on the chip surface. The channels were generated by a hydrophobic/hydrophilic surface contrast and have a half cylindrical profile.

Flow experiments employing fluorescently labeled beads as tracer particles yielded an estimate for the achieved shear rates with respect to the applied streaming velocities within the chosen channel geometry.

To functionalize the flat-μ-fluidic channels with an asymmetric phospholipid bilayer membrane, incorporating fluorinated micro-domains, position sensitive combined Langmuir-Blodgett (LB) and Langmuir-Schaeffer (LS) transfers were performed. During the deposition process, the position sensitive application of a lipid bilayer membrane in the μ-fluidic channel was achieved by a removable protective sheet.

First experiments with a mannose binding bacteria strain (E.Coli H101 (pPKl4)) demonstrated the feasibility of acoustic streaming to perform flow chamber experiments in a flat-μ-fluidic setup.

4.2 *μ*-Fluidic Pumping – Acoustic Streaming

Commonly used *μ*-fluidic setups utilize syringe or peristaltic pumps to agitate fluids (usually several ml) in either open or closed tube systems in order to rinse a sample fluid through *μ*-channels.

Here, the application of a *μ*-pump for *μ*-fluidic experiments is presented utilizing the principle of acoustic streaming to generate liquid flow in a *μ*-channel. This technique is based on the conversion of acoustic waves in solids close to the surface, the so-called surface acoustic waves (SAW), into acoustic waves in fluids. Hence, a streaming is generated within the fluid according to the principles of acoustic streaming [Nyborg, 1965].

Acoustic streaming has already been used for applications like mixing in extremely small volumes (droplets) [Strobel, 2005]. Furthermore, if a surface acoustic wave high with sufficient power is applied, a droplet can even be moved on a hydrophobic surface by the acoustic field [Wixforth et al., 2004].

4.2.1 Acoustic Waves in Solids

Oscillations close to a solid surface have been discussed by Lord Rayleigh in his mathematical investigations about seismic waves in the year 1885 [Rayleigh, 1885]. His formulations for oscillations in solids were derived from continuum theory and can be expanded to the situation found in piezoelectric solids.

According to the continuum theory, a solid can be considered as formed by infinitesimal volume elements ΔV. In the context of these theoretical descriptions, the coordinates are named x_i.

A deformation of the solid along x causes a displacement $u(x)$ of a volume element, whereby the distances between neighbouring volume elements are changed. Without these change in the neighbouring distances the displacement would be just a simple translation.

With Einstein's sum convention the distortion tensor S_{ij} for the solid is given by

$$S_{ij} = \frac{1}{2}\left(\frac{\partial u_k}{\partial x_j} + \frac{\partial u_l}{\partial x_k} \right). \tag{4.1}$$

In contrast to the general formulation here the quadratic term was omitted and the tensor exhibits the symmetry $S_{ij} = S_{ji}$.

Beside this the Newtonian equation of motion for a volume element ΔV can be written as

$$\rho \frac{\partial^2 u_i}{\partial t^2} = \frac{\partial T_{ij}}{\partial x_j}\,, \tag{4.2}$$

where T_{ij} is the tension tensor.

Both tensors, S_{ij} and T_{ij} are linked by the generalized Hooks law

$$T_{ij} = c_{ijkl} S_{kl}\,. \tag{4.3}$$

The coupling tensor c_{ijkl} is a tensor of forth degree and usually possess 81 entries.
But by taking the symmetry of both tensors, S_{ij} and T_{ij} into account and together with the Poynting-Theorem,

$$c_{ijkl} = c_{jikl} = c_{ijkl} = c_{jilk}\,, \tag{4.4}$$

the total number of relevant entries of c_{ijkl} can be reduced to 21.

For piezoelectric materials Hooks law, Equation (4.3), has to be extended by the electrical field **E**.
Thus the continuity equations can be derived to

$$T_{ij} = c_{ijkl} S_{kl} - p_{kij} E_k \tag{4.5}$$

$$\text{and} \qquad D_i = \varepsilon_{ij} E_j - p_{ijk} S_{jk}\,. \tag{4.6}$$

Here, p_{ijk} is the piezoelectric tensor, $\varepsilon_{\mathrm{ij}}$ the dielectric tensor and **D** the dielectric displacement.
The electric field **E** is defined by the electric potential Φ via the relation

$$E_i = -\frac{\partial \Phi}{\partial x_i}\,. \tag{4.7}$$

For the assumption of no free charges (div **D** = 0), and with Equation 4.1, 4.2 and 4.6 one obtains the 4 basic, coupled wave equations for the piezoelectric solid:
One for the electric potential Φ and three for the mechanical displacement $u(x)$,

$$\rho \frac{\partial^2 u_j}{\partial t^2} - c_{ijkl} \frac{\partial^2 u_k}{\partial x_i \partial x_l} - p_{kij} \frac{\partial^2 \Phi}{\partial x_i \partial x_k} = 0 \tag{4.8}$$

$$\text{and} \qquad p_{ikl} \frac{\partial^2 u_k}{\partial x_i \partial x_l} - \varepsilon_{ik} \frac{\partial^2 \Phi}{\partial x_i \partial x_k} = 0\,. \tag{4.9}$$

4.2.2 Bulk Acoustic Waves and Surface Acoustic Waves

The solution of Equation (4.8) and (4.9) for acoustic waves in a solid volume without boundary conditions is the so-called bulk acoustic wave (BAW).

It can be shown that the piezoelectric properties of a solid lead to a stiffening of the crystal and an increase in the acoustic wave velocity, since the coupling factor c_{ijkl} in Hooks law increases with a factor of $(1+K_{eff}^2)$ [Frommelt, 2007]. The so-called electromechanical coupling coefficient K_{eff}^2 is given by

$$K_{eff}^2 = \frac{p^2}{\varepsilon c}. \tag{4.10}$$

K_{eff}^2 is a measure of the efficiency of a given piezoelectric crystal in converting an applied electrical signal into mechanical energy.

In the case of a existing boundary of the solid to vacuum, for instance in $x_3 = 0$, one obtains an additional condition. The tension tensor has to vanish at all surfaces of a volume element ΔV

$$T_{31} = T_{32} = T_{33}, \text{ for } x_3 = 0. \tag{4.11}$$

Taking this into account, a solution of the Equations (4.8) and (4.9) is the so-called surface acoustic wave (SAW).

This wave propagates along the surface with a wave velocity v_{SAW}, while its amplitude and potential vanishes within several wave lengths inside the solid. The motion of an excited SAW in a piezoelectric material is depicted schematically in Fig. 4.2.1.

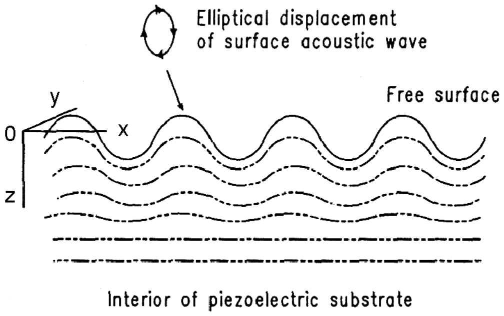

Fig. 4.2.1 Sketch of the propagating of a surface acoustic wave in an elastic solid (from [Campbell, 1998]).

Atoms close to the surface follow a retrograde movement with contributions of a compression wave and a shear wave coupled in a fixed ratio. In addition one has to mention that both mechanical waves are accompanied by an electrostatic wave.

In the case of a SAW, the electromechanical coupling coefficient K_{eff}^2 cannot be calculated as presented for the BAW, since the relationship between the electric potential Φ and the displacement $u(x)$ varies with altering distance to the solid boundary.

Therefore K_{eff}^2 has to be determined experimentally, for instance by measuring the change in the SAW velocity $\Delta v_{SAW} = v_{SAW}^{free} - v_{SAW}^{film}$ caused by the coating of the free surface in Fig. 4.2.1 with a thin highly conducting metal film.

K_{eff}^2 can then be calculated by the relation

$$K_{eff}^2 = -2\frac{\Delta v_{SAW}}{v_{SAW}}. \tag{4.12}$$

as demonstrated by Campbell [Campbell, 1998].

The propagation direction, K_{eff}^2 and the velocity v_{SAW} is presented for various piezoelectric materials in Appendix A.7.

4.2.3 Inverse Piezoelectric Effect - Interdigital Transducer (IDT)

The principal of exciting a mechanical wave by applying an external alternating electric field at a piezoelectric crystal is based on the inverse piezoelectric effect.

The piezoelectric effect, discovered by Pierre and Jacques Curie 1880, describes the generation of an electrical potential upon deformation of special crystals. Such crystals lack inversion symmetry and, hence, a deformation leads to polarization and the formation of electric fields.

For the inverse piezoelectric effect, a voltage is applied at electrodes attached to a piezoelectric crystal, which leads to mechanical stress within the substrate. The deformation of the piezoelectric crystal persists until the external potential is altered. Thus, a single and short electric impulse leads to a single expansion or contraction of the crystal. An external alternating electric field $\boldsymbol{E}(t)$ applied at electrodes leads therefore to an excitation of a periodic mechanical wave.

The wavelength λ_{SAW} for a surface acoustic wave is given by the relation

$$\lambda_{SAW} = \frac{v_{SAW}}{f_E}, \tag{4.13}$$

where v_{SAW} is the propagation velocity of the SAW in the crystal, owing to its material parameters, and f_{E} the frequency of the external alternating electrical field $\mathbf{E}(t)$. Therefore an additional charge at a neighboring electrode in the distance λ_{SAW} after a time $T = 1/f_{\mathrm{E}}$ leads to an amplification of the first passing wave.
The amplitude of the excited wave thus scales with the number of electrodes. To utilize this principle, a number of capacitors electrodes were deposited on the crystal. These so called Inter-Digital Transducers (IDT's) were presented first by White and Voltmer [White & Voltmer, 1965].

Since piezoelectric materials are anisotropic crystals, they possess at least two different, perpendicularly oriented propagation directions, with different acoustic properties, owing to the altering material parameters for different orientations. In the following the space coordinates of the piezoelectric crystal are denoted by X, Y, Z according to the commonly used nomenclature in piezoelectric applications.

The IDT fingers depicted in Fig. 4.2.2 are exemplarily aligned parallel to the Y-direction of the crystal and therefore the capacitors excite only SAW's with propagation direction in X, indicated by fat black arrows.

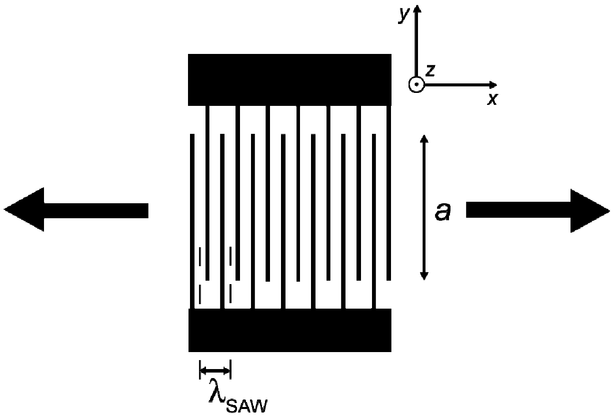

Fig. 4.2.2 Sketch of an Inter-Digital Transducer (IDT). The IDT acts as exciter of a surface acoustic wave (SAW). The alignment of the IDT fingers is here parallel to Y so that the propagation direction is therefore along the X-axis, depicted with big arrows.

The aperture *a* of the IDT, defined by the overlap of the complementary capacitor fingers, also determines the width of the propagating wave. In order to achieve maximum coupling, *a* was adjusted to the μ-fluidic channel width.

4.2.4 Acoustic Streaming in Fluids

From theoretical considerations, based again on continuums theory, it can be derived that only waves with a non-vanishing amplitude contribution along the crystal surface normal are able to couple from a solid into a fluid. Since Rayleigh waves and therefore surface acoustic waves represent such modes, they are able to generate longitudinal acoustic waves in an additional layer with sufficient thickness, applied to the solid surface [Strobel, 2005].

Consider a SAW propagating along the crystal surface. Once the SAW reaches a region, loaded with water, as indicated in Fig. 4.2.3, the wave is attenuated by the so-called out-of plane damping, i.e. a conversion of the transversal acoustic wave in the solid with to a longitudinal acoustic wave in the fluid bulk.

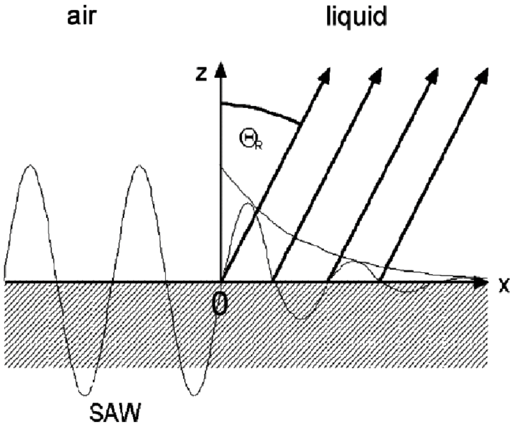

Fig. 4.2.3 Schematic illustration of a SAW coupled into water and converted to a acoustic pressure wave radiated under the Rayleigh angle Θ_R into the fluid (from [Wixforth, 2004])

The 1/e penetration length l_{op} of the SAW underneath the water was exemplarily determined for a $LiNbO_3$ 128° rot Y-cut crystal to $\sim 12\lambda_{SAW}$. Within this length scale the incoming SAW is attenuated to 1/e of its incident amplitude contribution along the crystal surface normal. For a typical frequency of f_E = 150 MHz and the SAW velocity for this crystal cut, the penetration length l_{op} can be determined to $l_{op} \approx 300\mu m$.

Along this distance a row of phase shifted point oscillators can be assumed, according to Huygen's Principle. Starting from these the excited longitudinal acoustic waves generate a plane wave front travelling through the fluid. This wave front is propagating under the Rayleigh angle Θ_R with respect to the chip surface normal given by

$$\Theta_R = \arcsin\left(\frac{v_{fliud}}{v_{SAW}}\right). \tag{4.14}$$

Here, v_{fluid} is the acoustic velocity in fluid, while v_{SAW} is the SAW velocity of the substrate. For $LiNbO_3$ the typical Rayleigh angle is about $\Theta_R = 22°$ [Strobel, 2005].

During the propagation of the excited longitudinal acoustic wave also this wave is attenuated and a penetration length l_{fd} within the fluid can be defined. This penetration length is dependent on the impinging SAW frequency f_{E} and can be given by

$$l_{fd} = \frac{a_{H_2O}}{f_E}. \tag{4.15}$$

In this equation a_{H2O} is a material parameter for water and dependent on its temperature T_{H2O}. Literature values for various water temperatures can be found in Appendix A.6.
Typically the penetration length l_{fd} of an excited longitudinal acoustic wave in water at $T_{\mathrm{H2O}} = 20°$ is about $l_{\mathrm{fd}} = 0.9$ mm, according to Equation (4.15). Geometrically the excited wave within the fluid has almost vanished until it reaches the top level of the channel geometry.

Caused by the damping along the propagation direction of the acoustic wave, an acoustic radiation pressure p_{S} is generated. The absolute value of the pressure p_{S} can be expressed by the relation

$$p_S = \rho_0 v_{SAW}^2 \left(\frac{\Delta\rho}{\rho_0}\right)^2. \tag{4.16}$$

Here, ρ_0 is the equilibrium density of the fluid and $\Delta\rho$ the change in the density, caused by a longitudinal acoustic wave in the fluid [Rayleigh, 1905]. In order to equalize this pressure gradient streaming is induced within the fluid: the so-called acoustic streaming.

To utilize this principle of acoustic streaming in μ-fluidic applications, commonly a square channel layout, filled with water is placed close to an IDT on top of a piezoelectric crystal. A SAW is excited close to the water and is coupled into the channel along one side of the square. The pressure p_s generated by the damping of the longitudinal acoustic wave in the fluid then creates a circular flow, as depicted schematically in Fig. 4.2.4.

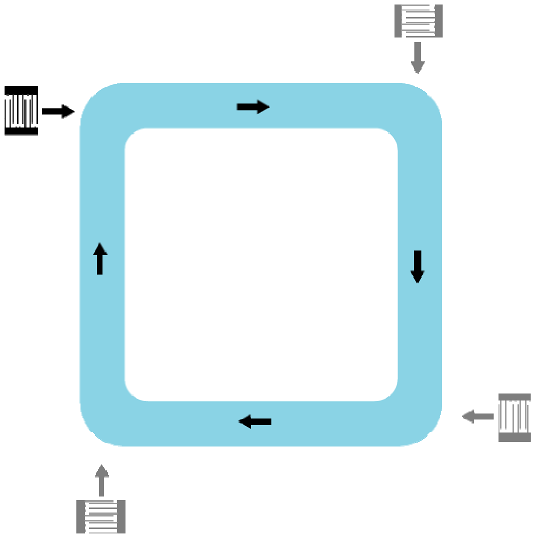

Fig. 4.2.4 An excited SAW propagates to the edge of a water filled channel and gets damped within the fluid. The generated flow, owing to the pressure wave is illustrated with small arrows in the channel. Indicated in light grey are additional IDT's as additional pumps to gain greater streaming

To use the pumping effect based on acoustic streaming, a SAW has to be excited by an IDT close to a water channel placed on top of the chip surface, without being blocked by any mass load in between.

The simultaneous use of more than one IDT is possible in order to gain higher flow velocity within the fluid.

4.3 Fluidics in Flat-*μ*-Fluidic *μ*-channels

In fluid dynamics, the streaming in a given geometry can be described by the flow velocity field **u**(x,t) with respect to point x and time t.
Here, a Newtonian viscous fluid is considered for which the shear stress τ is proportional to the gradient du/dz, i.e.

$$\tau = \eta \frac{du}{dz}, \tag{4.17}$$

with η as the viscosity coefficient of the fluid. Many real fluids, like water or oil behave according to Equation (4.17), over a wide range of environmental conditions.

4.3.1 Theory of viscous flow – The Navier-Stokes Equation

In case of viscous flow, a Newtonian fluid with constant density ρ and viscosity η is considered. Since the Euler equations only describe the motion of an ideal fluid with low viscosity a different formulation is required, the Navier-Stokes Equations [Acheson, 1990].
This set of equations takes into account the viscosity of the fluid and describes the motion of these fluids by the two relations

$$\rho(\frac{\partial u}{\partial t} + (u\nabla)u) = -\nabla p + \eta \nabla^2 u\ , \tag{4.18}$$

$$\text{and } \nabla u = 0\ . \tag{4.19}$$

Here, $\rho(\boldsymbol{u}\nabla)\boldsymbol{u}$ represents the mass inertia and $\eta\nabla^2\boldsymbol{u}$ is the viscous term. The incompressibility of the fluid leads to the simplification of the continuity equation for fluids in Equation (4.19).

To get a rough indication about the relative magnitudes of the both key terms in Equation (4.18), the Reynolds number R is defined.
Consider a viscous fluid in motion, and let U denote a typical flow speed and L a typical length scale of the streaming, then R is defined by the relation

$$R = \frac{\rho U L}{\eta} = \frac{\textit{inertia term}}{\textit{viscous term}} = \frac{|\rho(u \cdot \nabla)u|}{|\eta \nabla^2 u|}\ . \tag{4.20}$$

Since the first derivative of the streaming velocity with respect to length $\partial u/\partial x$ is in the same order as U/L and $\partial^2 u/\partial x^2$ as U/L^2 respectively, the Reynolds number can be rewritten as the ratio of the inertia and viscous term (see Equation 4.20). Thus, it is obvious that for a dominating viscous or inertia term the fluid shows a different physical behavior.

If $\eta\nabla^2\boldsymbol{u}$ is negligible against the inertia, i.e. a high Reynolds number $R >> 1$, effects like turbulences have to be taken into account. This is in contrast to the case of $R << 1$, in which for a dominating viscous term no such perturbations appear and a highly laminar flow can be considered.

In the fixed geometry considered in this work, a length scale in the order of 10^{-3} m is given, while the flow velocities are in an order of 10^{-3} - 10^{-4} m/s. This leads, together with the density and viscosity of water at room temperature to a Reynolds number of $R << 1$ and the case of a highly viscous flow can be assumed. Thus $\rho(\boldsymbol{u}\nabla)\boldsymbol{u} = 0$ and the Equation (4.18) can be rewritten into the so-called slow flow equations,

$$0 = -\nabla p + \eta\nabla^2 u \,, \tag{4.21}$$

$$\nabla u = 0 \,. \tag{4.22}$$

In the context of acoustic streaming, a steady laminar flow can be considered, i.e.

$$\partial u / \partial t = 0 \tag{4.23}$$

4.3.1 Flat-*μ*-Fluidic Channel Layout

For the formation of *μ*-fluidic channels, the principle of a so-called flat-*μ*-fluidic setup was used. Here, the substrate surface is chemically patterned in order to create a half cylindrical water channel on top of the surface.

By employing standard photolithographic processes a hydrophilic lane is prepared in a hydrophobic surrounding, as indicated in Fig. 4.3.1(a). The now generated contrast between the hydrophilic channel and the hydrophobic surrounding can be utilized to form a 'virtual' channel. If a suitable amount of water is added on top of the hydrophilic lane, the water only wets the surface within the prepared lane. Finally a half cylindrical water channel is formed, as shown in Fig. 4.3.1(b).

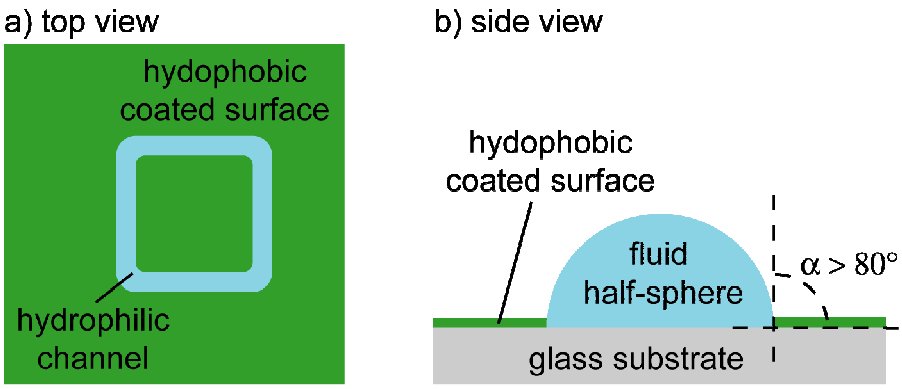

Fig. 4.3.1 (a) The hydrophilic channel filled with aqueous solution. (b) side view of the flat water channel forming a contact angle $\alpha > 80°$.

4.3.2 Finite Elements Model (FEM)

The streaming conditions of half cylindrical channels differ from the channels with three or four walls, commonly used in μ-fluidic applications. To get an impression of the expectable flow profile in the given half cylindrical μ-fluidic channel, illustrated in Fig. 4.3.2(a), a Finite Elements Model (FEM) of the used geometry was implemented in the physics modeling tool FEMLAB (COMSOL Multiphysics).

The side view of the channel shows a fluid with a velocity field pointing in x-direction, indicated by arrows. The boundary conditions for the flow profile, given by the geometry of the system, where defined as following.

- At the channel bottom ($z = 0$) a *no-slip* condition was assumed, since the fluid velocity at the solid/fluid interface should have a continuously transition. Thus $u(z = 0) = 0$ at the boundary since the bottom is in rest.
- In contrast to the fluid/solid boundary, along the half-spherical shape of the air/fluid interface a so-called slip condition was assumed. Here, the tangential and normal components of the fluid velocity and the surrounding air don’t have to be equal.

As can be seen in Fig 4.3.2(b) the velocity field increases in a parabolic shape in the channel with increasing height (z), but remains almost constant in y. Owing to boundary effects a region of interest is defined, indicated by a red box were a constant velocity field in y can be assumed for following flat-μ-fluidics experiments.

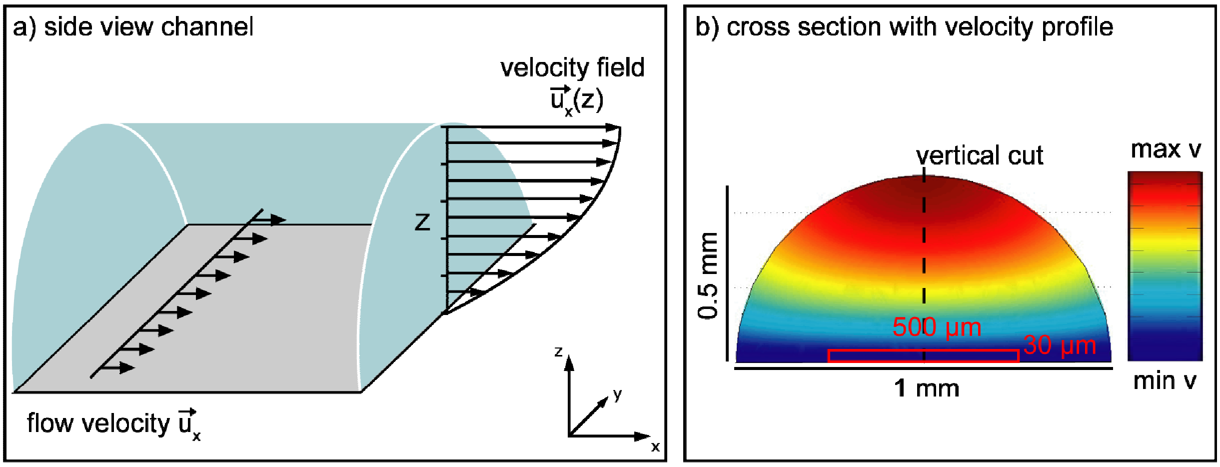

Fig. 4.3.2 (a) Schematic side view of the channel half-sphere and a parabolic velocity field **u**(*z*) indicated with arrows. (b) A cross section of the velocity profile **u**(*z*,*y*) calculated for a *μ*-fluidic channel with boundary conditions of non-slip at the solid/fluid and slip at the fluid/air interface, modeled with the fluidic simulation FEMLAB. A red box indicates a 500*μ*m x 30*μ*m region of interest located at the channel bottom.

For a vertical cut through the flow profile of Fig. 4.3.2(b), centered in the channel, the fluid velocity $u(z)$ vs. z and a shear rate $\partial u/\partial z$ vs. z is presented in Fig. 4.3.3.

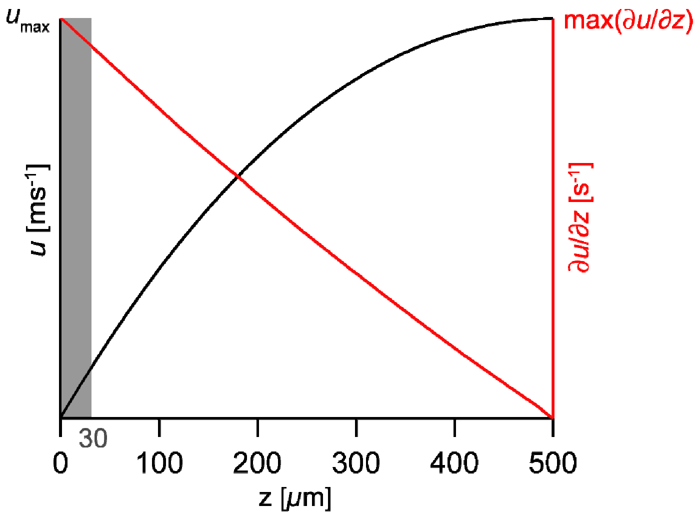

Fig. 4.3.3 Fluid velocity and shear rate of a half sphere channel along a line centered in the channel. The shear rate decrease with increasing height in the channel, and has therefore a maximum at the channel bottom.

While $u(z)$ shows the mentioned parabolic dependency, $\partial u/\partial z$ decreases with increasing height in the channel. The maximum shear rate is located at the channel surface resulting in the highest shear tensions τ_{max} according to Equation (4.17).

The defined region of interest for flat-μ-fluidic experiment is illustrated by the grey colored area in Fig. 4.3.3. It shows that at a maximum height of z = 30 μm, corresponding to the mean diameter of macrophages, the maximum shear rate can be assumed with a deviation of ~ 5 %.

To determine the shear rate for different fluid velocities, the flow profile centered in the channel was approximated with the parabolic behavior of a fluid flow through a pipe , the Hagen-Poiseuille flow profile [Acheson, 1990],

$$u(z) = u_{\max}(1 - \frac{z^2}{h^2}) \tag{4.24}$$

In this equation, the flow velocity of the maximum channel height h is equivalent to the radius R of the pipe. The FEMLAB modeled (black) and calculated (red) velocity profile show a good agreement as can be seen in Fig. 4.3.4.

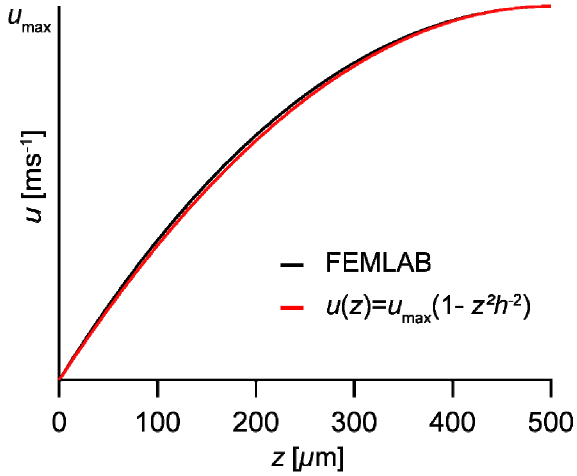

Fig. 4.3.4 Fluid velocity u vs. the channel height z for the FEM model solution (black) and the approximation of a pipe flow model (red). Both curves show a good agreement.

4.4 Experimental Components and Setup

The μ-fluidic application presented in this work is based on the surface functionalization of a piezoelectric crystal. As presented, these crystals can serve as μ-pump and agitate water in a predefined water channel layout, prepared on the crystal surface. These channels were prepared by a flat-μ-fluidics surface structuring to provide the experimental conditions for a further channel surface functionalization.

4.4.1 Piezoelectric Crystal and Electric Circuit Layout

In the presented work the piezoelectric chip material a $LiNbO_3$ 128° rot Y-cut crystal was used for the chips, i.e. the crystal was cut in an angle of 128° in respect to the Y axis. This cut direction exhibits a strong SAW propagation along the crystal X axis with best electromechanical coupling coefficient K_{eff}^2, see Appendix A.6, and enables the highest wave velocities v_{SAW} for the excitation of SAW's.

The bare crystal was structured with a circuit layout of IDT's, presented in Fig. 4.2.5, in order to accelerate SAW's in the four perpendicular directions in the X-Y plane.

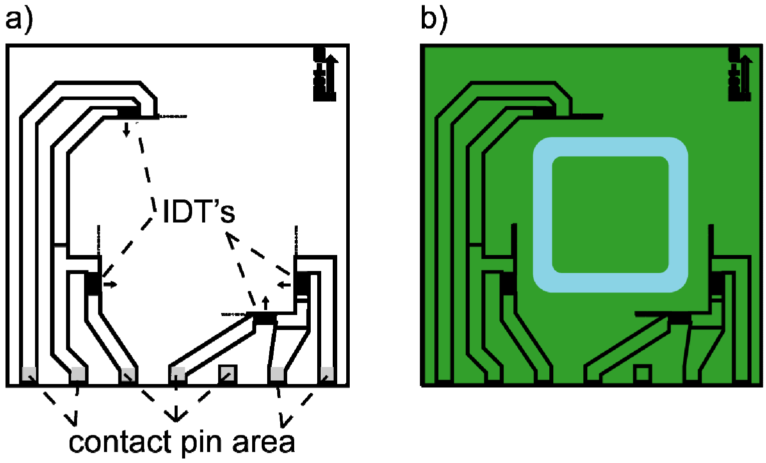

Fig. 4.4.1 (a) Sketch of the IDT layout applied to the bare $LiNbO_3$ 128°rot Y-Cut. The small arrows indicate the practical interesting propagation direction of the generated SAW. The grey highlighted pads are not covered with SiO_2 to enable the contact by a contact device. (b) The same chip as in (a) but structured with a flat-μ-fluidics layout. The blue highlighted line shall illustrate the hydrophilic area for the μ-channel, located within the acoustic patheay of the IDT's. The hydrophobic surface coating is illustrated in green color.

Subsequently the chip surface was coated with a thin layer of $Si0_2$ to enable the further surface structuring. Up to this step the chip was manufactured by the company

Advalytix AG (Brunntal, Germany, now part of Olympus Life Science Research Europe, Munich, Germany)
As already mentioned in Chapter 4.3.1, the surface structuring was done by the application of a flat-µ-fluidics layout by photolithography. For more details about the processing of the solid surface to obtain the flat-μ-fluidic channel see Appendix A.8.1.

The μ-fluidic channel layout used in the experiment comprises a channel with a width of 1mm and a length of a square side of about 8 mm.

4.4.2 Transfer of Asymmetric, Position Selective Deposited Lipid Bilayers into Flat-µ-Fluidic Channels

A so-called position selective transfer of an asymmetric bilayer was performed by a combined Langmuir-Blodgett, Langmuir-Schaeffer transfer using a PDMS protective sheet. Other techniques to coat the channel surface with a functionalized lipid bilayer have been tried out, but failed by various reasons. For more details about the different coating strategies, of vesicle fusion and a simple combined Langmuir-Blodgett, Langmuir-Schaeffer transfer, see Appendix A.7.

For the transfer as performed here, a PDMS protective sheet was prepared as described in the Appendix A.8.2. The PDMS protective sheet protects the chip surface from being coated with lipids, except of the parts open by cavities in the sheet, as depicted in Fig. 4.4.2.

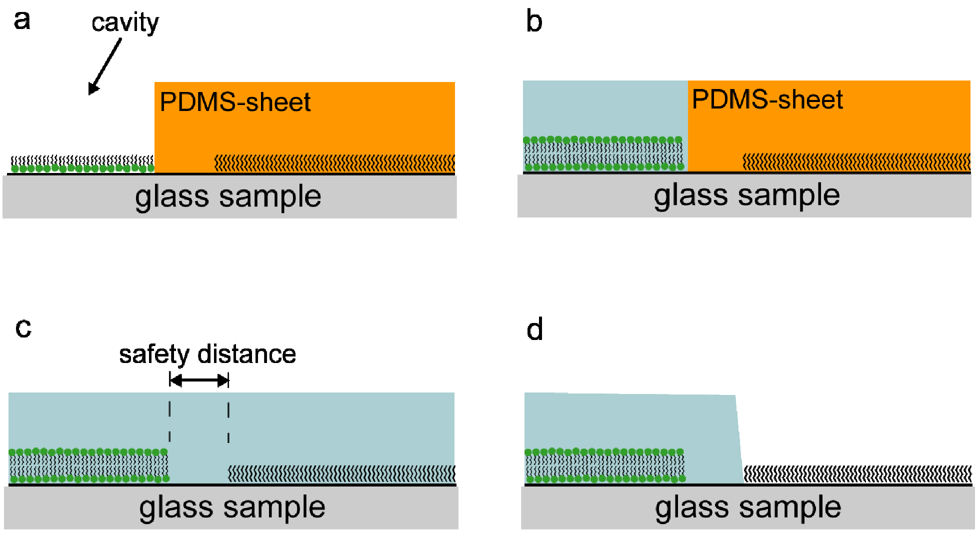

Fig. 4.4.2 Sketch of a two step Langmuir-Blodgett, Langmuir-Schaeffer transfer utilizing a protective PDMS-sheet.

The PDMS protective sheet was applied to the chip surface, before a monolayer was transferred into the flat-*µ*-fluidic channels. The such covered chip was immersed into the subphase of a Langmuir film-balance with dipping well and a monolayer of DOPC was spread and equilibrated at the air/water interface. A Langmuir-Blodgett transfer was performed to apply a lipid monolayer as the lower leaflet of the functionalized lipid bilayer membrane in the open cavity of the PDMS protective sheet (Fig. 4.4.2(a)). As upper leaflet a mixed monolayer incorporating FL10man at a distinct molar fraction was prepared.

To verify the de-mixing and self-assembling into micro-domains within the upper leaflet, the fluorescence probe Texas Red was added in a ratio of 0.1 mol%. Subsequently a Langmuir-Schaeffer transfer was performed on the PDMS-protected chip (Fig. 4.4.2(b)). After lifting-off the PDMS protective sheet under water, the channel bottom is partially coated by a functionalized asymmetric membrane, as it is depicted in Fig 4.4.2(c). Finally, while removing the chip from the water bath, a flat-*µ*-fluidic channel water with convex profile remains in the hydrophilic areas of the chip, forming the desired channel structure as indicated in Fig 4.4.2(d).

In Fig. 4.4.3(a) the chip layout is depicted with a desired surface structuring for flat-*µ*-fluidics.

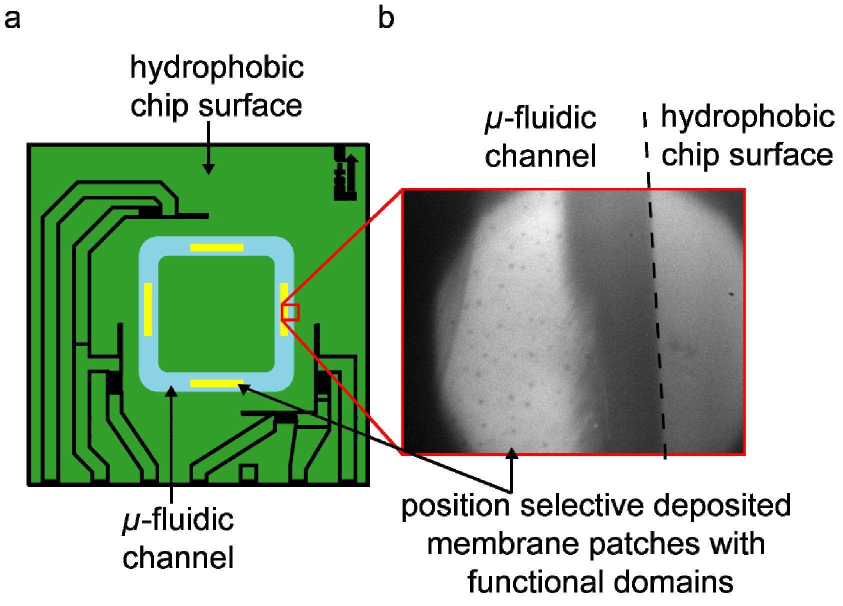

Fig. 4.4.3 (a) Sketch of the *µ*-fluidic chip layout. The zoom in shows a schematic view of the water filled channel in the hydrophobic surrounding. The channel is thereby covered with a functionalized membrane. The fluorescence image (b) verifies the successful transfer of a localized membrane

As a zoom in Fig. 4.4.3(b) the fluorescence image shows a cut out of the flat-μ-fluidic channel, structured with an asymmetric membrane.

The upper leaflet of the lipid bilayer incorporated 20mol% FL10man, so that the formed FL10man micro-domains are identifiable as dark spots. The dashed line indicates the channel border and therefore the hydrophobic/hydrophilic structuring. Between the membrane and the channel border a safety space of bare, uncoated glass can be seen.

4.4.3 High Frequency Contacting Device and Microscope Setup

To excite the surface acoustic waves on the previously described chip layout a contacting device connected to a temperature control unit was designed, as it is shown in Fig 4.4.4.

The setup consists of a poly-tetrafluoroethylene (PTFE, “Teflon”) frame with a square cutout, sealed by a glass cover slide. This window enables access to the flat-μ-fluidic channel with an upright microscope.

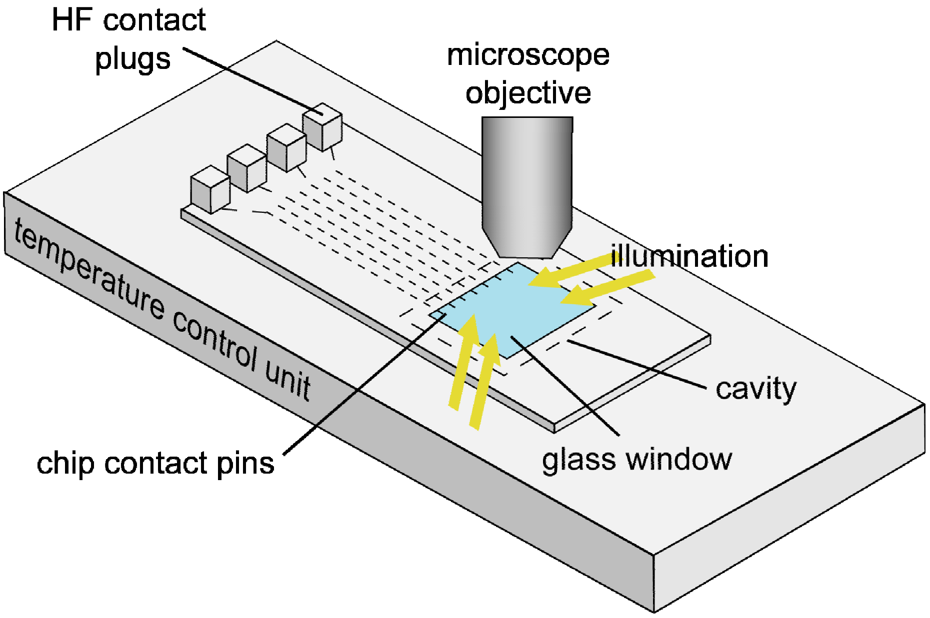

Fig. 4.4.4 Schematic view of the contacting device mountable on a heat control to perform temperature controlled micro-fluidic experiments

The contacting device itself serves at the same time as a humidity chamber during the flat-μ-fluidic experiment. Therefore the chamber was mounted on top of a temperature control unit, operated via a temperature controlled water bath. To stabilize the humidity during the experiment a moist piece of tissue is placed in a cavity close to the window. To resolve biological structures for instance bacteria with a diameter of ~1 μm within the μ-fluidic channels, it is mandatory to use a 63x long distance (LD) objective. Thus, the absolute height of the Teflon frame and window was made to be approximately 2 mm, owing to the working distance of 2.2 mm [Zeiss - Homepage].

The amplitude of the exited SAW was controlled by a high frequency (HF) generator (Advalytix AG) connected to the setup by the HF contact plugs. The HF generator was working in a frequency regime of ~100 - 200 MHz and with a maximum acoustic level output of ~30 dbm [Advalytix, 2004].

The generator was controllable by a computer software tool (LabView, provided from Advalytix AG). By this software tool, a working maximum acoustic level output of the HF generator p_{HFmax} could be defined in units of dbm and stepwise adjusted by a virtual slide controller in the regime between $p_{\mathrm{SAW}} = 0$ to p_{HFmax}.

The conversion from acoustic level, in units of dbm, to power, in units of mW, follows the relation,

$$p_{dbm} = 10^{(dbm/10)} \cdot 10^{-3}. \tag{4.25}$$

Therefore the maximum output acoustic level of 29 dbm corresponds to a SAW power of $p_{\mathrm{SAW}} = 800$ mW.

4.5 Flat-*μ*-Fluidic Experiments

With the previously described setup and the developed surface structuring and functionalization strategies first experiments with the flat-*μ*-fluidic were performed to verify their usability for *μ*-fluidic biological applications.

4.5.1 Shear-Rate $\partial u/\partial z$ of the Flat-*μ*-Fluidics Setup

To determine the maximum shear rate max($\partial u/\partial z$) achievable with the experimental setup, fluorescently labelled beads were tracked in order to estimate the maximum flow velocity max($u_{\mathrm{beads}}|_{p\mathrm{saw}}$) at the top position of the convex channel profile. From this value, a velocity profile for the half-cylindrical channel could be derived, according to Equation (4.24). Based on this profile, the shear rates $\partial u/\partial z$ could be calculated.

The nano-beads were dispersed into a *μ*-channel, prepared on a $LiNbO_3$ chip surface and movies of the streaming beads at the top position h_{max} in the half cylindrical channel were taken with a CCD camera connected to the upright microscope optics shown in Fig. 4.5.1.

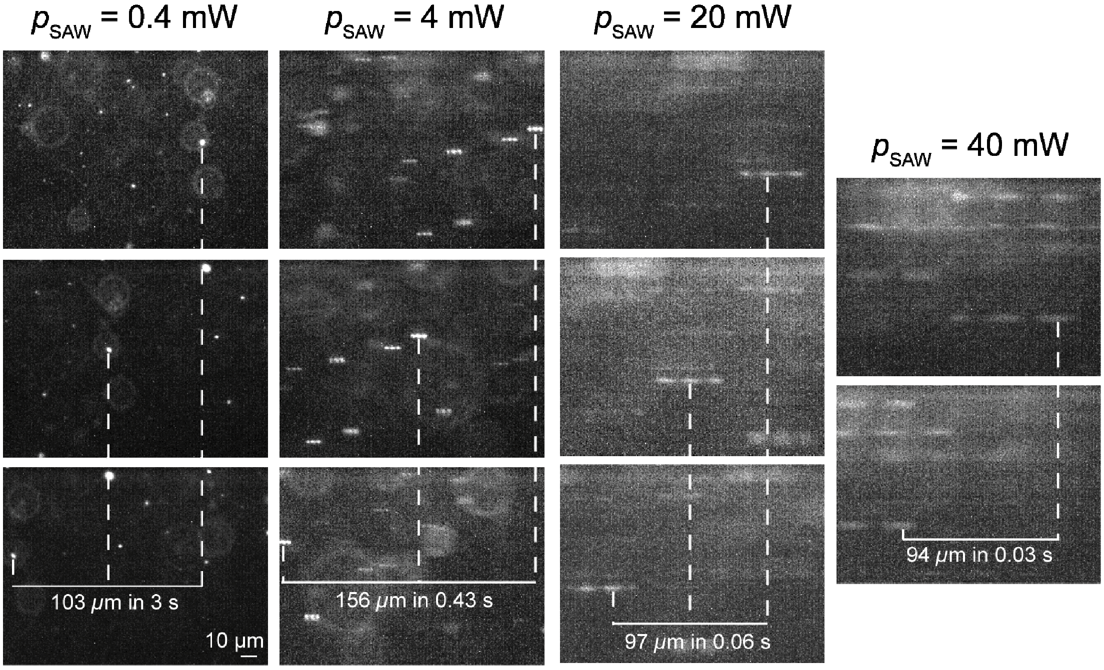

Fig. 4.5.1 Fluorescence images of particles (fluorescence nano-beads) taken at the power of the SAW p_{SAW} of 0.4 mW , 4 mW, 20 mW and 40 mW. For higher powers a tracking of particles was not possible.

From the acquired videos at different SAW power p_{SAW} the bead velocity could be calculated using

$$u_{bead}(h_{\max}) = \frac{d_{bead}}{t_{bead}}, \tag{4.26}$$

Here, d_{bead} was the traveled distance of a tracked bead and t_{bead} the elapsed time.

Fluorescence images of movies taken for the applied SAW power p_{SAW} = 0.4 mW, 4 mW, 20 mW and 40 mW are presented in Fig. 4.5.1 (the applied SAW power is labeled above the correspondent fluorescence image stack). For higher SAW powers no particles could be tracked anymore, owing to high the streaming velocities.

The calculated velocities for the tracked beads are presented in Fig. 4.5.2 and exhibit a linear dependency of u_{bead} from p_{SAW}.

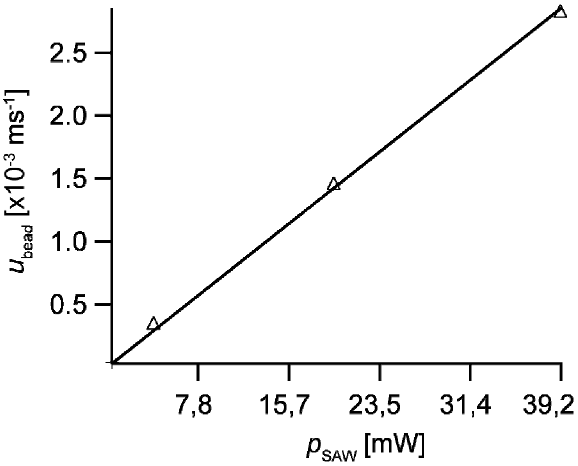

Fig. 4.5.2 Measured flow velocities of fluorescence beads at the top position of flat-μ-fluidic channels with a width of 1 mm at various SAW power p_{SAW}. The maximum velocity u_{max} for this channel geometry was determined from the measurements by linear extrapolation.

Therefore, a linear fit of the measured data points could be assumed and was extrapolated to obtain the maximum velocity u_{max}, achievable with the HF generator. This assumption is well justified as even at highest powers, one is still in the low Reynold's regime, hence no non-linearities need to be considered.

For the maximum power output of the HF generator of p_{SAW} = 800 mW a bead velocity of u_{800mW} = 0.09 m/s was extrapolated and a maximum shear rate of $\partial u_{800mW}/\partial z$ = 360 s^{-1} was calculated. Note that this value was obtained for the use of a single IDT. If the utilization of three IDT's aligned in one direction is assumed a shear rate of 3 x $\partial u_{800mW}/\partial z \approx$ 1080 s^{-1} could be achieved. This value is in regime of shear rates needed to detect detach events of bacteria [Thomas et al, 2004]

4.5.2 Preliminary Experiments with Bacteria

A first adhesion experiment was performed to prove bio-functional micro-domains formed by the molecule FL10man. To transfer an asymmetric lipid bilayer into the flat-μ-fluidic channel a position-selective LB-LS deposition was performed. First, a pure DOPC monolayer was LB-transferred into the channel as the lower leaflet and subsequently a mixed monolayer of DOPC incorporating 20 mol% FL10man was LS-transferred as the upper leaflet. To visualize the self-assembled micro-domains, a fluorescence lipid tracer was added into the spread lipid stock solution. The bacteria sample was taken from an overnight culture of a single clone of bacteria strain E.Coli HB101 (pPKl4). A single bacterium was isolated on a cell-culture plate and grown at 37°C in a culture medium. The cell density was determined to N = 2.2 x 10^9 cells/ml and diluted to a concentration of 1/10th for the following experiment. In Fig. 4.5.3, a series of overlaid fluorescence and phase contrast images is presented and showing bacteria moving over a previously transferred patterned membrane.

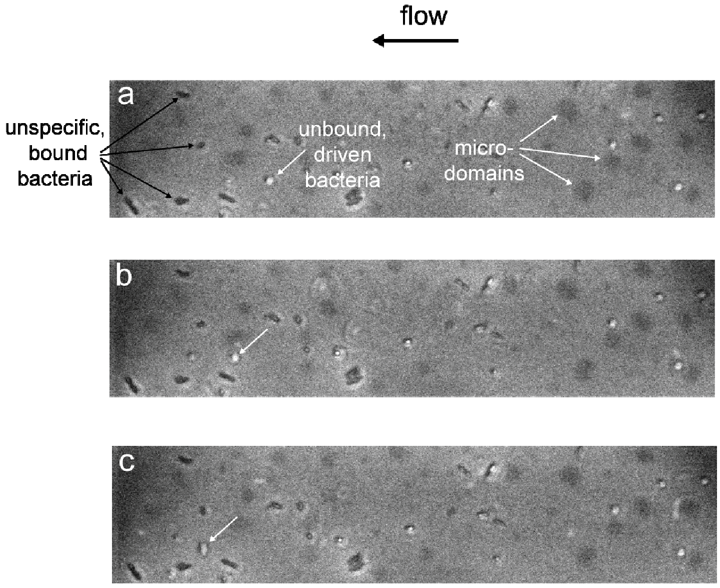

Fig. 4.5.3 Series of overlaid phase contrast and fluorescence images of bacteria driven over FL10man functionalized membrane in a μ-fluidic channel

The power of the SAW used in this experiment was approximately p_{SAW} = 8 mW which corresponds to a shear rate of $\partial u_{8\mathrm{mW}}/\partial z \approx 3\ \mathrm{s}^{-1}$. This shear rate was chosen below a critical rate for catch bond events, which is reported to be around 3 to 10 s^{-1}. With this experiment, it could be shown that bacteria can be streamed over a surface, bio-functionalized by a simple sugar head-group based on acoustic streaming.

5. Conclusion

This thesis presented the design of new model biological membranes that display well defined, highly ordered functional micro-/nano-domains towards the geometric regulation of cell adhesion. The formation of these micro-domains was achieved by utilizing unique properties of fully fluorinated lipid anchors that are perfectly phase separated at a wide mixing ratio, so that lipid monolayers incorporating these domains could be transferred from the air/water interface onto a planar substrate.

In Chapter 2, the structures and lateral correlations of micro-domains of FL17 molecules were investigated by the combination of various physical techniques. Fluorescence microscope images demonstrated that FL17 molecules form highly uniform micro-domains in fluid phospholipid matrices. In the first step the size of FL17 domains were determined by self-developed image analysis routine. However the quantitative determination of the cluster size by optical microscopy can be erroneous, since the characteristic length scale from Fast Fourier Transform and image analysis is close to the diffraction limit ($\langle d_{\mathrm{FL17}} \rangle = (0.33 \pm 0.08)\ \mu\mathrm{m}$). To overcome the resolution limit the grazing-incidents X-ray diffraction (GIXD) technique was used to determine the micro-domain size. In this series of experiments a unique analyzer crystal optics was used to gain a high angular resolution to resolve the micro-domain size of $\langle d_{\mathrm{FL17}} \rangle = (0.35 \pm 0.01)\ \mu\mathrm{m}$, indicating that each cluster consist of a single crystallite of FL17 molecules. Furthermore the two-dimensional reciprocal space maps imply that FL17 molecules take a hexagonal lattice (intra-molecular distance d_{FL17}^{mo} = 5.65 Å), keeping an upright orientation, even at low surface pressures. The fact that FL17 molecules form single crystalline, highly uniform micro-domains enables one to generally describe the lateral correlation of FL17 micro-domains as the problem of 2D colloidal interactions. To quantify the strength of the lateral correlation of micro-domains the radial distribution function was determined from the self-developed image analysis routine. The potential of mean force could be derived from the radial distribution function, taking all interactions of micro-domains into account The potential first minimum corresponds to the correlation distance of the micro-domains and verifies that micro-domains do not coalesce into bigger domains even at high molar fraction of FL17. This high repulsive potential of the fluorinated domains can be understood by taking into account the dipole moment of the CF_3-terminus. As a quantitatively measure of the potential strength, spring constants have been derived from a harmonic fit of the first minima position. At a high FL17 fraction (33 mol%) a periodic oscillation could be observed up to the distance of six times the micro-domain diameter, indicating significantly strong correlations between 2D colloidal particles formed by a self-assembling of organic molecules.

In Chapter 3, the influence of the molecular chemistry on the micro-domain structures and their lateral correlations was investigated by varying the length and number of fluorinated chains. First, it was found that the size of micro-domains was not influenced by increasing the number of chains. In contrast the change in the number of fluorocarbons from 10 to 17 had a dramatic influence on the micro-domain size, as well as on the lateral correlation: The domain size is reduced in the order of a magnitude according to a systematic increase in the number of fluorocarbons. Though it appeared counter-intuitive from the simple consideration of the line tension around fluorinated micro-domains this tendency could well be explained, by taking the height mismatch at the micro-domain boundary into account (equilibrium dipole model). The quantitative determination of all structural parameters enabled one to theoretically calculate the domain size of FL10, FL13 and FL17 showing an excellent agreement with our experimental results.

To add biofunctionalities to the micro-domains FL10 with a relatively simple monosaccharide (mannose) was used for the proof of principle. As predicted from the theoretical framework, a clear influence of the sugar head group on the domain size could be observed. As the fist test system, mouse macrophages that express mannose binding receptor were incubated on (a) a pure (and thus non-functional) phospholipids membrane and (b) a membrane displaying mannose micro-domains. On the membrane functionalized with mannose micro-domains, cells take spindle-like shape after 20 h, which is in a clear contrast to the cells on phospholipids membranes remaining spherical and non-active. This gives clear evidence that such molecular constructs can be used for the geometrical regulation of cell shape and activity.

In Chapter 4, it was demonstrated that the surface of a flat-μ-fluidics chip could be coated with a position selective deposition of asymmetric membranes functionalized with micro-domains. This was achieved by a self-developed protocol utilizing the combination of Langmuir-Blodgett and Langmuir-Schaeffer transfer. A small volume (7 μl), half-cylindrical water channels with convex profile could be prepared by photolithography on the chip surface. The velocity profile in this non-invasive μ-pumping system utilizing the principle of acoustic streaming could be modeled by finite elements model, confirming the laminar flow conditions near the middle of the channel. Measurements of the velocities of fluorescence nano-beads yield a quantitative calibration of the applied shear rate, which can be as high as 1000 s^{-1}. As preliminary attempt for the study of dynamic cell adhesion bacteria expressing mannose binding proteins were brought in contact with the functionalized flat-μ-fluidics chip, subjected to various shear fields.

The results obtained here demonstrated that highly uniform, strongly correlated micro-/nano-domains can be designed by using fully synthetic lipid anchors. Compared to commonly used raft models composed of complex lipid mixtures, this strategy has a large advantage to precisely adjust the domain size and inter-domain correlations by simple molecular chemistry. The successful stimulation of cell reactions, adding bio-functionalization to the domains, justified the approach to use them as membrane models in μ-fluidic applications. The here used flat-μ-fluidic technique offered high flexibility in the surface structuring by a self-developed transfer process together with the capability for the required shear rates even for bacterial adhesion experiments.

6. Outlook

During this work the anchor molecule FL10 was used as basis of the derived bio-functional molecule FL10man. The size of the functionalized micro-domains formed by this amphiphilic was determined to be about 1 μm. As these micro-domains shall be used as adhesive spots for bacteria or cells in adhesion experiments, this size is far too big. Therefore another molecule should be used as basis for bio-functional molecules like FL17. This molecule forms smaller self-assemblies with a mean diameter of ~ 350 nm as presented in Chapter 2. This dimension is more in the regime for raft-like adhesive spots. Another improvement should be a molecular redesign of the perfluorinated lipid with respect to the bio-functionalization. Agglomeration experiments with different synthetic glycolipids have shown that a binding of lectines to glycolipids incorporated in giant unilamellar vesicles take place after the introduction of >6 polyethylenglycerol (PEG) spacer units [Engel et al., 2003]. The introduction of polyethylenglycerol (PEG) spacer units between the fluorinated anchor section and the sugar head-group should therefore enhance the binding event.

In other fluidic experiments with the bacteria E.Coli a shear tension of 100 to 1000 pN was determined, necessary for attachment and detachment events [Thomson et al., 2004; Thomas, 2008]. This is correspondent to a shear rate of 100 to 1000 s^{-1} for a viscosity coefficient for water at 20°C $\eta_{20°C} = 1 \cdot 10^{-3}$ Pas. To cover this whole shear rate regime the use of multiple IDT's is necessary, as illustrated in Fig. 6.1, since the utilization of a single IDT led to a maximum share rate of 360 s^{-1}.

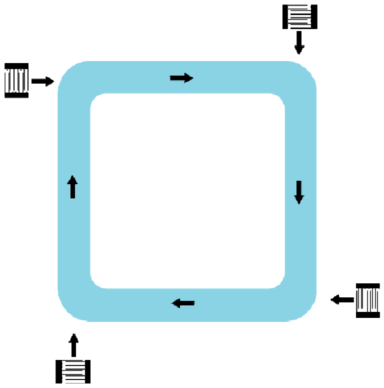

Fig. 6.1 A micro-fluidic setup, employing four IDT’s in parallel. The parallel use of multiple IDT's is possible since the damping rate of the generated longitudinal acoustic waves exceeds the streaming velocity of water.

The performed velocity measurements by tracking fluorescence beads in μ-fluidic channels were limited to SAW powers < 40 mW, owing to the insufficient frame rates of commonly used CCD cameras. In Fig. 6.2 an optical grid technique is depicted, which allows to measure high velocities in defined μ-fluidic channels using a frequency analysis [Sitharan, 2008].

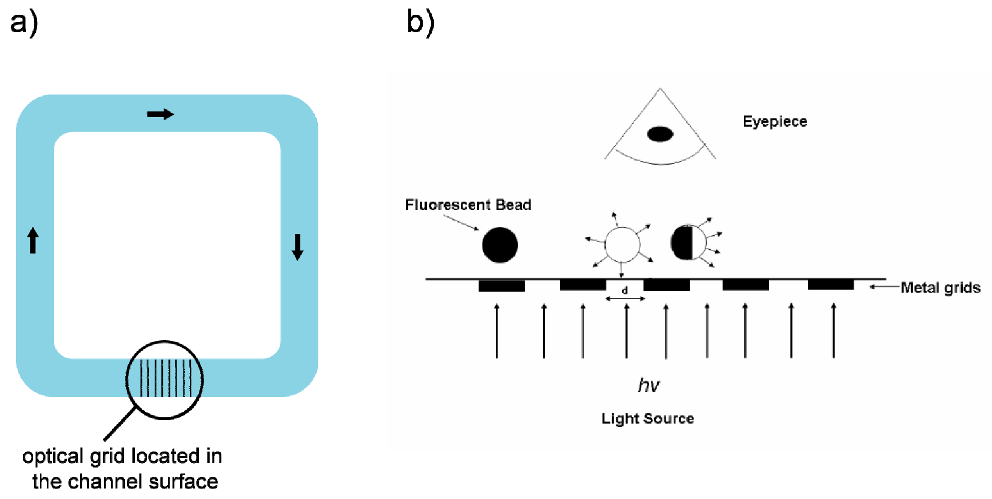

Fig. 6.2 (a) Optical grid applied at the surface of a μ-fluidic channel. (b) A bead is agitated over the grid and is illuminated from underneath the transparent surface (from [Sitharan, 2008]). The particle is tracked and the recorded illumination periodicity is frequency analyzed to determine the flow velocity

With this technique the calibration of shear rates for high streaming velocities in flat-μ-fluidic channels, utilizing multiple IDT's could be done.

A. Appendix

A.1 Lipid Chemical Structure

The chemical structures of the matrix lipid ,2-dioleo-*sn*-glycero-3-phosphocholine (DOPC) and the fluorescence dye tracers 1,2-dihexadecanoyl-sn-glycero-3-phosphoethanolamine triethylammonium salt (Texas Red-PE) are presented in Fig. A.1.

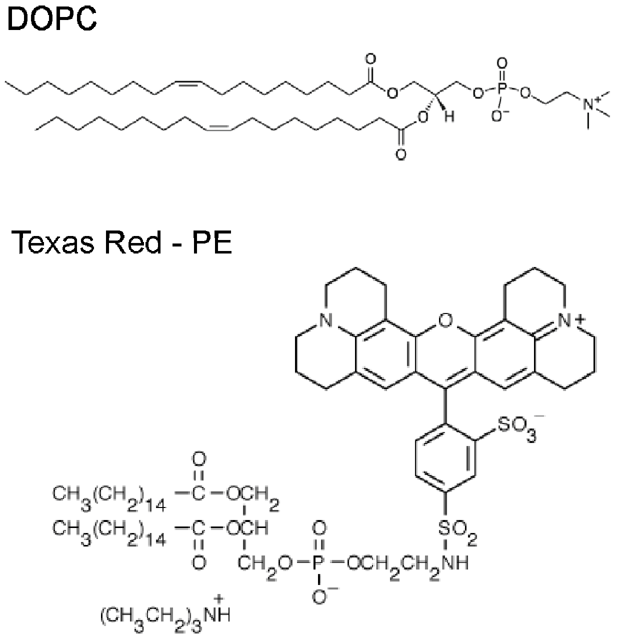

Fig. A.1 Chemical structures of the lipid DOPC (Avanti Polar Lipids) and the fluorescence tracer Texas-Red-PE (Invitrogen)

A.2 Grazing Incidents X-Ray Diffraction Measurements on Mixed Monolayers at Air/Water Interface

To obtain information about the molecular chain-chain correlation of synthetic fluorinated molecules in mixed monolayers, grazing-incidence X-ray diffraction (GIXD) measurements at the air/water interface were performed at various surface pressures π. Mixed monolayers with a molar fraction $\chi = 50$ mol% for all fluorinated molecules presented in Chapter 1.1 were spread at the air/water interface onto a film balance placed at the sample stage of the beam-line as reported in Chapter 1.5.1 The following presentation of GIXD measurement results follows the same structure as used in Chapter 3.

A.2.1 Modification in Chain Length - FL10, FL13, FL17

The integrated intensities for the fluorinated molecules with varying chain length is presented in Fig. A.2.1(upper row).

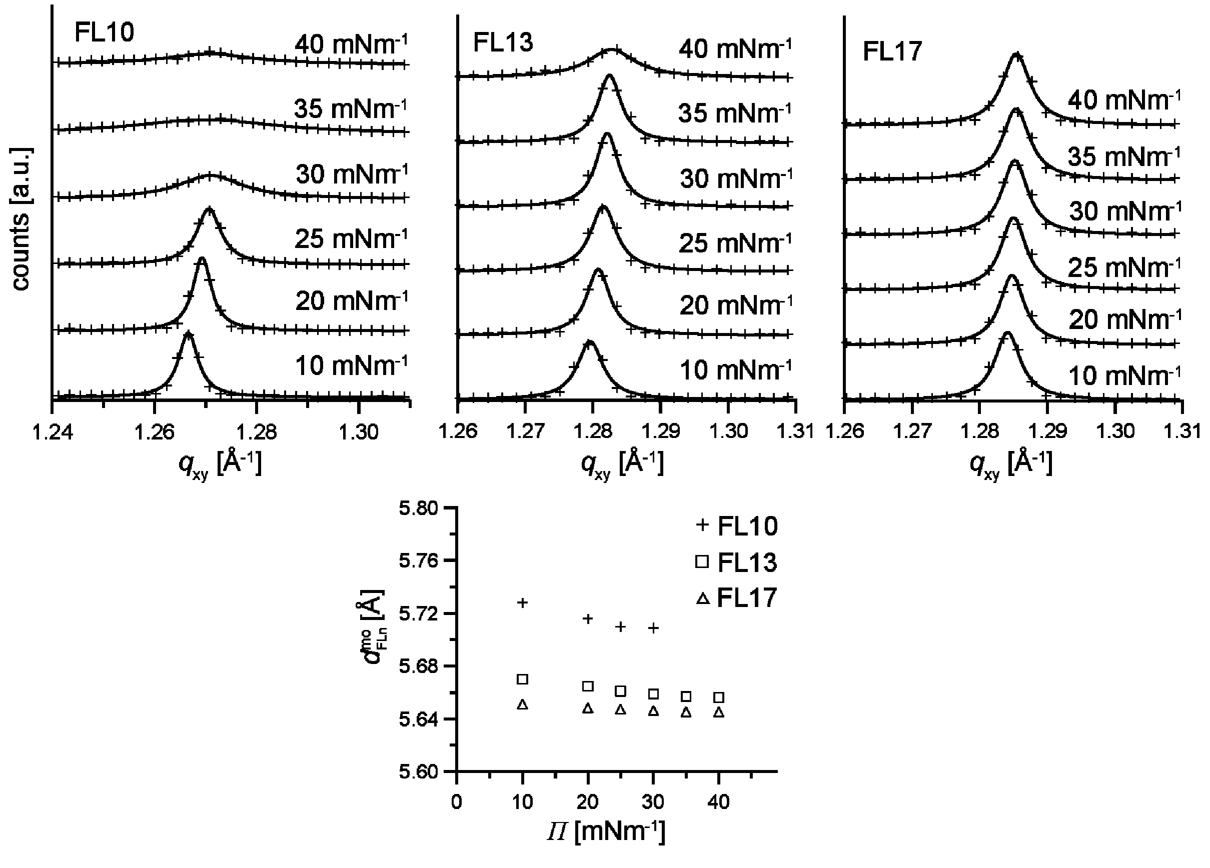

Fig. A.2.1 (upper row) Integrated intensities for the GIXD measurements of mixed monolayers, incorporating FL10, FL13 and Fl17, at various surface pressures *Π*. While for FL17 the chain-chain correlation is constant beyond a pressure of *Π* = 40mN^{-1}, the chain packing for FL13 vanishes below Π = 40 mNm^{-1} respectively Π = 25 mNm^{-1} for FL10. (lower row) The chain–chain distance vs. the surface pressure.

While the initial chain packing for FL17 remains constant up to a surface pressure of Π > 40 mNm^{-1} the hexagonal arrangement vanishes beyond a critical pressure of Π_{FL13} = 40 mNm^{-1} for FL13 and Π_{FL10} = 30 mNm^{-1} for FL10 respectively. This loss in the chain-chain correlation, in particular for the molecule FL10 coincides with results of fluorescence microscopy for the domain break-down at a transfer pressures Π_{T} > 20 mNm^{-1}, as reported in Chapter 3.4.1.

The correlation chain-chain distance for FL10, FL13 and FL17 with respect to the surface pressure Π is presented in Fig. A.2.1(lower row), calculated from the maximum peak position of the GIXD measurements. Here, the fact that for FL17 the peak position does not shift measurably, and only a slight shift for FL10 ($\Delta d_{FL10}^{mo} = 0.02$ Å) is observable should be noted. This indicates that an elongation leads to a stabilization of the micro-domains.

Fluorinated Molecule	q_{xy} [Å^{-1}]	correl. length [Å]	d_{FLn}^{mo} [Å]
FL10	1.267 ± 0.001	4.96 ± 0.01	5.73 ± 0.01
FL13	1.280 ± 0.001	4.91 ± 0.01	5.67 ± 0.01
FL17	1.284 ± 0.001	4.89 ± 0.01	5.65 ± 0.01

Tab. A.2.1 The Obtained q-values, the calculated correlation length and corresponding chain-chain distance d_{FLn}^{mo} for FL10, FL13 and FL17 at a surface pressure of π = 10 mNm^{-1}.

The calculated correlation lengths according to Equation (1.9) and the correspondent chain-chain distance d_{FLn}^{mo} at the surface pressure of Π = 10mNm^{-1} is presented in Table A.2.1. These values for the measured fluorinated molecules coincide well with X-ray measurements on fluorinated alcohols at the air water interface [Barton et al., 1991].

A.2.2 Modification in Chain Number - FL10, FT10

The comparison of the molecules FL10 and FT10 shows an identical surface pressure dependency in the molecular arrangement.

As already observed for FL10 the chain-chain correlation of FT10 within the fluorinated micro-domains vanishes at a surface pressure of Π_{FT10} = 30 mNm^{-1}, presented in Fig. A.2.2(upper row). Furthermore a good agreement in the calculated chain-chain distances d_{Fn10}^{mo} for both molecules could be found (for FT10 d_{FT10}^{mo} = (5.72 ± 0.01) Å at Π = 10 mNm^{-1}).

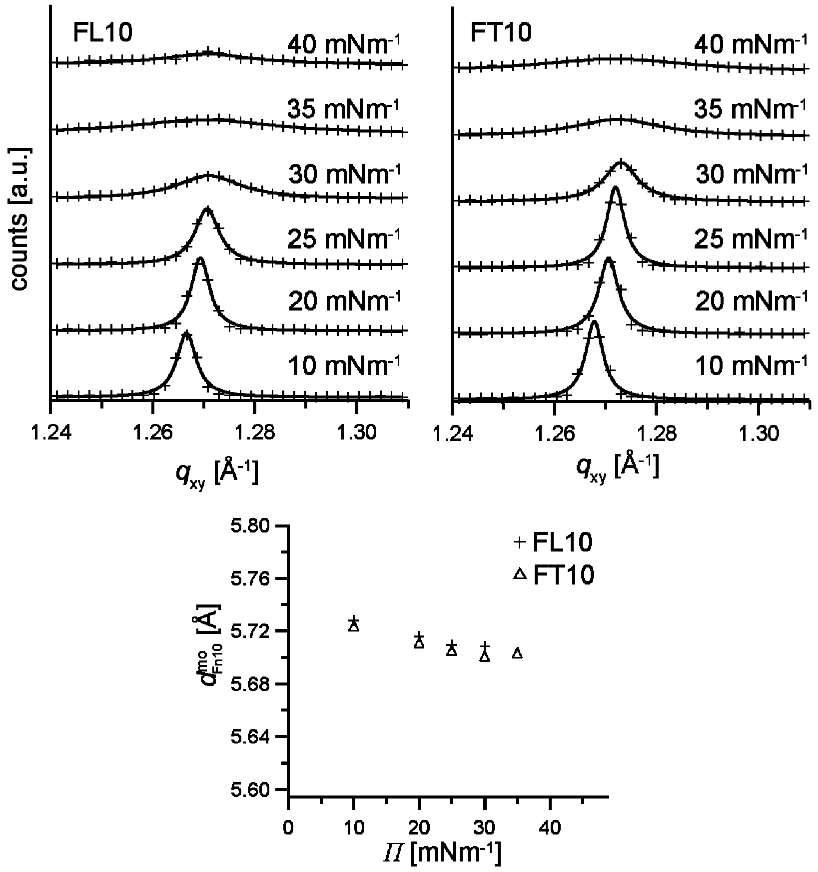

Fig. A.2.2 (upper row) Integrated intensities of GIXD measurements of mixed monolayer incorporating FL10 and FT10 at various surface pressures *Π*. Both molecules show a comparable behavior. (lower row) The chain–chain distance vs. the surface pressure.

A.2.3 Modification in Head-Group - FL10, FL10man

For the bio-functional molecule FL10man the modification in the head-group of the anchor molecule FL10 with a sugar moiety leads to a significant change in the stability of the chain-chain packing between the fluorinated molecules within the self-assemblies. This was owing to the additional head-head interactions of the more polar mannose in contrast to the simple OH head-group of FL10.

In Fig. A.2.3(upper row) the integrated diffraction intensities are presented for FL10 and FL10man for comparison.

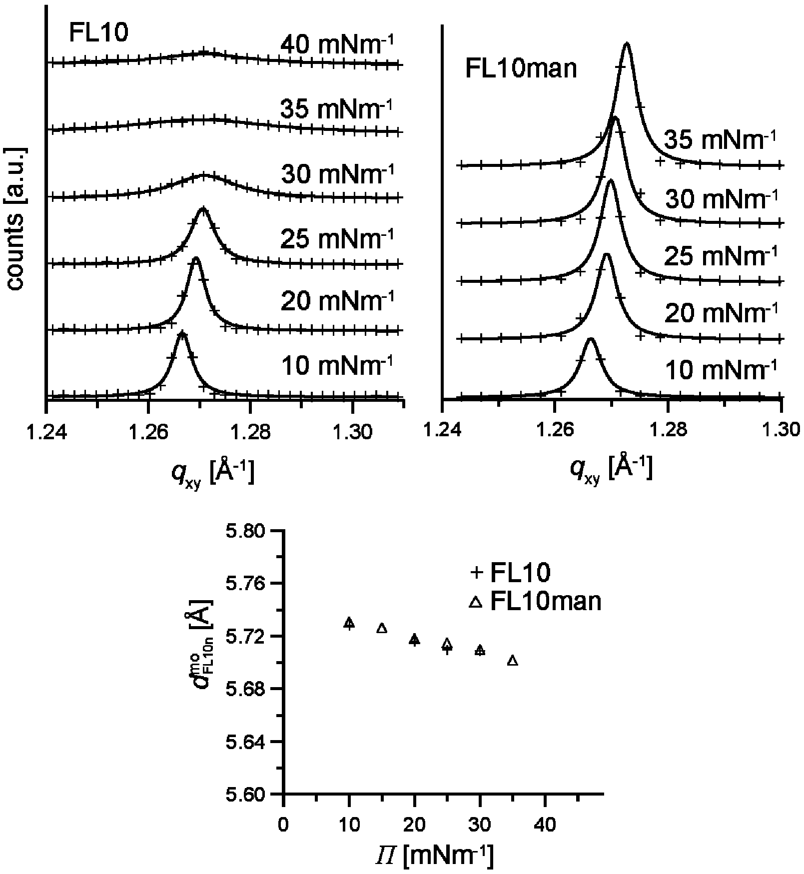

Fig. A.2.3 (upper row) Integrated diffraction intensities for FL10 and FL10man at various surface pressures *Π*. (lower row) Shift in the peak position d_{mo} during monolayer compression.

While the chain-chain ordering breaks up for FL10 beyond a critical surface pressure $\Pi > 20\ \mathrm{mNm}^{-1}$ the hexagonal ordering of FL10man was still resolvable at $\Pi > 35\ \mathrm{mNm}^{-1}$.

In contrast to the stabilization effect for the hexagonal packing, no significant change in the molecular distance d_{FL10n} could be observed. For FL10man the same peak position ($d^{mo}_{FL10man}$ = (5.73 ± 0.01) Å at $\Pi = 10\ \mathrm{mNm}^{-1}$) is obtained as for FL10. This suggests that the de-mixing of the fluorinated molecules and therefore the formation of micro-domains is dominated by the unique property of the fluorocarbon chains.

A.3 Small Angle (SAXS) and Wide Angle (WAXS) X-Ray Scattering of Fluorinated Molecule/Lipid Dispersions

Small angle X-Ray (SAXS) and wide angle X-ray (WAXS) measurements of bilayer stacks composed of fluorinated molecules were performed at the Hamburger Synchrotronstrahlungslabor (HASYLAB, Hamburg, Germany) to determine the inter lamella distances formed by fluorinated molecules and thus the molecular height h^{mo}, their electron density profile, as well as the lateral molecular spacing.

In Fig. A.3.1 the measurement setup of the HASYLAB is schematically depicted.

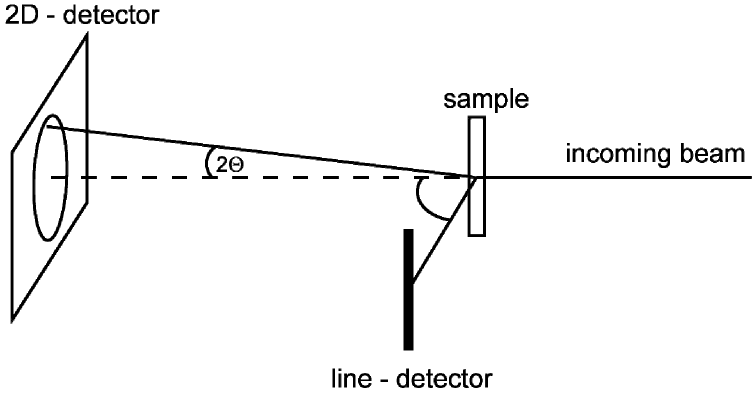

Fig. A.3.1 SAXS/WAXS experimental setup of the beamline A2 at the HASYLAB.

The incoming beam impinges on the sample and gets scattered according to Bragg's law at an angle 2θ with respect to the direct beam. The small angle and wide angle scattering is simultaneously recorded with a 2D detector in case of SAXS and with a line detector in case of WAXS.

The detectors were previously calibrated by a reference samples Rat Tendon Tail (RTT) for SAXS and Tripalmetin for WAXS. The resolution of the SAXS corresponds to a lattice spacing of ~4 to 10 nm and WAXS is suited for the investigation of in-plane correlations in the range of few nm down to 1 Å. As samples, quartz capillaries (Hilgenberg, Malsfeld, Germany) filled with pure molecules or lipids, respectively 1:1 molecule/lipids dispersions (concentration ~20 wt% water) were used.

SAXS results for the fluorinated molecules with varying chain length are presented in Fig. A.3.2 , wherefrom a fitted electron density profile could be extracted, as presented in the inset of Fig. A.3.2.

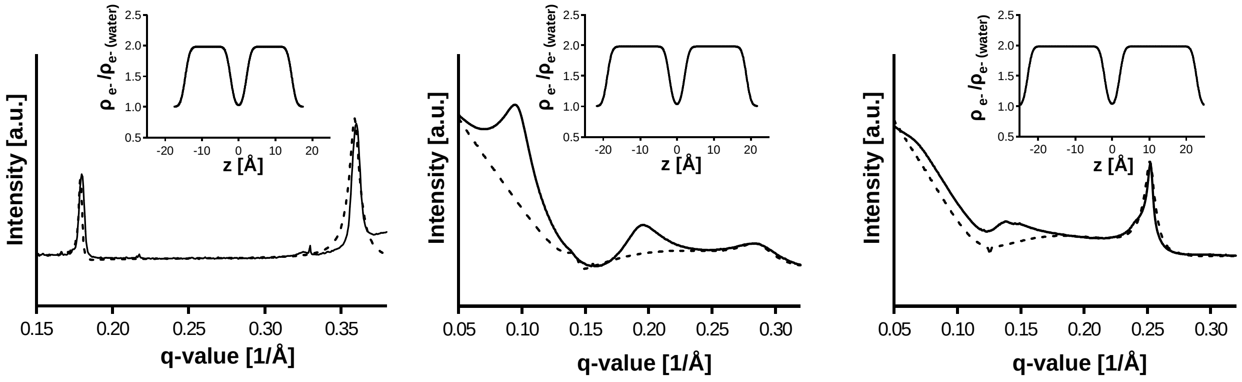

Fig. A.3.2 SAXS results for the molecules FL10(left), FL13(middle) and FL17(right). As an inset the electron density profile of the molecules according to the fitted SAXS profile (dashed line) is presented.

From electron density profiles fitted by a self-made routine, the heights for the molecules FL10 h_{FL10}^{mo} = (12.8 ± 0.5) Å, FL13 h_{FL13}^{mo} = (16.8 ± 0.5) Å and FL17 h_{FL17}^{mo} = (21.9 ± 0.5) Å could be obtained, verifying the assumption of a CF_2-CF_2 spacing of 1.294 Å reported by Bunn & Howells [Bunn & Howells, 1954]. The values for the molecular height were used for the theoretically domain size calculation, performed in Chapter 3.4.6.

WAXS measurements performed for the molecules are presented in Fig. A.3.3 and show a single peak, suggesting a hexagonal packing for the molecules.

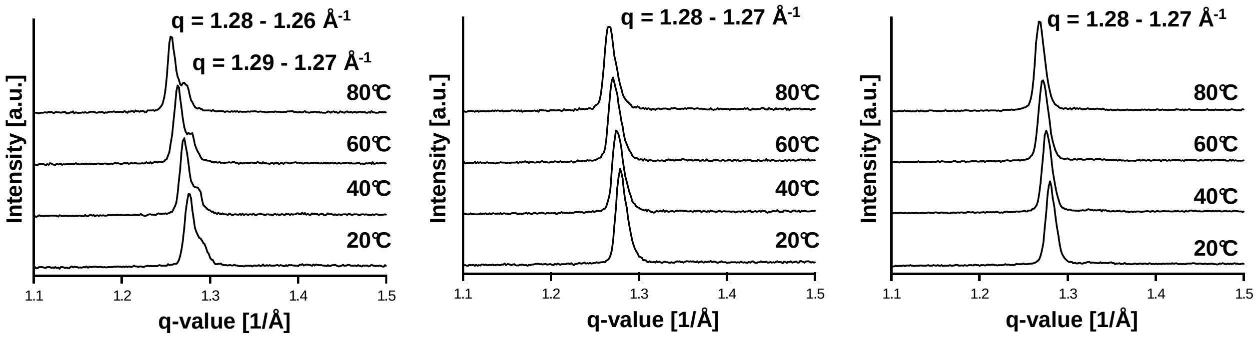

Fig. A.3.3 WAXS results for the molecules FL10(left), FL13(middle) and FL17(right).

The peak positions in *q*-space for all molecules coincide with the results of the GIXD measurements, as can be seen in Table 3.1.

[$Å^{-1}$]	FL10	FL13	FL17
GIXD	1.27 ± 0.01	1.28 ± 0.01	1.28± 0.01
WAXS	1.27 ± 0.01	1.28 ± 0.01	1.28± 0.01

Tab. A.3.1 Comparison between WAXS (at T = 20°C) and GIXD (at π = 10 mNm^{-1}) results for FL10, FL13 and FL17.

A.4 Image Processing of Mixed Monolayers

Here, for each fluorinated molecule the results of the performed image processing, i.e. the mean diameter <*d*> and distance distribution *p*(*r*) as well as radial distribution function *g*(*r*) and potential of mean force–*ßw*(*r*) is presented.

A.4.1 Size Distribution

FL10

The size distribution for mixed monolayers incorporating FL10 micro-domains at molar fractions χ_{FL10} = 33, 20 and 10 mol% is presented in Fig. A.4.1(upper row).

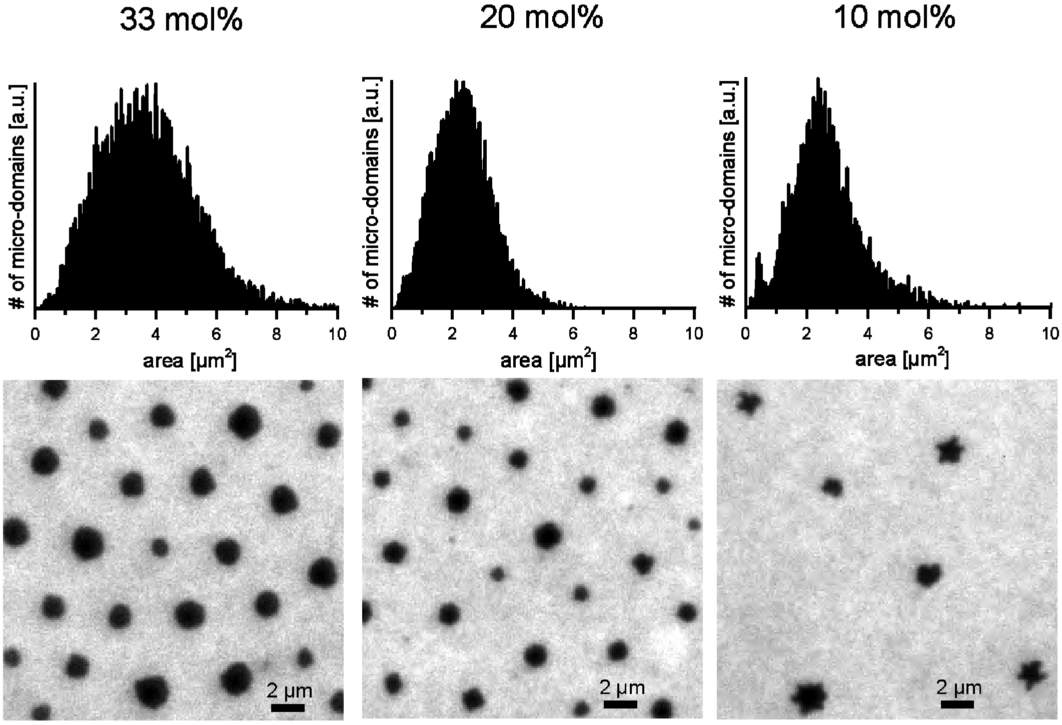

Fig. A.4.1 In the upper row, the size histograms of FL10 micro-domains for the molar fractions χ_{FL10} = 33, 20 and 10 mol% is presented, while the lower row shows the correspondent fluorescence images. Below a critical threshold of fluorinated molecules no formation of circular micro-domains could be observed for FL10, owing to line tension induced instability.

At a molar fraction of χ_{FL10} = 10 mol%, owing to an instability in the domain formation, the micro-domains take no circular shape, see Fig. A.4.1(lower row), therefore no diameter could be calculated, assuming a circular shape. For mixed monolayers with higher molar fractions a mean diameter was determined by the assumption of a circular disc for a micro-domain to $<d_{FL10}>_{33mol\%} = (2.1 \pm 0.34)\ \mu m$ and $<d_{FL10}>_{20mol\%} = (1.68 \pm 0.25)\ \mu m$.

FL13

Mixed monolayers incorporating FL13 at a molar fraction of χ_{FL13} = 33, 20, 10 and 5 mol% have been transferred and processed, shown in Fig. A.4.2.

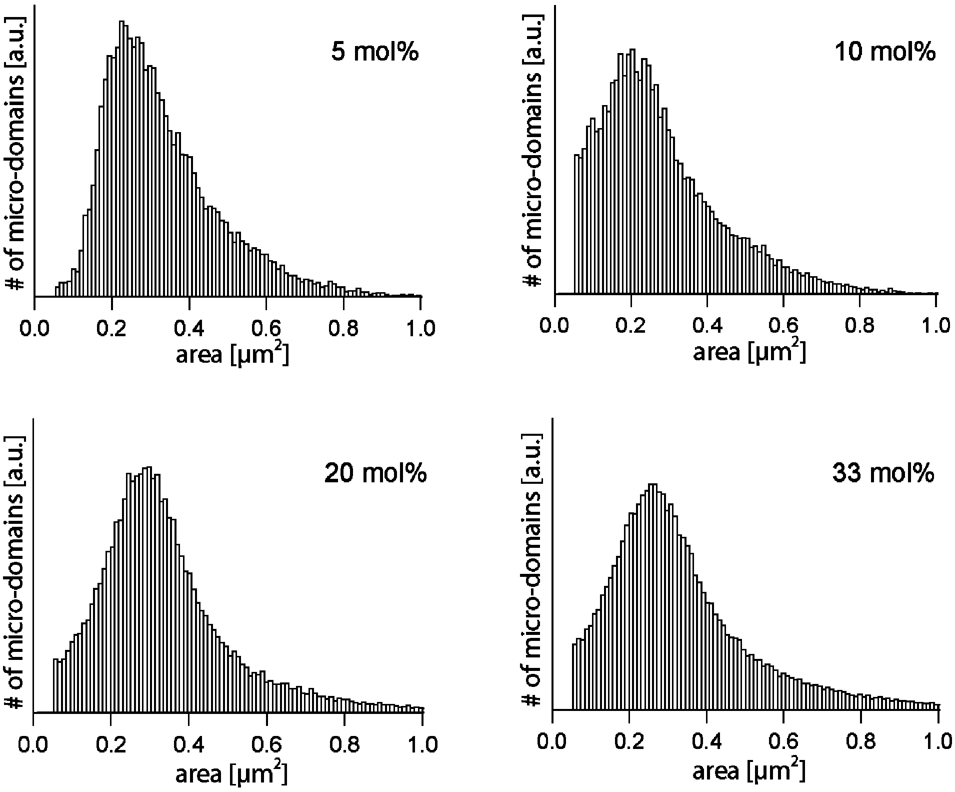

Fig. A.4.2 Size histograms of FL13 micro-domains for the molar fractions χ_{FL13} = 33, 20, 10 and 5 mol%

Mean diameters of $<d_{FL13}>_{33mol\%} = (0.57 \pm 0.07)\ \mu m$, $<d_{FL13}>_{20mol\%} = (0.6 \pm 0.07)\ \mu m$, $<d_{FL13}>_{10mol\%} = (0.5 \pm 0.08)\ \mu m$ and $<d_{FL13}>_{5mol\%} = (0.57 \pm 0.08)\ \mu m$ were determined according to the corresponding molar fractions.

FL17

Mixed monolayers with χ_{FL17} = 33, 20, 10 and 5 mol% have been transferred and processed for FL17, shown in Fig. A.4.3.

The size of FL17 micro-domains is close to the optical resolution of fluorescence microscopy, therefore a cut-off minimum size for the detected micro-domains was defined (A_{min} = 4pxl). A detected object below this value was not identified as a micro-domain for further analysis. The mean diameters $<d_{FL17}>_{33mol\%}$ = (0.30 ± 0.1) μm, $<d_{FL17}>_{20mol\%}$ = (0.33 ± 0.1) μm, $<d_{FL17}>_{10mol\%}$ = (0.36 ± 0.05) μm and $<d_{FL17}>_{5mol\%}$ = (0.34 ± 0.05) μm have been determined.

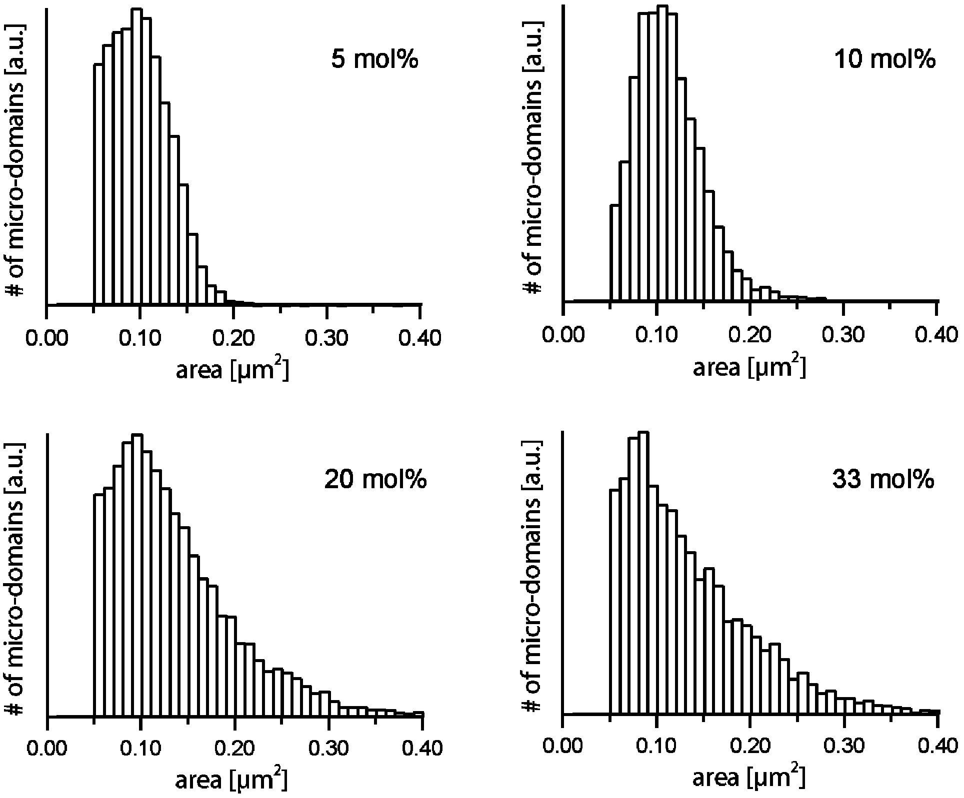

Fig. A.4.3 Size histograms of FL17 micro-domains for the molar fractions χ_{FL17} = 33, 20, 10 and 5 mol%

FL10man

In contrast to FL10, micro-domains formed by FL10man could be observed even at a molar fraction <10 mol%. Thus, monolayers at χ_{FL10man} = 5, 10 and 33 mol% have been transferred, shown in Fig. A.4.4.

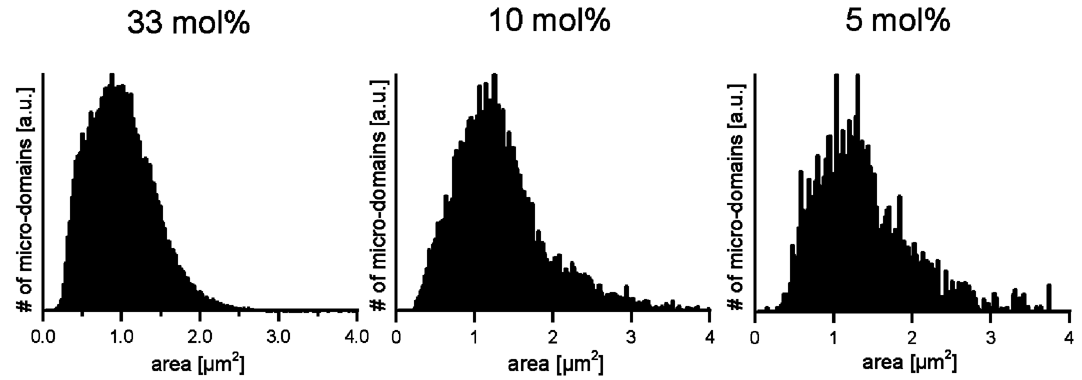

Fig. A.4.4 Size histograms of FL10man monolayers at the molar fractions χ_{FL10man} = 33, 20 and 5 mol%

Micro-domains in all transferred monolayers showed circular shape, so that the mean diameters $<d_{\text{FL10man}}>_{\text{33mol\%}}$ = (1.09 ± 0.19) μm, $<d_{\text{FL10man}}>_{\text{10mol\%}}$ = (1.2 ± 0.19) μm and $<d_{\text{FL10man}}>_{\text{5mol\%}}$ = (1.19 ± 0.24) μm could be calculated.

FT10

For monolayers incorporating FT10 at χ_{FT10} = 5, 10 and 33 mol% have been transferred, shown in Fig. A.4.5.

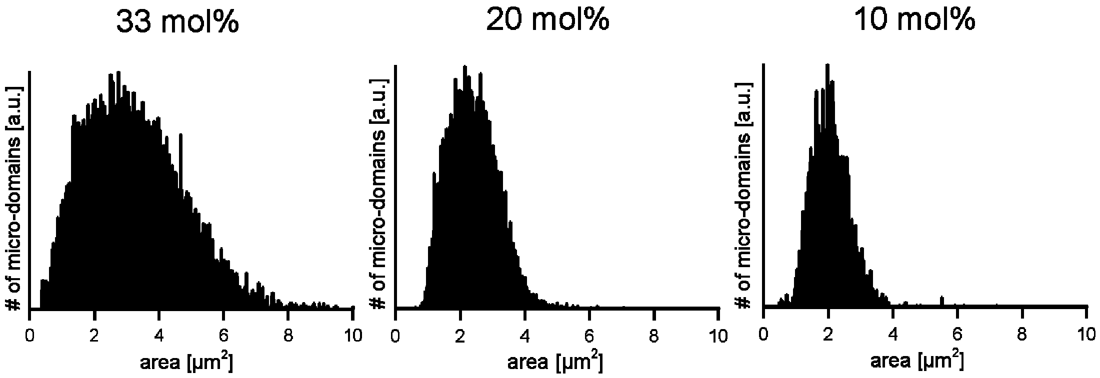

Fig. A.4.5 Size histograms of FT10 monolayers at the molar fractions χ_{FT10} = 33, 20 and 10 mol%

The mean diameters $<d_{FT10}>_{33mol\%}$ = (1.92 ± 0.37) μm, $<d_{FT10}>_{20mol\%}$ = (1.70 ± 0.21) μm and $<d_{FT10}>_{10mol\%}$ = (1.57 ± 0.33) μm have been determined.

A.4.2 Mean Diameter Distribution <*d*>

For all fluorinated compounds the mean diameters $<d>_\chi$ are plotted versus the corresponding molar fraction and is presented in Fig. A.4.6.

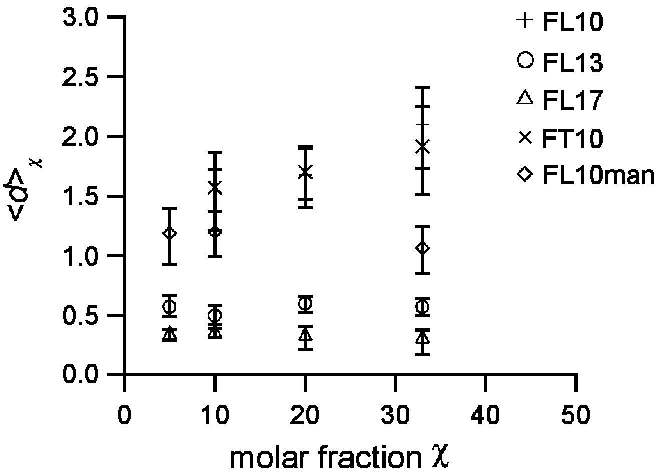

Fig. A.4.6 Mean diameter $<d>_\chi$ for all fluorinated molecules vs. the molar fraction χ

Since the diameters $<d>_\chi$ for the corresponding fluorinated molecules are constant in respect to the molar fraction χ a mean diameter for all mixing ratios could be determined to $<d_{FL10}>$ = (1.88 ± 0.29) μm, $<d_{FL13}>$ = (0.56 ± 0.08) μm, $<d_{FL17}>$ = (0.33 ± 0.08) μm, $<d_{FL10man}>$ = (1.16 ± 0.2) μm and $<d_{FT10}>$ = (1.73 ± 0.3) μm.

A.4.3 Nearest-Neighbour Distance Distribution *p*(r)

From the center-to-center distance between detected micro-domains, obtained from the image processing, a distance distribution *p*(*r*) could be determined. The distribution is presented for all fluorinated molecules and for all molar fractions vs. the normalized distance *r*/<*d*>, where <*d*> is the mean diameter determined from the size distributions.

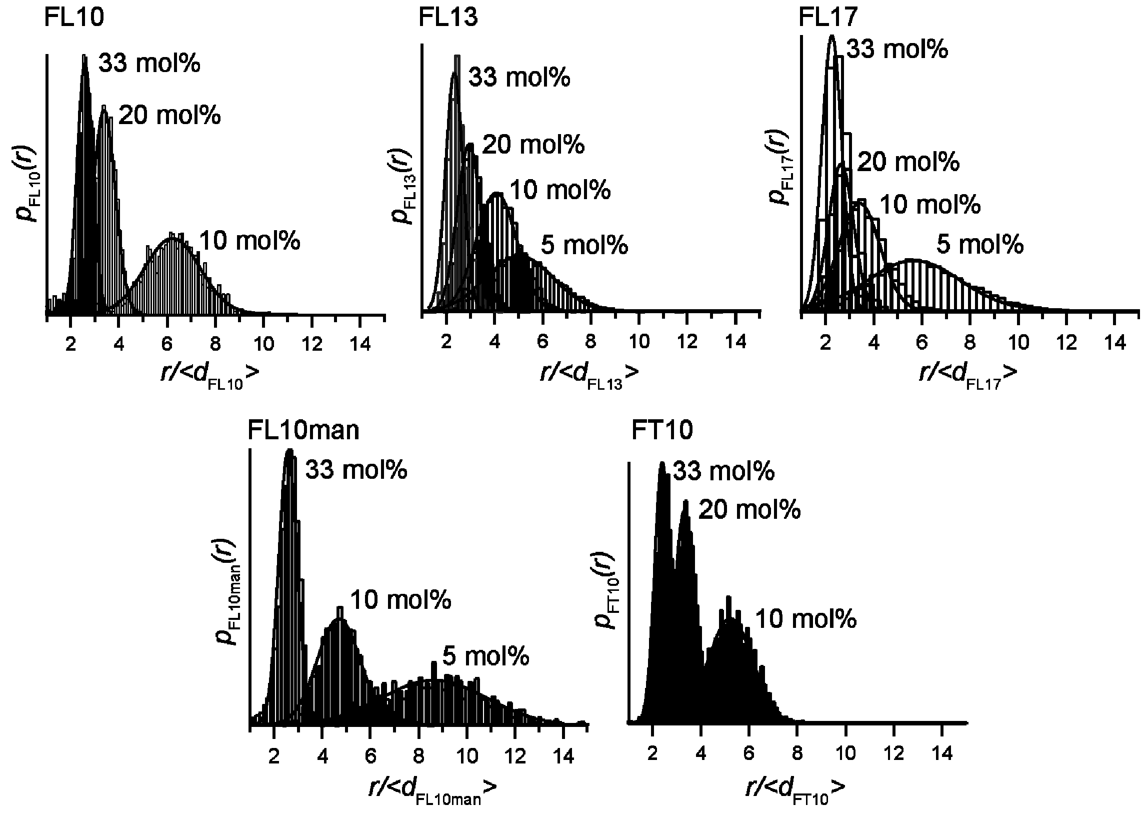

Fig. A.4.7 Nearest neighbor distance distribution $p(r)$ vs. the normalized distance $r/<d>$ whereby $<d>$ is the mean distance determined by optical analysis.

A.4.4 Mean Distance $<r>_\chi/<d>$

The normalized mean distance $<r>_\chi/<d>$ is presented in Fig A.4.8 versus the molar fraction χ.

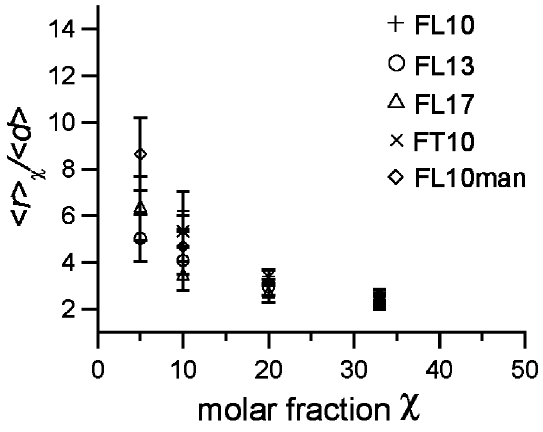

Fig. A.4.8 The normalized mean distance $<r>_\chi/<d>$ for all fluorinated molecules vs. the molar fraction χ

The normalized mean distance provides, that for all fluorinated compounds a minimum distance of about 2.5 times the corresponding mean diameter <*d*> is preserved at a molar fraction of χ = 33 mol%. This suggests the presence of a repulsive interaction between the micro-domains, owing to a resulting dipole-moment.

A.4.5. Radial Distribution Function *g*(*r*)

To obtain information about a long-range ordering of micro-domains, owing to the repulsive interaction and the influence of various mixing rations of fluorinated molecules within the monolayers, the radial distribution function *g*(*r*) was determined, according to the procedure reported in 1.4.2. For all transferred monolayers incorporating fluorinated molecules at different molar fractions *g*(*r*) is shown in Fig. A.4.9.

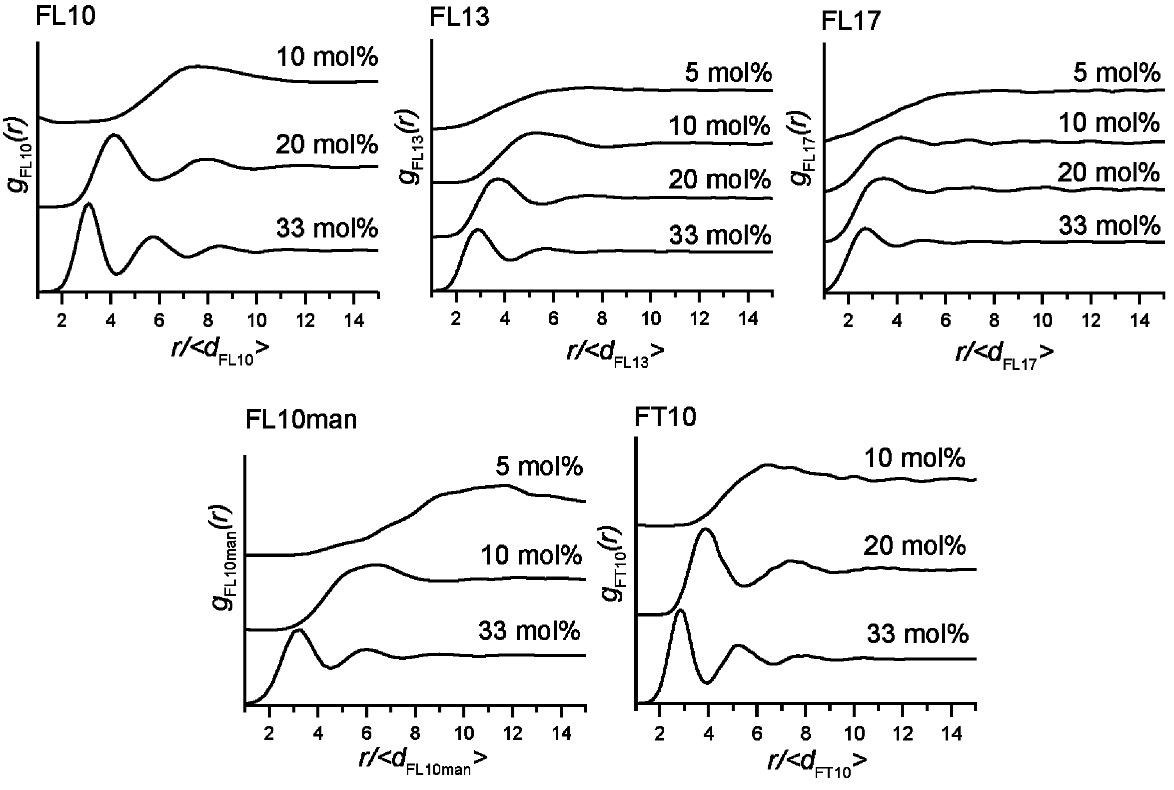

Fig. A.4.9 Radial distribution *g*(r) vs. the normalized distance *r*/<*d*>

The radial distribution function for all fluorinated domains is normalized as the nearest neighbor distribution, by the corresponding mean micro-domain diameter <*d*>.

Again a minimum distance between micro-domains even at high molar fractions could be observed. Therefore no evidence of a coalescence of micro-domains even at high mixing ratios could be observed.

A.4.6 The Potential of Mean Force –ß*w*(*r*)

To quantify the interaction of the fluorinated domains within the quasi hexagonal lattice, a potential of mean force was calculated according the inverse work theorem, presented in Chapter 1.4.3. The calculated potential for all radial distribution functions is shown in Fig. A.4.10.

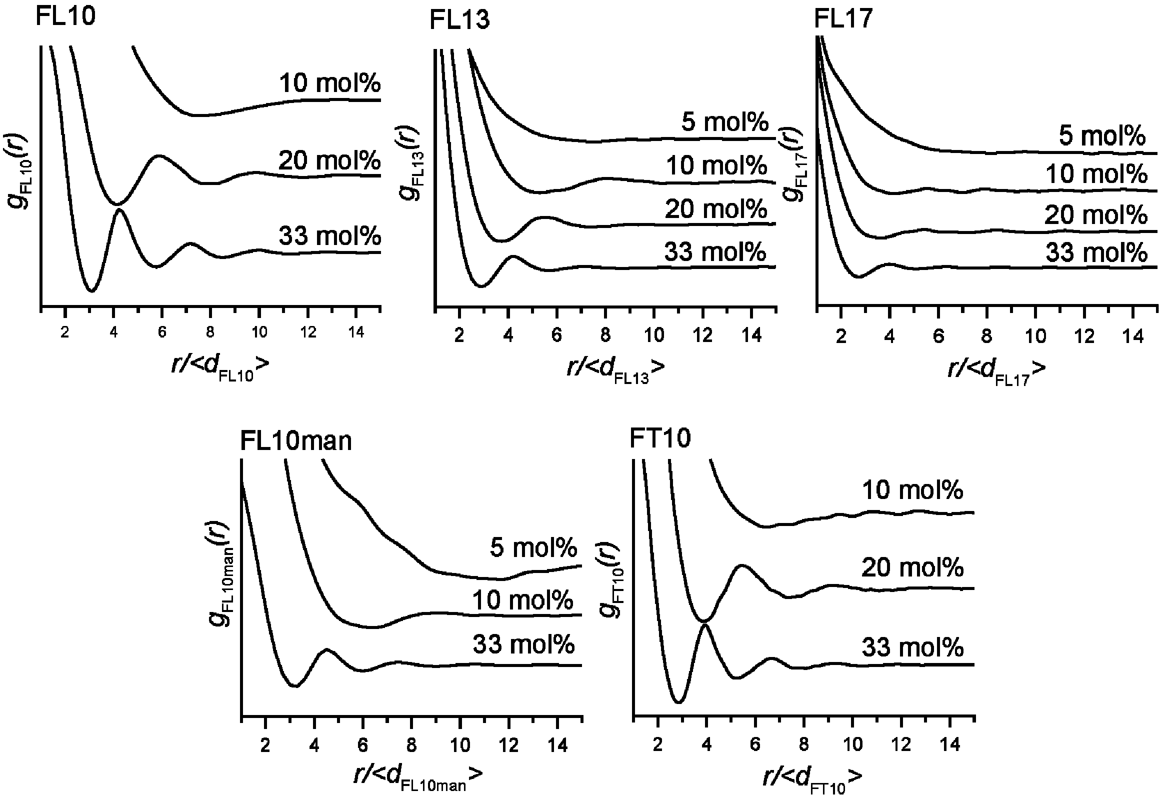

Fig. A.4.10 Potential of mean force -ß*w*(r) vs. the normalized distance *r*/<*d*>

The interaction potentials show a narrowing and deepening of the first potential minimum for an increasing molar fraction of fluorinated molecules and thus of the density of micro-domains.

A.5 Micro-Domain Shape Instability of FL10

An explanation for changes in shape of FL10 domains, compared to the circular appearance at high molar fractions, can be derived by the concept of the *“equilibrium shape model”* proposed by McConnell [McConnell, 1991].

A.5.1 Instability in molar fraction

In fluorescence images of mixed monolayer incorporating FL10 at a molar fraction <10 mol%, no circular but larger, bulkier micro-domains could be observed, as presented in Chapter 3.4.1. One possible explanation for this behavior could be a missing dipole-dipole interaction between these bigger FL10 domain agglomerations during the evaporation phase.

According to McConnell, a dipole-dipole interaction between domain agglomerations has to be taken into account in the free energy of an equilibrium shape for a micro-domain, if one or more domain agglomerations are in between the dipole potential of another domain.

The mean distance between the agglomerates at low molar fractions of FL10 seems beyond the range of the potential dipole-dipole interaction. For the domain agglomerations formed during the equilibration period no such dipole-dipole interaction can take place.

A.5.2 Compression instability

In A.2.1 it could be seen that the chain-chain ordering of FL10 micro-domains breaks up at the same surface pressure as the optically observable micro-domains collapsed (see Chapter 3.4.1). One possible explanation for these phenomena could also be provided by the “*equilibrium shape model*”. Theoretical calculations of the equilibrium diameter show that changes in the surrounding dipole moment density difference Δm have a drastic impact on the equilibrium domain diameter of FL10, as demonstrated in Fig. A.5.

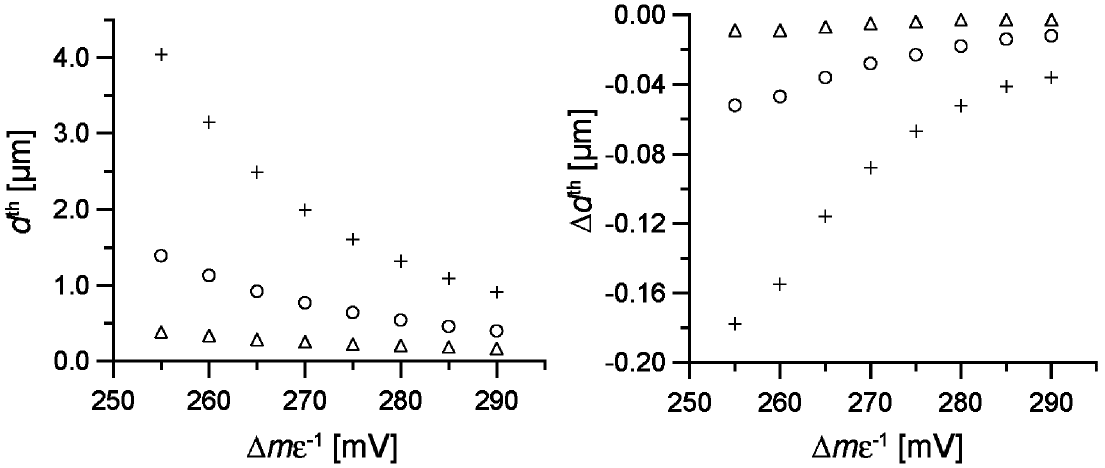

Fig. A.5 Calculated diameter $<d>_{th}$ and differential $<\Delta d>_{th}$ dependency from molecular dipole density difference

A small increase in *Δm* causes a drastic reduction in the domain size for the molecule FL10, in contrast to FL13 and especially to FL17. Thus FL17 micro-domains remain in their circular shape until the critical monolayer pressure of DOPC monolayer, while FL13 micro-domains collapse close before and FL10 micro-domains already at medium surface pressures.

Since the GIXD measurements in Appendix A.2 verified that the micro-domains of FL10 are slightly compressible in contrast to the micro-domains formed by FL17 their dipole density, and therefore the dipole density difference *Δm* could be also changed during the compression.

A.6 Piezoelectric Material Parameter and Damping Coefficient for Acoustic Waves in Water

Material parameters for various piezoelectric materials are presented in Table A.6.1.

Material	Crystal-Cut	SAW Propagation	v_{SAW} [ms^{-1}]	K^2
Quartz	ST	X	3158	0.11
$LiNbO_3$	Y	Z	3488	4.5-4.6
$LiNbO_3$	128°-rot Y	X	3992	5.3-5.6
$Bi_{12}GeO_{20}$	110	001	1681	1.4
$LiTaO_3$	Y	Z	3230	0.72-1.6
GaAs	<001>	(110)	<2841	<0.06

Tab. A.6.1 SAW parameters for selected piezoelectric substrates [Dutta, 1986; Campbell, 1998]

The crystal of $LiNbO_3$ in a 128°-rot Y cut exhibits the highest coupling coefficient for the conversion of an electrical signal into a mechanical wave. Therefore this cut shows the highest surface acoustic wave velocities.

The damping coefficient for acoustic waves in water is presented in Table A.6.2.

T [°C]	a_{H20} [10^{13} ms^{-2}]
10	1.42
15	1.70
20	2.35
25	3.07

Tab. A.6.2 Damping coefficient for longitudinal acoustic waves in water at various temperatures [Frommelt, 2007].

A.7 Lipid - Bilayer Formation

Supported artificial membranes are commonly generated in two different ways:
The first way is the so-called vesicle fusion; the second is the formation of lower and upper leaflet of a lipid bilayer by a combination of the LB- and LS-technique.
The utilization of these techniques in combination with flat-μ-fluidics shall be presented here.

A.7.1 Vesicle Fusion

A previously cleaned and hydrophilic surface, as described in Chapter 1.1.3 is mounted in a fluid cell and small uni-lamellar vesicles (SUV's) are added (see Fig A.7.1(a)). The SUV's rupture by contact with the hydrophilic surface and after a sufficient incubation time period the surface is completely covered by a lipid bilayer [Plant, 1993].

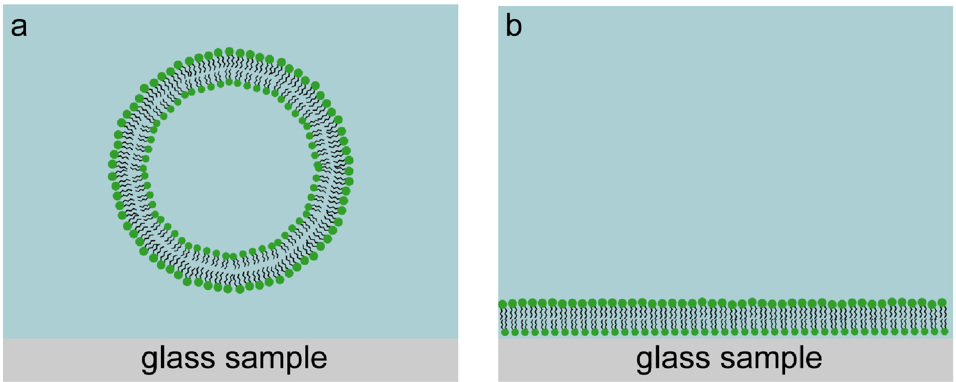

Fig. A.7.1 Schematic picture of (a) a small uni-lamellar vesicle (SUV) approaching the bare glass surface, and (b) the formed lipid bilayer.

The not ruptured fraction of SUV's, accumulated at the channel surface, is removed by flushing the sample volume carefully and a membrane coated surface remains under a bulk of water (see Fig. A.7.1(b)).

Since this is a self-assembling process, the preparation and performance of vesicle fusion is easy and effective. In a first try this technique was also tested to apply a lipid bilayer membrane within a flat-μ-fluidic channel and is stepwise depicted in Fig. A.7.2.

An aqueous solution containing a sufficient amount of SUV's was applied on the previously freshly prepared flat-μ-fluidic channel (a). Within the incubation time, the vesicles accumulate at the channel surface, rupture and cover the hydrophilic channel with a homogenous membrane up to the channel borders (b). Additional SUV's accumulated at the channel surface and especially at the channel boarder, indicated with a red box.

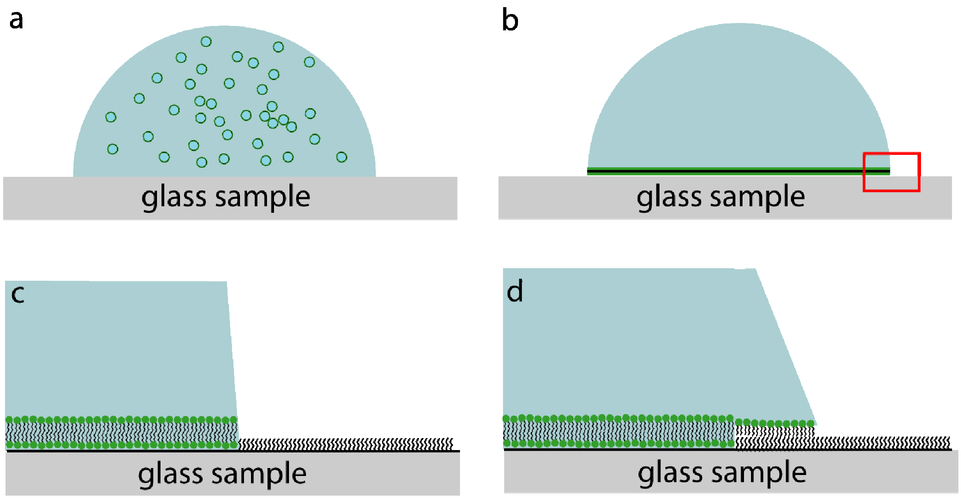

Fig. A.7.2 Vesicle fusion in a flat micro-fluidic channel destroys the hydrophilic-hydrophobic contrast

The formed lipid bilayer (c) is less hydrophilic then the supporting glass surface, therefore the contact angle of the water half sphere is changed. This effect enables the SUV's to spread as a lipid monolayer onto the hydrophobic surrounding (d).

The resulting monolayer is again hydrophilic and destroys therefore the flat-μ-fluidic layout. Therefore this technique could not be used for the surface functionalization of flat-μ-fluidics channels.

A.7.2 Asymmetric Lipid-Bilayer formation with LB and LS Technique

The two step procedure of forming a bilayer separately by a lower and upper leaflet can also be used to form a solid supported lipid bilayer membrane.

As described for the LB transfer technique (see Chapter 1.2.4) in a first step a single lipid monolayer is applied on the surface of a cleaned and hydrophilic surface as shown in Fig. A.7.3(a). The resulting sample with transferred monolayer is pictured in Fig. A.7.3(b).
To create the upper leaflet of a monolayer, the LS technique is used as shown in Fig. A.7.3.3(c). A second monolayer, composed of a different lipid, or a lipid mixture, is spread on a film balance and transferred by the technique reported in Chapter 1.2.5.

After mounting the finally coated sample into a fluid cell (see Fig. 4.4.3(d)), the lipid bilayer membrane can be analyzed by optical microscopy.

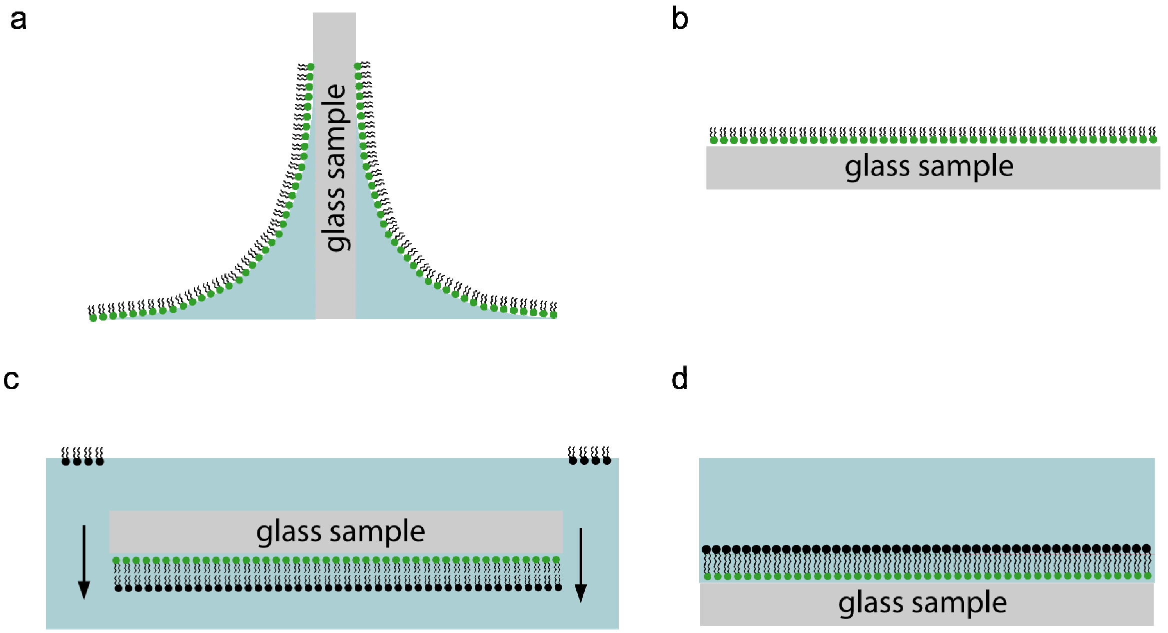

Fig. A.7.3 Sketch of the LB – LS combined deposition technique to form an artificial lipid on a surface.

A big advantage of this bilayer formation method is the high flexibility in the choice of the lipid composition of upper and lower bilayer leaflet, and the adjustable lateral pressure within the transferred membranes. While for fused vesicles the lateral pressure is reported to be about 20 to 25 mNm^{-1}, the pressure for the transfer is free tunable.

During the transfer using a flat-μ-fluidic channel first a lipid monolayer located in the hydrophilic channel ground area is formed, as depicted in Fig. A.7.4(a). This is due to the fact that during a Langmuir-Blodgett no lipid is transferred on a hydrophobic sample surface [Howland et al., 2005; Lenz et al., 2004]. A subsequently performed Langmuir-Schaeffer transfer covers all hydrophobic parts (see Fig. A.7.4(b)), channel and surrounding areas with a lipid monolayer, inverted to the previous LB transferred.

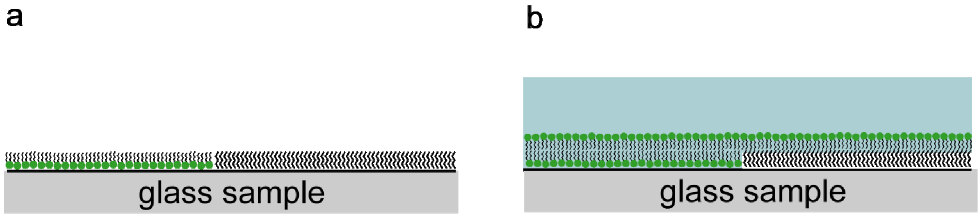

Fig. A.7.4 Sketch of a two step Langmuir-Blodgett, Langmuir-Schaeffer transfer to form a lipid bilayer

As can be seen, this destroys again the hydrophobic/hydrophilic contrast, so that this technique, without any improvement also fails for the structuring of flat-μ-fluidic channels. The improvement necessary to guarantee a successful transfer of an intact lipid bilayer without destruction of the hydrophilic/hydrophobic contrast was the use of a protective sheet, made of PDMS.

A.8 Photolithography

The sample preparation using photolithography was done with a mask-aligner (MJB3, Süss Microtech, Garching, Germany) at clean room conditions (clean room class 1000)

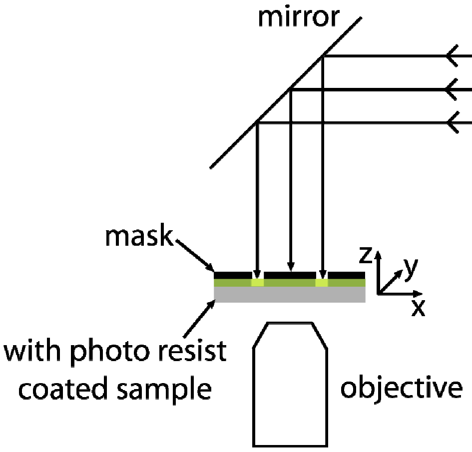

Fig. A.8.1 Sketch of the mask aligner setup MJB3, at the University Augsburg. The sample is aligned with the structure mask on a μm scale with a xy-stage, and afterwards irradiated with UV-light to activate the photo resist coated sample surface.

The used mask-aligner setup is depicted in Fig. A.8.1. It combines an inverted light microscope for alignment of the sample and photolithography mask with an illumination unit for irradiation of the sample through the applied mask with UV-light. The alignment of sample and mask in x and y direction is done on a μm scale before performing the illumination.

Off-set foil masks were printed as templates for flat-μ-fluidic channel structures, see Fig. A.8.2(left) and for PDMS molds, Fig. A.8.2(right).

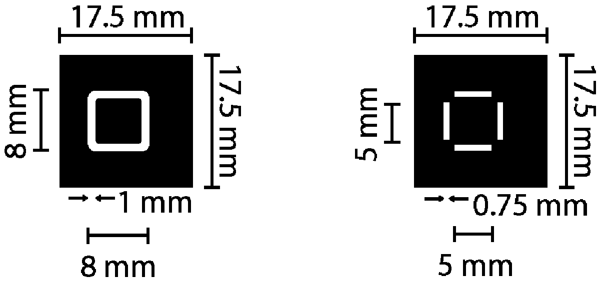

Fig. A.8.2 Sketch of (left) flat-μ-fluidic channel layout, applied on the chip by photolithography and (right) the layout of the corresponding PDMS mold.

A.8.1. *μ*-Fluidic Channels

The preparation steps for micro-fluidic channels are schematically depicted in Fig A.5.3:

(a) Glass cover slides (grey) were cleaned by sonication in different solvents and a wet chemical cleaning step to activate the glass surface for the following silanization as reported in Purrucker [Purrucker, 2004]

(b) The pretreated surface was coated with ODTMS (green) in order to make the glass surface hydrophobic as described by Hillebrandt & Tanaka [Hillebrandt & Tanaka, 20001].

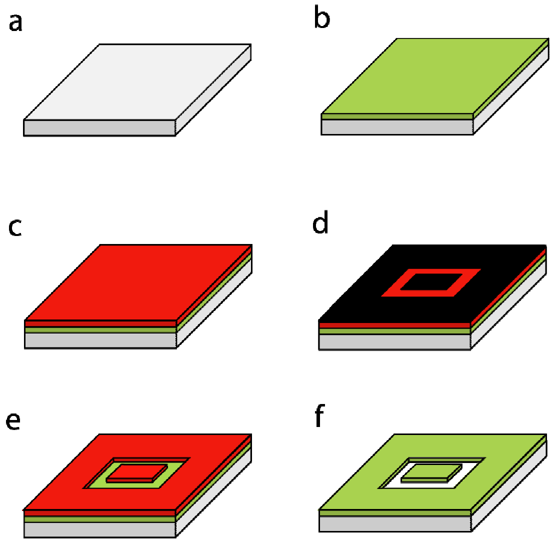

Fig. A.8.3 Sketch of the procedure steps for the preparation of micro-fluidic samples

The following steps are performed under clean room conditions:

(c) A sufficient amount of the photo resist Shipley 1813 (red) is spin coated with 5000rpm for 30sec to apply a homogeneously thin layer of lacquer on the glass surface. Afterwards the sample was baked at 90°C for 30 min to remove the solvents from the lacquer.

(d) The sample structure (black) was applied by the previously described mask-aligner setup by irradiation for 30 sec.

(e) Immediately after the illumination the sample gets developed, where the irradiated parts get lifted.

The now uncovered regions get exposed to an oxygen plasma at 200mbar O_2 for 40 seconds, to remove the ODTMS from glass surface. In a last step the residual photo resist got removed with sonication in Aceton for 3 min.

The produced surface is a hydrophobic environment with a hydrophilic lane. This lane can then be filled with approximately 7 μl aqueous solution and represents the μ-fluidic channel.

A.8.2. PDMS Coversheets

The preparation of casting mold for PDMS protective sheets is slightly different from the procedure for the flat-μ-fluidic channels. The step wise procedure is depicted in Fig. A.8.4. and begins with a cleaning step (a), similar to A.8.3(a)

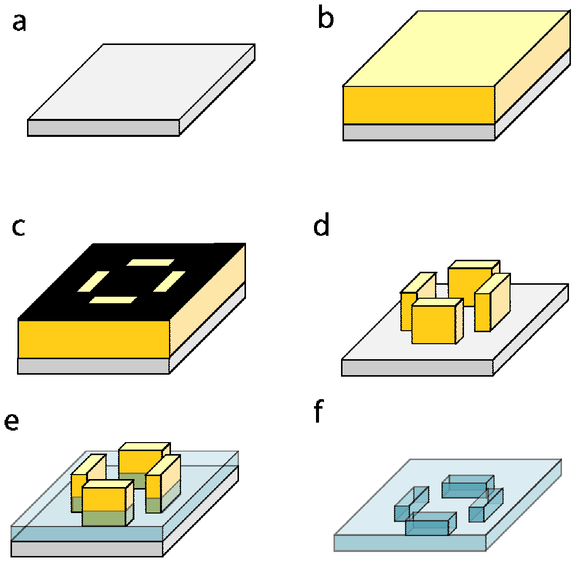

Fig. A.8.4 Sketch of the procedure steps for the preparation of PDMS casting molds.

The steps (b)-(d) are carried out under clean-room conditions

(b) To obtain a layer thickness of approximately 150µm [Kouharenko et al., 2005] a sufficient amount of SU-8/100 photo resist (yellow) was spin coated for 30s at 1460 rpm and 5min at 70°C followed by a 60min at 90°C pre-bake step. In contrast to the photo resist Shipley 1813 the SU-8/100 is a positive lacquer.

(c) The structure mask (black) was aligned and illuminated 3 times for 30sec with a pause of 60s to allow the lacquer to cool down. This should avoid unwanted cross-linking of the lacquer polymers by thermal excitation.

(d) After another 15min at 90°C post-baking, the sample was developed with the corresponding chemistry for 25min and rinsed with Isopropanol to resolve the structure seen in Fig. A.8.4.

Before casting PDMS, the Sylgart 184 silicon oil and curing agent was mixed in a ratio of 10:1 and diluted with approximately 20 vol% Toluol, which is a solvent for unpolymerized silicon oil. This enables the PDMS to fill the casting in mold without covering the SU-8/100 bridges.

(e) The applied layer of PDMS (thickness approximately 75 μm) was polymerized for 8h at 70°C to guarantee a sufficient cross-linking of PDMS.

In Fig. A.8.4(f) the lifted PDMS protective sheet is depicted, where the cavities are formed by the mold. These cavities are finally the dedicated regions, where lipids are able to access the otherwise protected surface and therefore are able to form a monolayer on the surface. The detailed use of the protective sheets is reported in Chapter 4.2.

A.9 Abbreviations

DLVO	Derjaguin-Landau-Verwey-Overbeek
DMPC	dimyristoyl-phosphatidyl-choline
DOPC	1,2-dioleo-*sn*-glycero-3-phosphocholine
E.Coli	escherichia-coli
FEM	finite elements model
FWHM	full width at half maximum
GIXD	grazing-incidence X-ray diffraction
IDT	inter-digital transducer
LB	Langmuir-Blodgett
LD	long distance
$LiNbO_3$	Lithium Niobate
LS	Langmuir-Schaeffer
PBS	phosphate buffered saline
PDMS	polydimethylsiloxane
PEG	poly(ethylene glycol)
PMF	potential of mean force
PSD	position sensitive detector
PTFE	poly-tetrafluoroethylene (“Teflon”)
SAW	surface acoustic wave
SAXS	small angle X-ray scattering
SUV	small uni-lamellar vesicles
Texas Red-PE	1,2-dihexadecanoyl-sn-glycero-3-phosphoethanolamine, triethyl-ammonium salt
WAXS	wide angle X-ray scattering

A.10 Symbols

A	area
A_{mol}	molecular area
α_f	angle of diffraction in z-plane
α_i	incidence angle
c_{ij}	coupling tensor
d	correlation length
ε	dielectric constant
ε_{ij}	dielectric tensor
$\varepsilon(\eta)$	in-plane deviation
$\mathbf{E}$	electric field
η	offset angle
h^{mo}	molecular height
k	wave vector
k'	spring constant
k_B	Boltzmann constant
K	electromechanical coupling coefficiant
χ	molar fraction
λ	X-ray wavelength
$m_\perp$	dipole density normal
$\mu_\perp$	molecular dipole moment normal
N	number of domains
Π	surface pressure
r	radial distance
ρ	micro-domain density
Ψ	true scattering angle
q	scattering vector
T	temperature
T_{ij}	tension tensor
Θ	angle of diffraction in x-y plane
Θ_B	Bragg angle
$v(r)$	harmonic potential
V	surface potential
γ	surface tension

Bibliography

[Acheson, 1990] Acheson, D.J. (1990) *Elementary Fluid Dynamics*, New York: Oxford University Press.

[Advalytix, 2004] (2004) *personal communication* with Zeno von Guttenberg, staff member of the Advalytix AG.

[Als-Nielsen et al., 1994] Als-Nielsen, J., Jacquemain, D., Kjaer, K., Leveiller, F., Lahav, M. & Leiserowitz, L. (1994). Principles and applications of grazing incidence X-ray and neutron scattering from ordered molecular monolayers at the air water interface. *Physics Reports*, 246, 251-313.

[Als-Nielsen, 2001] Als-Nielsen, J. & McMorrow, D. (2001) *Elements of Modern X-Ray Physics,* New York: John Wiley & Sons, Ltd.

[Anderson, 1998] Anderson, R.G.W. (1998). The Caveolae Membrane System. *Annual Review in Biochemistry,* 67, 199-225.

[Anderson & Jacobson, 2002] Anderson, R.G.W. & Jacobson, K. (2002). A Role for Lipid Shells in Targeting Proteins to Caveolae, Rafts and other Lipid Domains. *Science*, 296, 1821-1825.

[Baird et al., 1999] Baird, B., Sheets, E.D. & Holowka, D. (1999). How does the Plasma Membrane Participate in Cellular Signalling by Receptors for Immunoglobulin E? *Biophysical Chemistry* 82, 109-119.

[Barton et al., 1991] Barton, S., Goudot, A., Bouloussa, O., Rondelez, F., Lin, B., Novak F., Acero, A. & Rice, S.A. (1991). Structural transitions in a monolayer of fluorinated amphiphil molecules. *Journal of Chemical Physics* 96, 1343-1351.

[Brian & McConnell, 1984] Brian, A. & McConnell, H. (1984). Allogeneic stimulation of cytotoxic T cells by supported planar membranes. *Proceedings of the National Academy of Science* 81, 6159-6163.

[Brockmann, 1994] Brockmann, H. (1994). Dipole Potential of Lipid Membranes *Chemistry and Physics of Lipids* 73, 57-79.

[Belloni, 2000] Belloni, L. (2000). Colloidal interactions. *Journal of Physics: Condensed Matter*, 12, R549-R587.

[Blodgett, 1934] Blodgett, K. B. (1934). Monomolecular films of fatty acids on glass. *Journal of the American Chemical Society,* 56, 495.

[Blodgett, 1935] Blodgett, K. B. (1935). Films built by depositing successive monomolecular layers on a solid surface. *Journal of the American Chemical Society*, 57, 1007-1022.

[Blodgett & Langmuir, 1937] Blodgett, K. B. & Langmuir, I. (1937). Built-up films of barium stearate and their optical properties. *Physical Review*, 51, 964-982.

[Brunner, 2003] Brunner, M. (2003). *Effective Interactions and Phase Behavior of Colloidal Monolayers in the Presence of Light-Induced Substrate Potentials*. PhD Thesis, Universität Konstanz, Germany.

[Bunn & Howells., 1954] Bunn, C.W. & Howells, E.R. (1954). Structures of Molecules and Crystals of Fluorocarbons. *Nature*, 174, 549-551.

[Campbell, 1998] Campbell, C. (1998). *Surface Acoustic Wave Devices for Mobile and Wireless Communication*. Boston: Academic Press.

[Charitat et al., 1999] Charitat, T., Bellet-Amalric, E., Fragneto, G. & Graner, F. (1999) Adsorbed and free lipid bilayers at the solid-liquid interface. *European Physical Journal B*, 8, 583-593.

[Chaudhury & Owen, 1993] Chaudhury, M.K., & Owen, M.J. (1993) Adhesion Hysteresis and Friction. *Langmuir*, 9, 29-31.

[Dantzler Siebert & Knobler, 1971] Dantzler Siebert, E.M. & Knobler C.M. (1971) Interaction Virial Coefficients in Hydrocarbon-Fluorocarbon Mixtures. *The Journal of Physical Chemistry*, 75(25), 3863-3870.

[Dutta, 1986] Dutta, S. (1986). *Surface Acoustic Wave Devices*. Prentice Hall.

[Dynarowicz-Latka et al., 2001] Dynarowicz-Latka, P., Dhanabalan, A. & Oliveira, O. (2001). Modern physiochemical research on Langmuir monolayers. *Advances in Colloid and Interfacial Science*, 91, 221-293.

[Edidin, 2003] Edidin, M., (2003). The State of Lipid Rafts: From Model Membranes to Cells. *Annual Reviews of Biophysics and Biomolecular Structure*, 32, 257-283.

[Engel et al., 2003] Engel, A., Chatterjee, S.K., Al-Arifi, A. & Nuhn, P. (2003). Influence of Spacer Length on the Agglutination of Glycolipid-Incorporated Liposomes by ConA as Model Membrane. *Journal of Pharmaceutical Science*, 92/11, 2229-2235.

[Evans & Wennerström, 1994] Evans, D.F. & Wennerström H. (1994). *The Colloidal Domain: Where Physics, Chemistry, Biology and Technology meet*. New York: Wiley-VCH.

[Frommelt, 2007] Frommelt, T. (2007). *Mischen und Sortieren mit SAW-Fluidik in Simulation und Experiment*. PhD Thesis, Universität Augsburg, Germany.

[Gaines, 1966] Gaines, G. L. (1966). *Insoluble Monolayers at Liquid-Gas Interfaces*. New York: Wiley – Interscience.

[Gege et al., 2004] Gege, C., Schneider M. F., Schumacher, G., Limozin, L., Rothe, U., Bendas, G., Tanaka, M. & Schmidt R. R. Functional Microdomains of Glycolipids with Partially Fluorinated Membrane Anchors: Impact on Cell Adhesion. *ChemPhysChem*, 5, 216-224.

[Guinier, 1963] Guinier, A. (1963) *X-Ray Diffraction: In Crystals, Imperfect Crystals, and Amorphous Bodies*. San Francisco: W.H. Freeman

[Hansen, 2007] Hansen, J. P. & McDonald, I. R. (2007) *Theory of Simple Liquids*, London: Academic Press

[Heerklotz, 2002] Heerklotz, H. (2002). Triton Promotes Domain Formation in Lipid Raft Mixtures. *Biophysical Journal*, 83, 2693-2701.

[Howland et a., 2005] Howland, M.C., Sapuri-Butti, A.R., Dixit, S., Dattelbaum, A.M., Shreve, A.P. & Parikh, A.N. (2005). Phospholipid Morphologies on Photochemically Patterned Silane Monolayers. *Journal of the American Chemical Society*, 127, 6752-6765.

[Hillebrandt & Tanaka, 2001] Hillebrandt, H. & Tanaka, M. (2001). Electrochemical Characterization of Self-Assembled Alkylsiloxane Monolayers on Indium-Tin Oxide (ITO) Semiconductor Electrodes. *Journal of Physical Chemistry B*, 105, 4270-4276.

[Hu et al., 2006] Hu, Y., Meleson, K. & Israelachvili, J. (2006). Thermodynamic Equilibrium of Domains in a Two-Component Langmuir Monolayer. *Biophysical Journal*, 91, 444-453.

[Huang & Feigenson, 1999] Huang, J. & Feigenson, G.W. (1999). A Microscopic Interaction Model of Maximum Solubility of Cholesterol in Lipid Bilayers. *Biophysical Journal*, 76, 2142-2157.

[Jacobson & Dietrich, 1999] Jacobson, K. & Dietrich, C. (1999). Looking on Lipid Rafts. *Trends in Cell Biology*, 9, 87-91.

[Jain & White, 1977] Jain, M.K. & White, H.B. (1977). Long-range Order in Biomembranes. *Advances in Lipid Research*, 15, 1-60.

[Israelachvili, 1991] Israelachvili, J. N. (1991). *Intermolecular and Surface Forces*, Academic Press Inc.

[Kern & Puotinen, 1970] Kern, W. & Puotinen, D. (1970). Cleaning solutions based on hydrogen peroxide for use in silicon semiconductor technology. *RCA Review*, 31, 187-206.

[Koukharenko , 2005] Koukharenko, E., Kraft, M., Ensell, G.J. & Hollinshead, N. (2005). A comparative study of different thick photoresists for MEMS applications. *Journal of Material Science: Material in Electronics*, 16, 741-747.

[KIBRON - Homepage] http://www.kibron.com/tensiometers/langmuir-blodgett-trough. *Homepage of KIBRON INC.*

[Krafft & Riess, 1998] Krafft, M.P. & Riess J.G. (1998). Highly fluorinated amphiphiles and colloidal systems, and their applications in the biomedical field. A contribution. *Biochimie*, 80, 489-514.

[KSV - Homepage] http://www.ksvltd.com/content/index/minitrough. *Homepage of KSV Instruments Ltd.*

[Lenz et al., 2004] Lenz, P., Ajo-Franklin, C.M. & Boxer, S. (2004). Patterned Supported Lipid Bilayers and Monolayers on Poly(dimethylsiloxan). *Langmuir*, 20, 11092-11099.

[Lipowsky & Dimova, 2003] Lipowsky, R. & Dimova R. (2003). Domains in Membranes and Vesicles. *Journal of Physics: Condensed Matter*, 15, S31-S45.

[London & Brown, 2000] London, E. & Brown D.A. (2000). Insolubility of Lipids in Triton X-100: Physical Origin and Relationships to Sphingolipid/Cholesterol Membrane Domains (Rafts). *Biochimica et Biophysica Acta*, 1508, 182-195.

[Maxfield, 2002] Maxfield, F.R. (2002). Plasma Membrane Microdomains. *Current Opinion in Cell Biology*, 14, 483-487.

[McConnell, 1991] McConnell, H.M. (1991). Structures and Transitions in Lipid Monolayers at the Air-Water Interface. *Annual Reviews in Physical Chemistry*, 42, 171-195.

[McConnell & Radhakrishnan, 2003] McConnell, H.M. & Radhakrishnan, A. (2003). Condensed Complexes of Cholesterol and Phospholipids. *Biochimica et Biophysica Acta*, 1610, 159-173.

[McConnell & Vrljic, 2003] McConnell, H.M. & Vrljic, M. (2003). Liquid-Liquid Immiscibility in Membranes . *Annual Reviews of Biophysics and Biomolecular Structure*, 32, 469-492.

[Metzger et al., 1999] Metzger, T.H., Kegel, I., Paniago, R. & Peisl, J. (1999). Grazing Incidence x-ray scattering: an ideal tool to study the structure of quantum dots. *Journal of Physics: Applied Physics*, 32, A202-A207.

[Mooney et al., 1996] Mooney, J.F., Hunt, A.J. & McIntosh, J.R. (1996). Patterning of functional antibodies and other proteins by photolithography of silane monolayers. *Proceedings of the National Academy of Science*, 93, 12287-12291.

[Möhwald, 1990] Möhwald, H. (1990). Phospholipid and phospholipid-protein monolayers at the air/water interface. *Annual Reviews of Physical Chemistry*, 41, 441-476.

[Möhwald, 1995] Möhwald, H. (1995). *'Phospholipid Monolayers'* in *'Handbook of Biological Physics - Structure and Dynamics of Membranes'*, Volume 1, (pp. 161-211). Elsevier Science B. V.:Amsterdam

[Mukerjee & Maxfield, 2004] Mukerjee, S. & Maxfield, F.R. (2004). Membrane Domains. *Annual Reviews of Cell and Developmental Biology*, 20, 839-866.

[Nikolaides et al., 2002] Nikolaides, M.G, Bausch, A.R., Hsu, M.F., Dinsmore, A.D., Brenner M.P., Gay. C. & Weitz, D.A. (2002).Electric-field-induced capillary attraction between like-charged particles at liquid interfaces. *Nature*, 420, 299-301.

[Nima - Homepage] http://www.nima.co.uk/equipment/equipindex.htm. *Homepage of Nima Technology Ltd.*

[Nyborg, 1965] Nyborg, W.L. (1965). *Acoustic streaming* in *Pysical Acoustics 2B: Properties of polymers and nonlinear acoustics*, edited by Mason, W.P., Academic Press.

[Oelke, 2008] Oelke, J., Pasc, A., Konovalov, O. & Tanaka, M. Influence of Molecular Structure on the Micro/Nano-Domains of Fluorinated Lipids. *in preparation*.

[Parton & Simons, 2007] Parton, R.G. & Simons, K. (2007). The Multiple Faces of Caleolae. *Nature Reviews Molecular Cell Biology*, 8, 185-194.

[Plant, 1993] Plant, A.L. (1993). Self-Assembled Phospholipid/Alkanethiol Biometric Bilayers on Gold. *Langmuir*, 9, 2764-2767.

[Purrucker, 2004] Purrucker, O. (2004). *Establishment of a New Plasma Membrane Model with Well-Defined Polymer Spacers*. PhD Thesis, Technische Universität München, Germany.

[Quesada-Pérez et al., 2001] Quesada-Pérez, M., Moncho-Jordá, A., Martinez-López, F. & Hidalgo-Álvarez, R. (2001) Probing interaction forces in colloidal monolayers: Inversion of structural data. *Journal of Chemical Physics*, 115(23), 10897-10902.

[Quesada-Pérez et al., 2002] Quesada-Pérez, M., Callejas-Fernández, J., & Hidalgo-Álvarez, R. (2002) Interaction potentials, structural ordering and effective charges in dispersions of charged colloidal particles, *Advances in Colloid and Interface Science*, 95, 295-315.

[Rayleigh, 1885] Lord Rayleigh (1885) On Waves Propagating along the Plane Surface of an Elastic Solid, *Proceedings of the London Mathematical Society*, 7, 4-11.

[Rayleigh, 1905] Lord Rayleigh (1905), *Philosophical Magazine*, 10 (Ser 6), 364-374.

[Riess, 2002] Riess, J. G (2002). Flurous micro- and nanophase with a medical perspective. *Tetrahedron*, 58, 4113-4131.

[Riess & Greiner, 2000] Riess, J. G. & Greiner, J. (2000). Carbohydrate- and related polyol derived fluorosurfactants: an update. *Carbohydrate Research*, 327, 147-168.

[Riess & Krafft, 1998] Riess, J. G. & Krafft, M. P. (1998). Fluorinated Materials for in vivo oxygen transport (blood substitutes), diagnosis and drug delivery. *Biomaterials*, 19, 1529-1539.

[Rowlinson, 1969] Rowlinson, J. S. (1969). *Liquids and Liquid Mixtures*, 2nd Ed. Butterworths, London.

[Sackmann & Lipowsky, 1995] Sackmann, E & Lipowsky, R. (1995) '*Biological Membranes, Architecture and Function*' in *'Handbook of Biological Physics - Structure and Dynamics of Membranes'*, Volume 1, (pp. 1-62). Elsevier Science B. V.:Amsterdam

[Sackmann, 1996] Sackmann, E. (1996). Supported Membranes: Scientific and Practical Applications. *Science*, 271, 43-48.

[Schneider et al., 2005] Schneider, M.F., Andelman, D. & Tanaka, M. (2005). Stripes of Partially Fluorinated Alkyl Chains: Dipolar Langmuir Monolayers. *The Journal of Chemical Physics*, 122, 094717.

[Simons & Ikonen, 1997] Simons, K. & Ikonen, E. (1997). Functional rafts in cell membranes. *Nature*, 387, 569-572.

[Simons & Toomre, 2000] Simons, K. & Toomre, D. (2000). Lipid Rafts and Signal Transduction. *Nature Reviews Molecular Cell Biology*, 1, 31-39.

[Simons & Vaz, 2004] Simons, K. & Vaz, W.L.C. (2004). Model Systems, Lipid Rafts and Cell Membranes. *Annual Reviews of Biophysics and Biomolecular Structure*, 33, 269-295.

[Singer & Nicolson, 1972] Singer, S.J. & Nicoslon, G.L. (1972). The Fluid Mosaic Model of the Structure of Membranes. *Science*, 175, 720-731.

[Sitheran, 2008] Sitheran, K. (2008). *Applications of Surface Acoustic Waves (SAW) for Chemical and Biological Analysis*. PhD Thesis, Universität Augsburg, Germany.

[Smilgies., 2003] Smilgies, D. M. (2003) High-resolution grazing-incidence scattering using a combination of analyzer crystal and linear detector. *Review of Scientific Instruments*, 74, 4041-4047.

[Smilgies et al., 2005] Smilgies, D. M., Boudet, N., Struth, B. & Konovalov, O. (2005) Troika II : A versatile beamline for the study of liquid and solid interfaces, *Journal of Synchrotron Radiation*, 12, 329-339.

[Strobel, 2005] Strobel, C. J. (2005). *Mikro- und Nanofluidik auf piezoelektrischen Substraten*. PhD Thesis, Ludwigs-Maximilians-Universität München, Germany.

[Tamm & McConnell, 1985] Tamm, L. & McConnell, H. (1985). Supported Phospholipid Bilayers. *Biophysical Journal,* 47, 105-113.

[Tanaka & Sackmann, 2005] Tanaka, M. & Sackmann, E. (2005). Polymer-Supported Membranes as models of the cell surface, Nature, 437, 656-663.

[Tanford, 1980] Tanford, C. (1980). *The Hydrophobic Effect: Formation of Micelles and Biological Membranes*, New York: Wiley-Interscience, 2. Edition.

[Thomas, 2008] Thomas, W.E. (2008). Catch Bonds in Adhesion, *Annual Review of Biomedical Engineering* , 10, 39-57.

[Thomas et al., 2004] Thomas, W.E., Nilsson, L., Forero, M., Sukorenko, E.V. & Vogel, V. (2004). “Stick-and-roll” bacteria adhesion mediated by catch bonds, *Molecular Microbiology,* 53, 1545.

[Thompson & Tillack, 1985] Thompson, T. & Tillack, T. (1985). Organization of glycosphingolipids in bilayers and plasma membranes of mammalian cells, *Annual Reviews of Biophysical Chemistry,* 14, 361-386.

[Tristram-Nagle et al., 1998] Tristram-Nagle, S., Petrache, H.I. & Nagle, J.F. (1998). Structure and Interactions of Fully Hydrated Dioleoylphosphatidylcholine Bilayers, *Biophysical Journal, 75,* 917-925.

[Vanderlick & Möhwald, 1990] Vanderlick, T.K. & Möhwald, H. (1990). Mode Selection and Shape Transition of Phospholipid Monolayer Domains. *Journal of Physical Chemistry*, 94, 886-890.

[Verwey & Overbeck, 1948] Verwey, E.J.W. & Overbeck J.T.G. (1948). *Theory of the Stability of Lyophobic Colloids*. Elsevier Science B. V.:Amsterdam.

[Vogel & Möbius, 1988] Vogel, V. & Möbius, D. (1988). Local Surface Potentials and Electric Dipole Moments of Lipid Monolayers: Contributions of the Water/Lipid and the Lipid/air Interface. *Journal of Colloid and Interface Science*, 126, 408-420.

[White & Voltmer, 1965] White, R.M. & Voltmer, F.W. (1965). Direct Piezoelectric Coupling to Surface Elastic Waves. *Applied Physical Letters*, 17, 314-3 16.

[Wiegart et al., 2005] Wiegart, L., Struth, B., Tolan, M. & Terech, P. (2005). Thermodynamic and Structural Properties of Phospholipid Langmuir Monolayers on Hydrosol Surfaces. *Langmuir*, 21, 7349-7357.

[Wixforth et al., 2004] Wixforth, A., Strobel, Ch., Gauer, Ch., Toegl, A., Scriba, J. & v. Guttenberg, Z. (2004). Acoustic Manipulation of Small Droplets. *Analytical and Bioanalytical Chemistry*, 379, 982-991.

[Zeiss - Homepage] http://www.zeiss.de/mikro *Homepage of Carl Zeiss AG*

Danksagung

Zum Ende dieser Arbeit möchte ich nun noch allen denjenigen Vielen Dank sagen, die zum Gelingen dieser Arbeit beigetragen haben.

Prof. Achim Wixforth möchte ich danken, dass er mich immer bei allen Ideen unterstützt hat, die ich im in Laufe dieser Promotion in seinem Lehrstuhl hatte, und dass meine Anliegen bei ihm immer auf positive Resonanz gestoßen sind.

Prof. Motomu Tanaka gebührt mein ganz besonderer Dank, er war mir als Betreuer dieser Arbeit jederzeit mit Rat zur Seite gestanden und er hat es mir ermöglicht, dass ich in dieser Arbeit so viele unterschiedliche Techniken erlernen und nutzen durfte.

Meinen Zimmerkollegen in der Technischen Universität München, **Thomas Schubert** und **Murat Tutus** möchte ich für viele Diskussionen und die nette Atmosphäre im Büro danken, die während unserer Arbeit geherrscht hat. Im Speziellen danke ich Thomas für seine immer sehr klaren Worte zu meiner Arbeit, die mir immer als Motivation gedient haben. Viel Erfolg Euch beiden für Eure Doktorarbeit!

Nicht zu vergessen der Rest der Arbeitsgruppe von Prof. Tanaka in München und jetzt in Heidelberg, **Dr. Fernanda Rosetti**, **Manuel Schneck**, **Peter Seitz**, **Thomas Kaindl.** Ihnen danke ich ebenfalls für eine schöne und interessante Zeit. Im Besondern gilt es hier **Dr. Stefan Kaufmann** zu erwähnen, der mich tatkräftig in der Präparation der biologischen Proben unterstützt hat. Für die zahllosen Korrekturrunden an dieser Arbeit möchte ich noch einen extra Dank an Fernanda, Manuel, Tom und Thomas richten.

Den ehemaligen Mitgliedern der Arbeitsgruppe Tanaka an der TU-München möchte ich ebenfalls danken. **Dr. Andreea Pasc** für die Synthese der fluorinierten Lipide, die ich im Zuge dieser Arbeit verwendet habe und Ihre Unterstützung in vielen Experimenten. Wo wäre ich ohne Ihre Unterstützung zum Verständnis der Fluorchemie! Für meine umfassende Einweisung in den E22 zu Beginn meiner Tätigkeit in München möchte ich **Dr. Oliver Purrucker** danken. Mit Ihm durfte ich nahezu ein Jahr noch ein Büro teilen. **Dr. Fatima Al-Ali**, **Dr. Rafael Oliveira** und **Dr. Daniel Gasull** danke ich ebenfalls für Diskussionen und Ihre Unterstützung in der Erlernung verschiedener experimenteller Techniken.

Prof. Matthias Rief möchte ich noch danken für das Verständnis und die Möglichkeit mein Büro an der TU-München übergangsweise zu behalten, nach dem Umzug der

AG Tanaka nach Heidelberg. Den restlichen Mitgliedern am E22 sei auch gedankt für zwei interessante und schöne Jahre an der TUM.

In der Universität Augsburg danke ich **Stephan Nuschele** und **Daniel Steppich** für meine ersten Einweisungen in die Biophysik noch vor dieser Promotion. Euch beiden ebenso noch viel Erfolg für eure Doktorarbeit!

Dr. Matthias Schneider und **Dr. Thomas Franke** danke ich für die erhellenden Diskussionen im Kaffeezimmer und Ihre Ideen zur Lösung verschiedener technischer Probleme. Meinen Bürokollegen aus dem Augsburger „Doktorandenbüro“ **Stephan Völk**, **Jürgen Neumann, Stephan Nuschele** und **Christian Leirer** danke ich für die wirklich sehr gemütliche und freundschaftliche Atmosphäre, die in unserem Zimmer jederzeit geherrscht hat. Das erleichterte mir die Arbeit ungemein!
Den übrigen Mitgliedern des Lehrstuhls EP1 an der Uni Augsburg sei ebenfalls für ein angenehmes letztes Jahr meiner Promotion gedankt!

Für die Unterstützung an den Röntgenstreu-Einrichtungen gilt mein Dank den beiden verantwortlichen Wissenschaftlern **Oleg Konovalov** (ESRF, Grenoble, France) und **Sérgio S. Funari** (HASYLAB, Hamburg). Der Firma Advalytix und hier im speziellen Herrn **Dr. Zeno von Guttenberg** danke ich für die Beantwortung aller Fragen im Zusammenhang mit dem Flat-μ-Fluidics Aufbau. Dem Werkstattmeister **Rudi Lehrhuber** des E22 möchte ich noch für die Fertigung der verwendeten Klimakammer danken.

Abschließend möchte ich auch allen denjenigen danken die mich auch im Verlauf dieser Arbeit außerhalb der Universität begleitet haben:
Ganz besonders meiner **Mutter**, aber auch meinem **Bruder Thorsten** und meiner **Großmutter** möchte ich danken, da ich ohne Ihre stetige Unterstützung sicherlich nicht soweit hätte kommen können und dafür, dass sie immer viel Geduld mit mir hatten. Meiner restlichen Familie möchte ich ebenfalls für die allgemeine Unterstützung danken, so z.B. für unzählige entspannende Champions-League Abende mit meinem **Cousin Thomas** während der anstrengenden Schreibephasen.

Meiner Freundin **Christine** gebührt nun noch einen ganz besonders lieber Dank für die Hilfe bei so manchem illustratorischem Problem und vor allem für Ihre Unterstützung und Motivationsarbeit, gerade in der letzten Phase dieser Arbeit!

Allen, die ich nun vergessen haben sollte sage ich auch nochmal **ein herzliches Dankeschön!**

Lebenslauf

Name: Jochen Oelke
Geburtsdatum: 13.04.1978
Geburtsort: Augsburg
Familienstand: Ledig
Eltern: Gisela Oelke, geb. Birkenmaier
Hermann Oelke
Geschwister: Thorsten Oelke

Schulausbildung

Sept. 1984 – Juli 1988	Volks- u. Hauptschule Firnhaberau
Sept. 1988 – Juli 1997	Jakob-Fugger-Gymnasium Augsburg

Zivildienst

Okt. 1997 – Sept. 1998	Anna Kolleg der Diakonie Augsburg

Studium

Okt. 1998 – Juli 2004	Studium der Physik an der Universität Augsburg mit dem Nebenfach Betriebswirtschaftlehre
Aug. 2003 – Juli 2004	Diplomarbeit am Lehrstuhl für Experimentelle Plasmaphysik der Universität Augsburg Thema: „*Energieverbrauch in Städten – der Weg von physikalischen Gebäudemodellen zu integralen Stadtmodellen*“
Okt. 2004 – Dez. 2006	Wissenschaftlicher Angestellter am Lehrstuhl für Biophysik E22 der Technischen Universität München
Jan. 2007 – Dez. 2007	Wissenschaftlicher Angestellter am Lehrstuhl für Experimentalphysik I der Universität Augsburg
Jan. 2008 – Feb.. 2008	Wissenschaftlicher Angestellter am Lehrstuhl für Biophysik E22 der Universität Heidelberg

Beruf

Seit März 2008	Anstellung als Patentmanager bei der Olympus Life Science Research Europe GmbH, München